



저작자표시-비영리-변경금지 2.0 대한민국

이용자는 아래의 조건을 따르는 경우에 한하여 자유롭게

- 이 저작물을 복제, 배포, 전송, 전시, 공연 및 방송할 수 있습니다.

다음과 같은 조건을 따라야 합니다:



저작자표시. 귀하는 원저작자를 표시하여야 합니다.



비영리. 귀하는 이 저작물을 영리 목적으로 이용할 수 없습니다.



변경금지. 귀하는 이 저작물을 개작, 변형 또는 가공할 수 없습니다.

- 귀하는, 이 저작물의 재이용이나 배포의 경우, 이 저작물에 적용된 이용허락조건을 명확하게 나타내어야 합니다.
- 저작권자로부터 별도의 허가를 받으면 이러한 조건들은 적용되지 않습니다.

저작권법에 따른 이용자의 권리는 위의 내용에 의하여 영향을 받지 않습니다.

이것은 [이용허락규약\(Legal Code\)](#)을 이해하기 쉽게 요약한 것입니다.

[Disclaimer](#)

공학박사학위논문

평판 구조물 내의 탄성 유도초음파 산란
현상에 대한 T -matrix 해법

Scattering analysis of guided waves in a plate
using the T -matrix method

2015 년 8 월

서울대학교 대학원

기계항공공학부

이 흥 선

평판 구조물 내의 탄성 유도초음파 산란 현상에 대한 T -matrix 해법

Scattering analysis of guided waves in a plate
using the T -matrix method

지도교수 김 윤 영

이 논문을 공학박사 학위논문으로 제출함

2015 년 5 월

서울대학교 대학원

기계항공공학부

이 흥 선

이흥선의 공학박사 학위논문을 인준함

2015 년 6 월

위 원 장 : 조 맹 효

부위원장 : 김 윤 영

위 원 : 김 진 오

위 원 : 윤 병 동

위 원 : 김 도 년

Abstract

Scattering analysis of guided waves in a plate using the T -matrix method

Heung Son Lee

School of Mechanical and Aerospace Engineering

The Graduate School

Seoul National University

The main focus of this dissertation is on development of semi-theoretical methods for scattering analysis of guided waves in plates. The area of concern is problems related to flat transversely isotropic plates which include single or multi-layer isotropic and functionally graded plates. Specifically, we focus on the development of wavefunction expansion methods based on the three-dimensional elasticity; in wavefunction expansion method, wave fields are expanded in terms of the eigenfunctions for the governing wave equation. We aim to solve problems that have not been solved before by previously existing wavefunction expansion methods and thus adopt the transition matrix formalism that has been well known for bulk wave scattering problems. In this formalism, the relation between the coefficient vector of a scattered field and that of an incident field is given by the transition matrix.

For this reason, we first derive the Green's function by employing integral transform whose transform kernel is the eigenfunctions for Lamb and SH waves. Then, we

develop the extended boundary condition method based on the null-field integral equation by using the derived Green's function. By using the extended boundary condition method, the T matrix for a single scatterer such as an elastic inclusion, a hole, a step thickness increase or reduction can be calculated. And the multiple scattering solution for these scatterers can be also obtained by using the single scatterer T matrices. We also derive the general properties of the T matrix which represent the reciprocity, energy conservation and time-reversal invariance.

Another development is a decomposition method particularly useful for solving scattering problems regarding arbitrarily shaped elastic inclusions. In this method, an elastic inclusion is decomposed into multiple small subscatterers and then a multiple scattering among subscatterers is calculated. By employing this approach, the restrictions imposed by the inherent problem of the extended boundary condition method can be relaxed and therefore elastic inclusions of various shapes and sizes can be covered.

The developed methods are validated by the finite element method or analytic solutions obtained from the approximate plate theories.

Keywords: Elastic wave, Guided wave, Plate wave, Scattering analysis

Student Number: 2009-20715

Contents

Abstract	i
Chapter 1 Introduction	1
1.1 Motivation	1
1.2 Background literatures	3
1.2.1 Review of advances in the T matrix formalism	4
1.2.2 Analytic or semi-analytic methods for scattering problems in elastic plates	7
1.3 Research objectives	10
1.4 Thesis outline	11
Chapter 2 Green's function for guided waves in a flat transversely isotropic plate	13
2.1 Backgrounds	13
2.2 Derivation of the Green's function	15
2.2.1 Green's function in the cylindrical coordinate system	16
2.2.2 Green's function in Cartesian coordinate system	31
2.3 Calculation of basis functions	38
2.3.1 Analytic solutions for an isotropic plate	39
2.3.2 Numerical solutions by using the pseudo-spectral collocation method for a transverse isotropic plate	42

2.4	Modeling of guided wave actuators	53
2.4.1	Axisymmetric line tractions	54
2.4.2	Straight line tractions	55
2.5	Numerical examples regarding functionally graded plates	59
2.5.1	Material properties of functionally graded plates	59
2.5.2	Through-thickness mode shapes of guided waves	60
2.5.3	Beam patterns of waves generated by a line traction	63
2.6	Approximate plate theories	64
2.6.1	Kirchhoff plate theory	65
2.6.2	Mindlin plate theory	66
2.6.3	Multipole expansion of flexural waves excited by arbitrary vertical loads	67
2.6.4	Comparison of the elasticity theory with plate theories	67

Chapter 3 Scattering analysis for guided waves in a flat transversely isotropic plate by using the T -matrix method 70

3.1	T matrix calculation using the extended boundary condition method for a single scatterer	71
3.1.1	The extended boundary condition method	71
3.1.2	Derivation of the T matrix in case when a plate and a scatterer are of the same thickness	73
3.1.3	Derivation of the T matrix in case when there is a thickness difference between a plate and a scatterer	77
3.1.4	Translation of fields generated by tractions to the coordinate system for the scatterer	81
3.1.5	Numerical examples	83
3.2	Multiple scattering analysis using the T -matrix method	86

3.2.1	Derivation of the T-matrix for multiple scatterers	86
3.3	Properties of the T matrix	91
3.3.1	Orthogonality relations between basis functions in the cylindrical coordinate system	91
3.3.2	Derivation for three properties of the T matrix	100
3.3.3	Summary	105
3.4	Decomposition method for elastic inclusions using multiple scattering theory	107
3.4.1	Overall description of the decomposition method	107
3.4.2	Details related to implementation	110
3.4.3	Numerical examples	114
Chapter 4	Conclusion and future works	127
4.1	Conclusion	127
4.2	Future works	129
Chapter A	Settings for the finite element method	131
초록		146

List of Figures

Figure 2.1	Guided wave excitation in an infinite plate of the thickness d with the coordinate system.	15
Figure 2.2	The dispersion curve for the shear horizontal wave modes with (bi-)orthogonal modes marked by circles. (a) The orthogonality relation derived in the present theory along the constant real k line, (b) the bi-orthogonality relation from the previous research [59] along the constant ω_{ext} line. Symbols: $\kappa = dk/\pi$ (dimensionless wavenumber), $\Omega = d\omega/\pi c_t$ (dimensionless frequency), $c_l = 6198$ m/s (longitudinal wave speed), $c_t = 3130$ m/s (shear wave speed).	23
Figure 2.3	A contour enclosing (a) a pole on the real axis, (b) a pole on the imaginary axis and (c) a pair of complex-valued poles.	26
Figure 2.4	A path in the complex plane of ϕ over which the contour integration is performed when k_n is (a) real or complex, (b) imaginary.	37
Figure 2.5	(a) Layered plate and (b) layered plate in contact with a fluid.	43
Figure 2.6	Guided wave actuation by an axisymmetric traction on the surface of an infinite plate.	54
Figure 2.7	Guided wave actuation by a straight line traction having finite length on the surface of an infinite plate.	57

Figure 2.8	The material variation profile (λ_L, μ_L, ρ) of an aluminum-zirconia functionally graded plate governed by Eq. (2.5.1) with different values of n	59
Figure 2.9	The through-thickness mode shape of the S_0 mode wave in an Aluminum-Zirconia functionally graded plate.	61
Figure 2.10	The through-thickness mode shape of the A_0 mode wave in an aluminum-zirconia functionally graded plate.	62
Figure 2.11	The through-thickness mode shape of the SH_0 mode wave in an aluminum-zirconia functionally graded plate.	62
Figure 2.12	The through-thickness mode shape of the S_0 mode wave in an aluminum-zirconia layered plate.	63
Figure 2.13	Beam patterns of guided waves generated by a line traction in Eq. (2.5.2) with $L = 2$ mm in the aluminum-zirconia functionally graded plate. The power-law material variation of the plate in Eq. (2.5.1) is governed by $n = 1$	64
Figure 2.14	Comparison beam patterns of guided waves generated by a line traction in Eq. (2.5.2) with $L = 2$ mm according to the different power-law material variation of the aluminum-zirconia functionally graded plate in Eq. (2.5.1).	65
Figure 2.15	Flexural wave excited by an axisymmetric vertical load (1 N/m) on a ring of radius $a = 2d$ in an aluminum plate of thickness $d = 1$ mm. Flexural waves were observed at $r = 100d$	69
Figure 3.1	Notations used for the extended boundary condition method illustrated in the horizontal plane (the x - y plane) of a plate when the field point \mathbf{r} of Eqs. (3.1.1) and (3.1.2) is located (a) in D_i and (b) in D_e	71

Figure 3.2	Illustrations for cross sections of (a) an elastic inclusion and (b) a through hole embedded in an exterior infinite plate. Thickness of the scatterer is same with that for the plate.	73
Figure 3.3	Illustrations for cross sections of (a) a thickness reduction and (b) a thickness increase embedded in an exterior infinite plate.	76
Figure 3.4	Guided wave incident on a scatterer by an externally applied traction.	82
Figure 3.5	Notations used for translation between coordinate systems.	82
Figure 3.6	Scattered fields from circular cylindrical partly through-hole (step thickness reduction) of radius $\lambda_{A0}/2$ in an aluminum plate of $d = 1$ mm thickness. The thickness reduction of the scatterer compared to an exterior plate is 50 %.	83
Figure 3.7	Scattered fields from circular cylindrical step thickness increase of radius $\lambda_{A0}/2$ in an aluminum plate of $d = 1$ mm thickness. The thickness increase of the scatterer compared to an exterior plate is 50 %.	84
Figure 3.8	Notation for a coordinate translation of fields in the cylindrical coordinate system.	86
Figure 3.9	Guided wave scattering in an infinite transversely isotropic plate of thickness d with the coordinate system.	107
Figure 3.10	(a) Decomposition of a scatterer into a finite number of sub-scatterers in the horizontal plane using the staircase approximation, (b) stacking a elastic inclusion material with a base (plate) material for the use of the EBCM, and (c) use of an equivalent circular cylindrical subscatterer for efficient T matrix calculation.	108

Figure 3.11	Near-scattered fields from the original square cylindrical scatterer and its equivalent circular cylindrical scatterer with its shape defined by $c = \lambda_{A0}/12$ and $h = d/2$ in Fig. 3.10(b) when an aluminum plate and a silicon inclusion are considered. The incident wave is actuated by line tractions as illustrated in Fig. 3.12 with $a_{\text{ext}} = \lambda_{A0}/2$, $r_{\text{ext}} = \lambda_{A0}$ and $t_{\text{ext}} = 1$ N/m at frequency·thickness = 1 MHz·mm. The scattered fields are calculated using the EBCM with $N = 12$ and observed at $r = \lambda_{A0}/6$ from the center of the scatterer.	113
Figure 3.12	Configuration for an incident wave generation. (a) Simultaneous actuation of symmetric and antisymmetric Lamb modes by a line traction on the top surface of the plate. (b) Antisymmetric Lamb mode wave actuation by line tractions on the top and bottom surfaces of the plate used in the numerical examples.	114
Figure 3.13	A wedge-shaped inclusion in a plate and its decomposition into multiple circular cylindrical subscatterers.	115

Figure 3.14	Scattered fields from a wedge-shaped silicon inclusion in an aluminum plate as in Fig. 3.13. The results with different values of subscatterer size c defined in Fig. 3.10 are compared. The relative values of c compared to the smallest wavelength λ_{\min} (λ_{A0} in this problem) are used. The shape of the wedge is defined by parameters $w_1 = \lambda_{A0}$, $w_2 = \lambda_{A0}/4$, $h_1 = 0$, and $h_2 = d$. The incident wave is actuated by line tractions as illustrated in Fig. 3.12(b) with $a_{\text{ext}} = \lambda_{A0}/2$, $r_{\text{ext}} = 5\lambda_{A0}$ and $t_{\text{ext}} = 1$ N/m at frequency·thickness = 1 MHz·mm. The scattered fields are observed at $r = 10\lambda_{A0}$ from the center of the scatterer on the top surface of the plate. For the suggested method, $N = 12$ guided wave modes are used.	116
Figure 3.15	The scattered fields from a wedge-shaped silicon inclusion in an aluminum plate as in Fig. 3.13. The results with different numbers of guided wave modes, N , used in the suggested method are compared. The shape of the wedge is defined by parameters $w_1 = \lambda_{A0}$, $w_2 = \lambda_{A0}/4$, $h_1 = 0$, and $h_2 = d$. The incident wave is actuated by line tractions as illustrated in Fig. 3.12(b) with $a_{\text{ext}} = \lambda_{A0}/2$, $r_{\text{ext}} = 5\lambda_{A0}$ and $t_{\text{ext}} = 1$ N/m at frequency·thickness = 1 MHz·mm. The scattered fields are observed at $r = 10\lambda_{A0}$ from the center of the scatterer on the top surface of the plate.	119
Figure 3.16	(a) The circular cylindrical inclusion, (b) the irregularly shaped cylindrical inclusion and (c) the spherical cap inclusion used to validate the suggested method.	120

Figure 3.17 Scattered fields from a circular cylinder silicon inclusion in an aluminum plate of $d = 1$ mm thickness at frequency of (a) 30 kHz, (b) 0.2 MHz and (c) 0.5 MHz. The shape of the inclusion is illustrated in Fig. 3.16(a) with $a = 4d$, and $h = d$. The incident waves are A_0 actuated by a circular traction as illustrated in Fig. 3.12(a) with $a_{\text{ext}} = 2d$, $b_{\text{ext}} = 10d$ and $t_{\text{ext}} = 1$ N/m. For the proposed method and the EBCM, the symmetric modes are not included. The scattered fields are observed at $r = 20d$ from the center of the inclusion. $N = 4$ guided wave modes are used for the proposed method and the EBCM. For 30 kHz, we used grid size $c = \lambda_{A0}/20$ instead of $c = \lambda_{A0}/12$ to avoid poor approximation of the curved surface. 121

Figure 3.18 Scattered field from an irregularly shaped silicon inclusion in an aluminum plate. The shape of the inclusion is illustrated in Fig. 3.16(b) and defined in the horizontal plane by Eq. (3.4.1) with $a_1 = 2\lambda_{A0}$, $a_2 = \lambda_{A0}/2$, and $h = d$. The incident wave is actuated by line tractions as illustrated in Fig. 3.12(b) with $a_{\text{ext}} = \lambda_{A0}/2$, $r_{\text{ext}} = 5\lambda_{A0}$ and $t_{\text{ext}} = 1$ N/m at frequency·thickness = 0.5 MHz·mm. The scattered fields are observed at $r = 10\lambda_{A0}$ from the center of the inclusion on the top surface of the plate. The inclusion is decomposed into 452 subscatterers and $N = 4$ guided wave modes are used for the suggested method. 122

Figure 3.19 Scattered field from an irregularly shaped silicon inclusion in an aluminum-zirconia functionally graded plate with the power-law material variation parameter $n = 1$. The shape of the inclusion is illustrated in Fig. 3.16(b) and defined in the horizontal plane by Eq. (3.4.1) with $a_1 = 2\lambda_{A0}$, $a_2 = \lambda_{A0}/2$, and $h = d$. The incident wave is actuated by line tractions as illustrated in Fig. 3.12(a) with $a_{\text{ext}} = \lambda_{A0}/2$, $r_{\text{ext}} = 5\lambda_{A0}$ and $t_{\text{ext}} = 1$ N/m at frequency-thickness = 0.5 MHz·mm. The scattered fields are observed at $r = 8\lambda_{A0}$ from the center of the inclusion on the top surface of the plate. The inclusion is decomposed into 452 subscatterers and $N = 8$ guided wave modes are used for the suggested method. 124

Figure 3.20 Scattered field from an irregularly shaped silicon inclusion in an aluminum-zirconia functionally graded plate with the power-law material variation parameter $n = 1$. The shape of the inclusion is illustrated in Fig. 3.16(b) and defined in the horizontal plane by Eq. (3.4.1) with $a_1 = 2\lambda_{A0}$, $a_2 = \lambda_{A0}/2$, and $h = d$. The incident wave is actuated by line tractions as illustrated in Fig. 3.12(a) with $a_{\text{ext}} = \lambda_{A0}/2$, $r_{\text{ext}} = 5\lambda_{A0}$ and $t_{\text{ext}} = 1$ N/m at frequency-thickness = 1 MHz·mm. The scattered fields are observed at $r = 8\lambda_{A0}$ from the center of the inclusion on the top surface of the plate. The inclusion is decomposed into 452 subscatterers and $N = 12$ guided wave modes are used for the suggested method. 125

Figure 3.21	Scattered field from a spherical-cap-shaped silicon inclusion in an aluminum plate. The shape of the inclusion is illustrated in Fig. 3.16(c) and defined by parameters $a = \lambda_{A0}$ and $h = d/2$. The incident wave is actuated by line tractions as illustrated in Fig. 3.12 with $a_{\text{ext}} = \lambda_{A0}/2$, $r_{\text{ext}} = 5\lambda_{A0}$ and $t_{\text{ext}} = 1$ N/m at frequency·thickness = 1 MHz·mm. The scattered fields are observed at $r = 10\lambda_{A0}$ from the center of the inclusion on the top surface of the plate. For the suggested method, the inclusion is decomposed into 452 subscatterers and $N = 12$ guided wave modes are used.	126
Figure A.1	The finite element meshes for circular domains used for validation of the proposed methods.	132

List of Tables

Table 3.1	Lamination types of plates and scatterers made of Mat 1 and Mat 2, I: isotropic, SL: symmetrically layered, NL: non-symmetrically layered.	117
Table 3.2	The number of guided wave mode expansion terms, $N(N_{\text{Lamb}}, N_{\text{SH}})$, needed to obtain a converged solution. S: symmetric guided wave, A: antisymmetric guided wave, C: nonsymmetric or coupled guided wave; I: isotropic, SL: symmetrically layered, NL: non-symmetrically layered.	118

Chapter 1

Introduction

1.1 Motivation

Plates are commonly used in aircraft, marine, civil structures and etc. Since thickness of a plate is small when compared with other dimensions, guided waves are observed when excited by external forces. Because guided waves travel long distance in bounded structures with a low attenuation, researchers have developed its ability to scan large areas in nondestructive evaluation (NDE) and structural health monitoring (SHM) techniques. These techniques have been studied for decades advancing towards simultaneous identification of location, size and shape of structural defects.

In the context of identifying defects, however, information contained in guided waves are still not being fully utilized. For example, when structural defects such as cracks or corrosions exist, guided waves are scattered by these defects. During scattering process, a guided wave mode is converted to many other guided wave modes; this phenomenon is called mode conversion. Furthermore, each guided wave mode has its own characteristics such as dispersion and mode shape that further complicate its utilization. Therefore, most of these mode conversion informations are left out for the sake of ease of analysis or neglected by the limitations imposed by transducers that could sense wave fields on structures; this may result in loss of important information

that can be used for reconstruction of defects.

On the other hand, researchers have investigated characteristics of guided wave to resolve these problems. For this reason, theoretical or numerical analysis techniques for calculation of scattering or dispersion relation could be used as supplements for interpreting experimental data. Methods for calculating dispersion relations for flat, cylindrical, spherical waveguides are based on a root-searching algorithm or an eigenvalue solver and have been well established [1]–[5]. When it come to choice of scattering analysis techniques, numerical analyses techniques based on differential equations such as the finite element method are powerful in terms of its versatility since it can be used for any complex geometry. However, in most cases, computational cost for this method exceed the current state of the computing power because the domain in which waves propagate should be discretized and absorbing layer around this domain should be also modeled to simulate an infinite space. Furthermore, many reconstruction schemes for bulk or guided waves require scattered fields obtained from incident waves of tens or hundreds of different angles [6]–[9]. Even with state of the art powerful computer and an efficient matrix equation solver, a guided waves scattering analysis by the FEM for single incident wave requires at least a number of minutes to an hour, and furthermore a substantial amount of memory is also needed. (For more details about drawbacks of differential equation solvers for wave problems such as the finite element or the finite difference method, see, e.g., [10].)

In this regard, theoretical or semi-analytical (semi-theoretical) analysis techniques based on integral equations are attractive alternatives to numerical analyses techniques based on differential equations. Unfortunately, these methods become more complicated when applied to more complex geometries of waveguides or scatterers. However, since even simple waveguide geometries that can be described with moderate mathematical complexity commonly appear in structures, it may be still worth putting efforts into theoretical techniques for relatively simple geometries.

Therefore, in this dissertation, we will develop theoretical analysis techniques for radiation and scattering of guided waves in flat plates that can be regarded as the most basic waveguiding structure for studying guided wave transducers and defect imaging methods. Before doing that, we will discuss in the next section about the current state of the development for theoretical analysis techniques.

1.2 Background literatures

Many analysis techniques for scattering problems have been developed and each technique has its own strength. Generally, the applicable range of each technique depends on the size of a scatterer relative to the wavelength [11]. When the sizes of scatterers are comparable to wavelength, these scatterers are called to be in the resonance region. Among many other method, the transition matrix (T matrix) method is one of powerful techniques when dealing with scatterers in the resonance region and became popular in analyzing electromagnetic wave scattering by particles [10]–[15].

Analysis techniques for bulk wave scattering problems have been highly advanced and analysis techniques for guided wave problems have also been paid attention to for decades in regard to ocean acoustics and seismology [1], [2]. But, when compared to other fields, it wasn't until recently that researchers paid them attention in fields of NDE and SHM [16].

Especially, the T -matrix method almost has not been studied for problems regarding NDE and SHM techniques based on elastic guided waves. The major issue of NDE and SHM techniques are identifying and imaging defects in plates, pipes or thin shells in presence of built-in inhomogeneities including holes, rivets, or weldings. To simultaneously obtain a certain level of imaging resolution, long range scanning ability and efficient electro-mechanical transduction, researchers have used elastic guided waves in ultrasonic frequency range up to a few MHz. In this case, defects, built-in inhom-

geneties and wavelengths are in the same order of magnitude.

For this reason, many of scattering problems in NDE and SHM can be considered to be in the resonance region, and therefore the T -matrix method can be useful in dealing with these problems. Since researchers have put efforts into studying on the T -matrix methods for bulk waves, it is worth briefly discussing state of the art T -matrix method for bulk waves before going into further about guided wave problems.

1.2.1 Review of advances in the T matrix formalism

For a external scattering problem, we can define the T matrix \mathbf{T} as in the following equation

$$\alpha = \mathbf{T}\mathbf{A}. \quad (1.2.1)$$

that operates on the coefficient vector \mathbf{A} of a incident field and results in the coefficient vector α of a scattered field. For example, in the two-dimensional linear acoustic wave fields, we seek, for a given incident field u^{Inc} , a scattered field u^{Sc} satisfying the time-harmonic wave equation for a scattered field (pressure field or, displacement or velocity potential field) in the external region D_e having a wavenumber k [11], [15],

$$\nabla^2 u^{\text{Sc}} + ku^{\text{Sc}} = 0 \text{ in } D_e, \quad (1.2.2)$$

and also satisfying the Sommerfeld radiation condition

$$r^{1/2} \left(\frac{\partial u^{\text{Sc}}}{\partial r} - iku^{\text{Sc}} \right) \rightarrow 0 \text{ as } r \rightarrow \infty. \quad (1.2.3)$$

Then, u^{Inc} and u^{Sc} are approximated as follows:

$$u^{\text{Inc}} = \sum_{m=-\infty}^{\infty} A_m \varphi_m(\mathbf{r}), \quad u^{\text{Sc}} = \sum_{m=-\infty}^{\infty} \alpha_m \bar{\varphi}_m(\mathbf{r}), \quad (1.2.4)$$

where A_m and α_m are the coefficients of the expansions and therefore $\mathbf{A} = \{A_m\}$ and $\alpha = \{\alpha_m\}$. In the above expansions, the basis functions are the solutions of the Helmholtz equation in the two-dimensional polar coordinate system. Explicitly we use

the regular cylindrical wavefunctions $\varphi_m(\mathbf{r}) = J_m(kr)e^{im\theta}$ which is regular at the origin and the singular cylindrical wavefunctions $\bar{\varphi}_m(\mathbf{r}) = H_m^{(1)}(kr)e^{im\theta}$ which is singular at the origin located somewhere in the internal region D_i and satisfies the radiation condition in Eq. (1.2.3). Then, the problem is to find the matrix \mathbf{T} for a scatterer with a boundary S subject to certain boundary conditions.

Variety of methods exist for the T matrix calculation for an arbitrarily shaped scatterer. The formulation using the T matrix for arbitrarily shaped scatterers was first rendered from the extended boundary condition method (EBCM, also called the null-field method) for a homogeneous scatterer developed by Waterman [12]. In the EBCM, the incident field and the surface field on S are related through a particular form of the integral equations so-called the null-field equation. Then, the surface fields are expanded in terms of basis functions such as $\varphi_m(\mathbf{r})$ or $\bar{\varphi}_m(\mathbf{r})$. After the surface fields are found, the scattered fields are obtained from the integral representation of the Huygens principle. The EBCM, however, has inherent instability when dealing with scatterers of some geometrical complexity or high aspect ratio, or high-frequency range problems. Specifically, when these problems are concerned, the EBCM requires the use of high-order Hankel functions that rapidly grow when $m > kr$ resulting in poor matrix conditioning. Therefore, researchers have sought alternative methods to overcome these instabilities.

One of the alternatives applicable to transmission boundary-value problems (when the boundary conditions allow transmission of waves into D_i) is the use of basis functions distributed at multiple coordinate origins [11], [17], [18]. Using this method, use of high order Hankel functions can be avoided resulting in better matrix conditioning that cannot be achieved by the EBCM.

The most flexible alternative to the EBCM is to decompose a scatterer into multiple subscatterer and apply a multiple scattering theory to these subscatterers [13], [19]–[24]. This method originated from two similar but different approaches. One of

them is so-called the discrete dipole approximation in electromagnetic field theory developed by Purcell [25]. In this approach, a scatterer is assumed as an assembly of point-like dipoles and the relation between the incident and scattered fields for each dipole are characterized by a quantity called Clausius-Mossotti polarizability. Another approach originated from the fact that, in the two-dimensional space, a rectangular scatterer small compared to the wavelength can be replaced with an equivalent circular scatterer of the same area [26]. Adopting this approach to the T matrix formalism is done by Chew [19]. These approaches are applicable to a scatterer of any size and shape. Furthermore, subscatterer methods can be accelerated by fast numerical algorithms such as the fast Fourier transform, the fast recursive algorithm, or the fast multipole method when a number of subscatterers are used [19], [21], [23]. Currently these methods are the mostly flexible and efficient method for calculating the T matrix for a scatterer of an arbitrary shape when dealing with bulk waves.

Another alternative is to use the method of moment (MOM) also called the boundary element method (BEM) in mechanical engineering field in calculation of the T matrix. Because local basis functions are used in the MOM, it is possible to handle infinitely scatterers of arbitrary shape that has Neumann or Dirichlet condition that cannot be handled by the EBCM or the subscatterer method. The connection between the MOM and the T matrix formalism was studied by Gurel and Chew [27].

The finite element method (FEM) can also be adopted into calculation of the T matrix [28]–[30]. In this approach, for example in two-dimensional acoustic problem, the virtual circular boundary is first set to encircle the scatterer. Then, the fields in the external region are described by sum of $\bar{\varphi}_m(\mathbf{r})$ and the fields in the internal region described by the FEM. And the boundary conditions are matched on the virtual boundary. Furthermore, this problem can be formulated to create sparse matrices [28]. Therefore, this approach is also flexible and efficient. However, since no comparison have been made between subscatterer methods with fast algorithms and hybrid FEM

method, we cannot tell which is better at this moment.

In another approach called the point matching method (PMM), boundary conditions are matched at discrete points [31] as many as the number of unknowns but many reports have shown that this method is not stable [32]. Better stability can be achieved if the number of matching points exceeds that of unknowns resulting in overdetermined system of equations. However, since for such system only a least-square solution can be calculated, there yet seems to be no realization of calculating the T matrix through this method.

1.2.2 Analytic or semi-analytic methods for scattering problems in elastic plates

In this subsection, we will briefly discuss about advances in analysis techniques for scattering problems in elastic plates. Particularly, we narrow down our interest to developments related to the T matrix formalism that adopts multipole series expansion of fields.

Analysis techniques for guided waves in elastic plates that adopt multipole series expansion can be divided into two approaches. One is based on the three-dimensional elasticity and the other is based on the approximate plate theories. Methods based on the three-dimensional elasticity would be exact, at least in theory, in any frequency range. However, methods based on an approximate plate theory are more efficient due to the smaller number of degree of freedom. Anyway since both approaches describe the same phenomena, they are complementary to each other — an advance in one approach results in an advance in other approach —.

Several approximate plate theories exist. Kirchhoff's theory for describing flexural waves is among the most frequently used approach. Poisson's theory describes extensional waves and shear horizontal waves. These two theories use the lowest order approximation, and therefore these are accurate only at very low frequency. Mindlin's

theory adds an additional degree of freedom to Poisson's theory resulting in extend applicable frequency range. However it is still only accurate at near non-dispersive region of S_0 (the lowest symmetric Lamb wave). Anyway, use of the approximate plate theories reduces the number of degree of freedom (DOF) by average 20 ~ 30% when compared to methods based on the three-dimensional elasticity. For example, for reasonably accurate description of guided waves at 500kHz · mm, we can use Mindlin and Kane's theory for extensional and shear horizontal waves that has 3 DOF and Mindlin's theory for flexural waves that 3 DOF, therefore a total of 6 DOF. In case of the three-dimensional elasticity theory, a total of 8 DOF [33] is required. Another advantage of the approximate plate theories is that it sometimes gives more insight into guided wave phenomena, for example when a certain analytic property is derived.

Here, we list some of studies based on the approximate plate theories. Most of them uses Rayleigh's hypothesis. Rayleigh's hypothesis is an assumption that a series expansion of the scattered wave as in Eq. (1.2.4) are valid also on S . The fact is that it is not obvious whether the waves in the region between the scatterer surface S and its circumscribed circle S^+ is outgoing or standing waves and there is still on-going debate on this assumption [13], [32]. Leviatan et al. studied scattering of a flexural wave (the lowest-order antisymmetric wave) by an inclusion of arbitrary shape using fictitious point sources [34]. Norris and Vemula derived the energy conservation equation for scattering of the flexural wave and discussed the behavior of a rigid inclusion and a hole [35]. McKeon and Hinders studied scattering of the extensional wave (the lowest-order symmetric wave) [36]. Grahn proposed a method that couples Poisson's theory and Kirchhoff's theory to analyze scattering of Lamb and shear-horizontal (SH) waves by a partly through hole [33]. Celga used Mindlin's theory instead of Kirchhoff's theory to achieve better solution accuracy in some frequency range [37]. Wang and Chang extended Kane-Mindlin theory for extensional wave to the case of transversely isotropic material [38]. Lee and Chen proposed the null-field integration equa-

tion method to analyze scattering of a flexural wave [39]. Rose and Wang developed an imaging method based on the Born approximation [40]. In addition to those, theoretical analyses have been conducted to obtain the effective wavenumber of a plate with a number of small scatterers [41], [42].

However, although the methods based on the approximate plate theories have the advantage of relatively small degrees of freedom (20 ~ 30% DOF reduction as we mentioned above) when compared to those of methods based the three-dimensional elasticity, even at low frequency there are situations that requires a method based on the three-dimensional elasticity such as when fluid-loaded plates should be handled. Up to now, methods based on Rayleigh's hypothesis have been appeared in literatures. The major issue in these researches has been the selection of the projection functions (the trial functions) onto which the boundary conditions of the cavity are projected. Diligent et al. analyzed the case of a circular through hole and used trigonometric functions as the projection functions [43]. Grahn extended the previous method to a circular part-through hole by considering the transmitted wave into the region beneath or above the scatterer [33]. In this work, Grahn also compared the results from the three-dimensional elasticity with those from the approximate plate theory, concluding that the method based on the low order approximate plate theories is valid only for a frequency·thickness range of <200 kHz·mm. Moreau et al. extended the aforementioned works to a cavity with an arbitrary shape in the horizontal plane by employing a Fourier series expansion for the circumferential-direction-dependent functions [44], [45]. They also suggested that the use of the displacement vectors as the projection functions instead of the trigonometric functions reduces the number of guided wave modes required for expansion and thus results in better convergence.

1.3 Research objectives

Although many efforts have been made to improve analysis techniques for guided waves in plates as we have mentioned in the preceding section, it still cannot handle a variety of shapes and sizes. For example, when the previously mentioned methods are applied to scatterers with aspect ratios > 4 in the horizontal plane of a plate, or with a radial size $> \lambda_{\min}/2$ (where λ_{\min} is the minimum wavelength), numerical problems such as matrix ill-conditioning occur when solving the linear system of equations.

These numerical problems are mainly due to the behavior of Hankel functions and Bessel functions. For example, $H_m^{(1)}(kr)$ decrease rapidly as m increases when $m > |kr|$ and $J_m(kr)$ becomes very large when k has an imaginary part comparable to or larger than the real part. These behaviors easily make the system matrix to be inverted ill-conditioned. And since Bessel function with a generally complex argument is necessary for describing nonpropagating modes of guided waves, the method of Rayleigh hypothesis is particularly more unstable for guided wave problems.

Another inevitable difficulty is observed particularly in guided wave problems when dealing with a scatterer of a varying thickness. This problem is due to the structure of the guided wave basis functions and can be stated as follows. The guided wave basis functions are composed of the thickness-dependent functions and the carrier functions. The thickness-dependent functions which only appears in guided wave problems are the eigenfunctions of governing equations that describe the motion of the vertical section of the plate. These eigenfunctions for Lamb and SH wave have been proven to be complete on the vertical section of the plate, but there seems no reason that these eigenfunctions are complete as to considering arbitrary lines (or surfaces). On the other hand, the bulk wave basis functions do not pose the same problem.

So far, it seems that no effort have been made in regard of overcoming these difficulties. Therefore, we now face a question of “*how to deal with scatterers of a wide*

range of shapes and sizes".

These difficulties can be undertaken through the subscatterer method that decompose scatterer into multiple subscatterer as mentioned in Section 1.2.1. By introducing the subscatterer method, the two major restrictions caused by the behaviors of Bessel and Hankel functions and the structure of the basis function can be simultaneously relaxed. The former problem is expected to be resolved since in subscatterer method only Hankel functions of orders up to 2 are used. The latter problem can be resolved because the even continuous thickness variation of scatterer is approximated as a piecewise constant variation among subscatterers.

To realize this idea, we focus specifically on the T matrix formalism based on using the three-dimensional elasticity theory to deal with general situations appearing in guided wave problems.

For calculation of the T matrix for a subscatterer, it is possible to adopt the method of Rayleigh's hypothesis mentioned in Section 1.2.2. However the system matrix equations given in Ref. [33], [45] do not directly yield the T matrix. Furthermore, it seems that overall formulations including detailed description of the methods and choice of trial functions can be more simplified if we adopt the extended boundary condition method (EBCM) [12]. For these reasons, we discuss details about the EBCM and multiple scattering theory based on the T matrix formalism after deriving a particular form of Green's function required for use in the EBCM.

1.4 Thesis outline

The dissertation is organized as follows. In Chapter 2, the Green's function and the basis functions for guided waves in a plate are discussed. In Chapter 3, a scattering theory based on the T -matrix formalism is presented.

In Section 2.2, the multipole expansion of the Green's function that will be used

in the EBCM is derived by using integral transform and the properties of the derived Green's function is also derived. In Section 2.3, the detailed explanation related to calculation of the Lamb and SH wave basis functions based on the pseudospectral collocation method is presented. In Section 2.4, analytic models for acutators typically used in ultrasonic guided wave techqniue are presented based on the derived Green's function.

In Section 3.1, the extended boundary condition method (EBCM) based on the null-field integral equation for evaluation of T matrix for a single scatterer is discussed. In Section 3.2, a simple multiple scattering theory based on the T -matrix formalism is discussed. In Section 3.3, the properties of the general T matrix is presented after deriving the real and complex orthogonality relation between the guided wave basis functions in the cylindrical coordinate system. In Section 3.4, the subscatterer method to extend the applicable size and shape range is presented and numerical examples are provide.

Chapter 2

Green's function for guided waves in a flat transversely isotropic plate

In this chapter, we will discuss about the basis functions and the Green's functions that will be used for solving scattering problems in flat transversely isotropic plates. First, we will derive the Green's function in the cylindrical coordinate and in the Cartesian coordinate by expanding it in terms of the basis functions; the derived Green's function in the cylindrical coordinate will be used for scattering analyses based on the transition matrix method in Chapter 3. And next, we will explain a method for calculating the basis functions by numerical methods. Then, we will cover problems related to radiation of guided waves by surface tractions since guided wave transducer are effectively modeled as surface tractions and the Green's function is useful for solving radiation problems. To validate the theory, we provide examples which compare results obtained from the theory with those from the finite element method and the approximate plate theories.

2.1 Backgrounds

The method of Green's functions is an effective way to solve inhomogeneous partial differential equations (PDEs) including wave equations. For wave propagation prob-

lems in an elastic plate which are the subject of this study, earlier efforts to obtain Green's functions used either approximate plate theories or three-dimensional elastodynamic equations with plain-strain or axial-symmetry assumptions [46]–[49].

By using three-dimensional elastodynamic equations, among others, Liu and Xi [50] derived the time-domain Green's function for anisotropic layered materials in the Cartesian coordinates based on the eigenfunction expansion technique. By using the elastodynamic reciprocity, Tan and Auld [51] derived the Green's functions for an isotropic plate in the Cartesian coordinates and Achenbach and Xu [52], in the cylindrical coordinates. Bai [53] derived the Green's functions for a layered isotropic plates by using the Fourier transform in the Cartesian coordinate system and converting the resulting expressions into those in the cylindrical coordinate by the coordinate transform. The Green's functions for seismic problems derived by Aki and Richard [1] and Hisada [54] and Guzina [55] may be extended to wave problems in a plate.

In this study, we aim to derive the Green's function in a certain form that is convenient for using the transition matrix (T-matrix) method [56], [57]. Specifically, the bilinear form composed of the regular and singular eigenfunctions in the cylindrical coordinates is known to be effective. Although the above mentioned earlier works presented the Green's function in different forms, none of them can be directly used in the T-matrix method. To this end, we adopt the method suggested by Tai [58] for electromagnetic wave problems.

While the method by Tai [58] has been used to deal with electromagnetic guided wave problems, it appears that no earlier work has utilized it to derive the Green's function for an elastic plate, a mechanical counterpart of an electromagnetic waveguide. The underlying concept of the method in Tai [58] is basically the same as that by Liu and Xi [50] who derived the Green's function in the Cartesian coordinate, but we derive the Green's function directly in the cylindrical coordinates. Because we expand the Green's function in terms of the waveguide mode eigenfunctions, it is important to

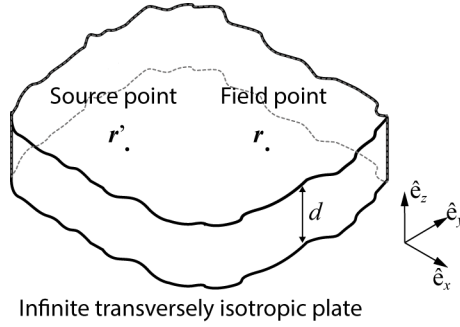


Figure 2.1 Guided wave excitation in an infinite plate of the thickness d with the coordinate system.

establish the orthogonality of the eigenfunctions for further development. The resulting orthogonality relation given in the transformed space is different from the well-known bi-orthogonality [59], [60] of the eigenfunctions of an elastic plate.

2.2 Derivation of the Green's function

In this section, the Green's functions will be derived by the eigenfunction expansion method. To begin with, let us consider an infinite linear-elastic plate of thickness d with a generic field point $\mathbf{r} = (r, \theta, z) = (x, y, z)$ as illustrated in Fig. 2.1. The domain V under consideration is defined to be $0 \leq r < \infty$, $0 \leq \theta < 2\pi$ and $0 \leq z \leq d$ in the Cylindrical coordinate system, $0 \leq x < \infty$, $0 \leq y < \infty$ and $0 \leq z \leq d$ in the Cartesian coordinate system. The cylindrical coordinates (r, θ, z) are converted to the Cartesian coordinates (x, y, z) using $x = r \cos \theta$ and $y = r \sin \theta$. Displacement $\mathbf{u}(\mathbf{r})$ and stress $\boldsymbol{\sigma}(\mathbf{r})$ in the plate satisfy the following three-dimensional equations for a plate made of an elastic isotropic medium with elastic properties of the Lamé constants λ , μ and the mass density ρ :

$$\nabla \cdot \boldsymbol{\sigma}(\mathbf{r}) + \rho \omega^2 \mathbf{u}(\mathbf{r}) = 0. \quad (2.2.1)$$

The traction-free conditions on the top and bottom surfaces ($z = 0, d$) are expressed as

$$\sigma_{zr} = \sigma_{z\theta} = \sigma_{zz} = 0, \text{ at } z = 0, d. \quad (2.2.2a)$$

or

$$\sigma_{zx} = \sigma_{zy} = \sigma_{zz} = 0, \text{ at } z = 0, d. \quad (2.2.2b)$$

In writing Eq. (2.2.1) solution dependency on time t is omitted by assuming harmonic motion in the form of $e^{-i\omega t}$ where ω is angular frequency and $i = \sqrt{-1}$.

If a point excitation source is located at $\mathbf{r}' = (r', \theta', z') = (x', y', z')$, the dyadic displacement Green's function $\mathbf{G}(\mathbf{r}|\mathbf{r}')$ and the triadic stress Green's function $\Sigma(\mathbf{r}|\mathbf{r}')$ satisfy the following equation,

$$\nabla \cdot \Sigma(\mathbf{r}|\mathbf{r}') + \rho \omega_{\text{ext}}^2 \mathbf{G}(\mathbf{r}|\mathbf{r}') = -\mathbf{I} \delta(\mathbf{r} - \mathbf{r}'), \quad (2.2.3)$$

with the boundary condition given by Eq. (2.2.2). The symbol ω_{ext} in Eq. (2.2.3) denotes the excitation angular frequency and the symbol \mathbf{I} , a 3×3 identity tensor and $\delta(\mathbf{r} - \mathbf{r}')$, the Dirac delta function. It should also be noted that the operator ∇ in Eq. (2.2.3) operates only on the terms related to \mathbf{r} .

2.2.1 Green's function in the cylindrical coordinate system

In this section, the Green's function is expanded in terms of the cylindrical coordinate system. The resulting Green's function is expressed in the form of summation over multipoles (e.g., monopole, dipole, qudrupole) in the horizontal plane of a plate. This form is useful, because multipolar terms are truncated at some order and thus, it is easy to find the dominant terms of the resulting field. In addition to this, multipolar expansion form will be used in theoretical scattering analysis.

2.2.1.1 Orthogonality of eigenfunctions for a fixed wave number k

Here, we first introduce an integral transform that will be used to expand an arbitrary wave field in a plate in terms of the guided wave eigenfunctions. We start from the well-known fact that an arbitrary three-dimensional displacement field $\mathbf{u}(\mathbf{r})$ in an elastic plate can be expressed in terms of three independent scalar potentials (see, e.g., Morse and Feshbach [61] and Miklowitz [62]). Because the plate in consideration is an infinite plate, the potentials can be expressed through the Hankel transform in r with the corresponding transform variable k , the complex Fourier series in the circumferential coordinate (θ) with the integer index m denoting the Fourier number ($m = 0, \pm 1, \pm 2, \dots$). Along the z direction, the displacement field will be expanded in the Lamb and shear-horizontal (SH) modes [60], [62], [63] that satisfy the traction-free conditions on the top and bottom surfaces. The mode number in the z direction will be indicated by the nonzero positive integer index n ($n = 1, 2, \dots$). If these expansions in r , θ and z are employed, $\mathbf{u}(\mathbf{r})$ can be written as the following inverse transform as

$$\mathbf{u}(\mathbf{r}) = \frac{1}{2\pi} \int_0^\infty k dk \sum_{n,m} A_n^m(k) \varphi_n^m(k, \mathbf{r}), \quad (2.2.4)$$

where $A_n^m(k)$ are unknown expansion coefficients to be determined. The kernel $\varphi_n^m(k, \mathbf{r})$ of the above integral transform is the eigenfunction of the following eigenvalue equation,

$$\nabla \cdot \boldsymbol{\sigma}(\varphi_n^m(k, \mathbf{r})) + \rho \omega_n^2(k) \varphi_n^m(k, \mathbf{r}) = 0, \quad (2.2.5a)$$

and satisfies the traction-free boundary conditions in Eq. (2.2.2a). In the above equation, $\nabla \cdot \boldsymbol{\sigma}$ may be viewed as an operator acting upon the eigenfunction $\varphi_n^m(k, \mathbf{r})$ because the stress field $\boldsymbol{\sigma}$ is explicitly written in terms of $\varphi_n^m(k, \mathbf{r})$ through the constitutive relation and the strain-displacement relation. In Eq. (2.2.5a), $\omega_n(k)$ represents the n^{th} (angular) eigenfrequency for some k and $\varphi_n^m(k, \mathbf{r})$, the corresponding eigenfunction. It is emphasized that there exist a number of real eigenvalues of ω_n for a given radial

wavenumber k . Note that ω_{ext} in Eq. (2.2.3) is the excitation frequency by an external source while $\omega_n(k)$ in Eq. (2.2.5) denotes eigenvalues determined from the dispersion curve of a plate for a given k .

For future compact notation, the following abbreviations will be used whenever possible:

$$\sigma_n^m = \sigma(\varphi_n^m(k, \mathbf{r})); \varphi_n^m = \varphi_n^m(k, \mathbf{r}).$$

With these notations, Eq. (2.2.5a) is rewritten as

$$\nabla \cdot \sigma_n^m + \rho \omega_n^2(k) \varphi_n^m = 0. \quad (2.2.5b)$$

Obviously the n^{th} eigenfrequency $\omega_n(k)$ satisfies the dispersion relations [60], [62], [63] for the Lamb or SH waves for a given mode n and a wavenumber k . The explicit forms of regular eigenfunctions $\varphi_n^m(k, \mathbf{r})$ are given by

· Lamb type wave mode:

$$\varphi_n^m(k, \mathbf{r}) = \left\{ \begin{array}{c} U_n(k, z) J'_m(kr) \\ U_n(k, z) im J_m(kr) / kr \\ W_n(k, z) J_m(kr) \end{array} \right\} e^{im\theta}, \quad (2.2.6)$$

· Shear-horizontal (SH) wave mode:

$$\varphi_n^m(k, \mathbf{r}) = \left\{ \begin{array}{c} V_n(k, z) im J_m(kr) / kr \\ -V_n(k, z) J'_m(kr) \\ 0 \end{array} \right\} e^{im\theta}, \quad (2.2.7)$$

where $J_m(kr)$ are the Bessel functions of the first kind of order m and the prime indicates derivative with respect to the argument. In Eqs. (2.2.6) and (2.2.7), three displacement components in the r , θ and z coordinates are given in order and the method for obtaining $U_n(k, r)$, $W_n(k, z)$ and $V_n(k, z)$ are provided in Section 2.3.

To expand the dyadic Green's function $\mathbf{G}(\mathbf{r}|\mathbf{r}')$ in terms of $\varphi_n^m(k, \mathbf{r})$ through the integral transform (2.2.4), it is important to show the orthogonality of $\varphi_n^m(k, \mathbf{r})$ with

respect to n , m and k . To this end, let us consider two sets of equations Eq. (2.2.5b) for different indices and wavenumbers:

$$\nabla \cdot \boldsymbol{\sigma}_n^m + \rho \omega_n^2(k) \boldsymbol{\varphi}_n^m = 0, \quad (2.2.8a)$$

$$\nabla \cdot \boldsymbol{\sigma}_{n'}^{-m'} + \rho \omega_{n'}^2(k') \boldsymbol{\varphi}_{n'}^{-m'} = 0. \quad (2.2.8b)$$

The negative sign in $(-m')$ can be viewed as the complex conjugate of the expressions with m' . The dot-product of Eq. (2.2.8b) with $\boldsymbol{\varphi}_n^m$ can be subtracted from the dot-product of Eq. (2.2.8a) with $\boldsymbol{\varphi}_{n'}^{-m'}$ to yield (after some manipulations)

$$\nabla \cdot (\boldsymbol{\sigma}_n^m \cdot \boldsymbol{\varphi}_{n'}^{-m'} - \boldsymbol{\varphi}_n^m \cdot \boldsymbol{\sigma}_{n'}^{-m'}) = \rho [\omega_{n'}^2(k') - \omega_n^2(k)] \boldsymbol{\varphi}_n^m \cdot \boldsymbol{\varphi}_{n'}^{-m'}. \quad (2.2.9)$$

Integrating Eq. (2.2.9) over V ($0 \leq r < \infty$, $0 \leq \theta < 2\pi$, $0 \leq z \leq d$) results in

$$\int_V dv \nabla \cdot (\boldsymbol{\sigma}_n^m \cdot \boldsymbol{\varphi}_{n'}^{-m'} - \boldsymbol{\varphi}_n^m \cdot \boldsymbol{\sigma}_{n'}^{-m'}) = \int_V dv \rho [\omega_{n'}^2(k') - \omega_n^2(k)] \boldsymbol{\varphi}_n^m \cdot \boldsymbol{\varphi}_{n'}^{-m'}. \quad (2.2.10)$$

The volume integral $\int_V dv \nabla \cdot (\boldsymbol{\sigma}_n^m \cdot \boldsymbol{\varphi}_{n'}^{-m'} - \boldsymbol{\varphi}_n^m \cdot \boldsymbol{\sigma}_{n'}^{-m'})$ can be reduced by the divergence theorem to a surface integral $\int_S ds \{ \mathbf{n} \cdot \boldsymbol{\sigma}_n^m \cdot \boldsymbol{\varphi}_{n'}^{-m'} - \boldsymbol{\varphi}_n^m \cdot [\mathbf{n} \cdot \boldsymbol{\sigma}_{n'}^{-m'}] \}$ where $\mathbf{n} \cdot \boldsymbol{\sigma}_n^m$ is the traction vector on the boundary surface S . Because of the traction-free surface condition ($\mathbf{n} \cdot \boldsymbol{\sigma} = 0$) at $z = 0, d$ and the decaying far-field asymptotic behavior of the stress and displacement eigenfunctions (see Eqs. (2.2.6) and (2.2.7) for their explicit expressions) on the circular cylindrical surface as $r \rightarrow \infty$, the left-hand side of Eq. (2.2.10) identically vanishes.

To simplify the right-hand side (RHS) of Eq. (2.2.10) and better interpret the resulting equation, let us consider the volume integration of RHS in Eq. (2.2.10):

$$\int_V dv (\dots) = \int_0^d dz \int_0^\infty r dr \int_0^{2\pi} d\theta (\dots).$$

At this point, we should consider three cases for defining orthogonality relations; between two Lamb type wave modes, between two SH wave modes and between a Lamb type mode and an SH mode. We first derive the orthogonality relation between

two Lamb type wave modes. By substituting the explicit expression of eigenfunctions φ_n^m in Eq. (2.2.6) into RHS of Eq. (2.2.10) and integrating over θ , we have the following equation

$$0 = 2\pi\delta_{mm'} \int_0^d dz \int_0^\infty r dr \int_0^\infty dk \left[U_n(k, z) U_{n'}(k', z) \frac{\partial J_m(kr)}{\partial r} \frac{\partial J_{-m'}(k'r)}{\partial r} \right. \\ \left. + U_n(k, z) U_{n'}(k', z) m \frac{J_m(kr)}{r} m' \frac{J_{-m'}(k'r)}{r} + W_n(k, z) W_{n'}(k', z) J_m(kr) J_{-m'}(k'r) \right]. \quad (2.2.11)$$

The recurrence relations of the Bessel function given as,

$$J_m(kr) = \frac{kr}{2m} [J_{m-1}(kr) + J_{m+1}(kr)], \quad (2.2.12a)$$

$$\frac{\partial J_m(kr)}{\partial r} = \frac{k}{2} [J_{m-1}(kr) - J_{m+1}(kr)], \quad (2.2.12b)$$

$$J_{-m}(kr) = (-1)^m J_m(kr), \quad (2.2.12c)$$

simplify Eq. (2.2.11) as follows [58]:

$$0 = \int_V dv \rho [\omega_{n'}^2(k') - \omega_n^2(k)] \varphi_n^m \cdot \varphi_{n'}^{-m'} \\ = [\omega_{n'}^2(k') - \omega_n^2(k)] \int_0^d dz \int_0^\infty r dr 2\pi\delta_{mm'} (-1)^{m'} \\ \times \rho [U_n(k, z) U_{n'}(k', z) J_{m-1}(kr) J_{m-1}(k'r) / 2 \\ + U_n(k, z) U_{n'}(k', z) J_{m+1}(kr) J_{m+1}(k'r) / 2 \\ + W_n(k, z) W_{n'}(k', z) J_m(kr) J_m(k'r)]. \quad (2.2.13)$$

For additional simplification of Eq. (2.2.13), the following relation [61] is used:

$$\frac{\delta(k-k')}{k'} = \int_0^\infty r dr J_m(kr) J_m(k'r), \quad (2.2.14)$$

where $\delta(k-k')$ represents the Dirac delta function. Substituting Eq. (2.2.14) into Eq. (2.2.13) yields,

$$0 = [\omega_{n'}^2(k') - \omega_n^2(k)] 2\pi \frac{\delta(k-k')}{k'} \delta_{mm'} (-1)^{m'} \\ \times \int_0^d dz \rho [U_n(k, z) U_{n'}(k', z) + W_n(k, z) W_{n'}(k', z)]. \quad (2.2.15)$$

Now let us further analyze Eq. (2.2.15) by integrating over the positive real-line of the k' space ($\int_0^\infty k' dk'(\dots)$) and summing over all m' :

$$0 = [\omega_{n'}^2(k) - \omega_n^2(k)] 2\pi(-1)^m \times \int_0^d dz \rho [U_n(k, z)U_{n'}(k, z) + W_n(k, z)W_{n'}(k, z)]. \quad (2.2.16)$$

Equation (2.2.16) states that if $\omega_{n'}^2(k) \neq \omega_n^2(k)$, i.e., if $n \neq n'$ for a given k , the integral over z in Eq. (2.2.16) must vanish. This implies that the eigenfunctions $\varphi_n^m(k, \mathbf{r})$ are orthogonal with respect to each other if $n \neq n'$ over the volume integral. Therefore, in terms of the eigenfunctions, the general form of the orthogonality relation can be stated as

$$\int_V dv \rho \varphi_n^m(k, \mathbf{r}) \cdot \varphi_{n'}^{-m'}(k', \mathbf{r}) = (-1)^{m'} 2\pi \frac{\delta(k - k')}{k'} \delta_{nn'} \delta_{mm'} E_{n'}(k'), \quad (2.2.17)$$

where $E_n(k)$ is defined as

$$E_n(k) = \int_0^d dz \rho [U_n^2(k, z) + W_n^2(k, z)]. \quad (2.2.18a)$$

The orthogonality relation between two SH modes are very similar to the case of two Lamb type modes except that we have

$$E_n(k) = \int_0^d dz \rho V_n^2(k, z). \quad (2.2.18b)$$

Now, we consider the orthogonality relation between a Lamb type mode and an SH mode. By substituting the explicit expression of eigenfunctions φ_n^m in Eqs. (2.2.6) and

(2.2.7) into RHS of Eq. (2.2.10) and integrating over θ , we have the following equation

$$\begin{aligned}
& 2\pi\delta_{mm'}(-1)^m \int_{-h}^h dz \int_0^\infty r dr \int_0^\infty dk \\
& \times \left[V_n(k, z) U_{n'}(k', z) im \left\{ \frac{J_m(kr)}{r} \frac{\partial J_m(k'r)}{\partial r} + \frac{\partial J_m(kr)}{\partial r} \frac{J_m(k'r)}{r} \right\} \right] \\
& = 2\pi\delta_{mm'}(-1)^m \int_{-h}^h dz \int_0^\infty r dr \int_0^\infty dk \\
& \times \left[V_n(k, z) U_{n'}(k', z) \frac{imkk'}{4} \left\{ J_{m-1}(kr)J_{m-1}(k'r) - J_{m+1}(kr)J_{m+1}(k'r) \right\} \right] \\
& = 0
\end{aligned} \tag{2.2.19}$$

Note that, in the last line of the above equation, the definition of the Delta function in Eq. (2.2.14) was used. Therefore, now, we can conclude that the orthogonality relation in Eq. (2.2.17) applies to any cases.

The orthogonality derived here as Eq. (2.2.17) differs from the bi-orthogonality relation derived earlier [59], [60]. Equation (2.2.17) represents the orthogonality of the displacement eigenfunctions having different eigenfrequencies ω_n (belonging to different mode number in z) for a given (fixed) real-valued k . Referring to Fig. 2.2(a) that shows the dispersion relation for the SH wave modes, the corresponding eigenfrequencies are marked by circles in Fig. 2(a). On the other hand, the bi-orthogonality relation [59], [60] represents the orthogonality of a set of displacements and some stress components having different wave numbers k (real, imaginary or complex) for a given (fixed) frequency ω_{ext} . The corresponding wavenumbers are marked by circles in Fig. 2.2(b).

If $\mathbf{u}(\mathbf{r})$ is expressed in terms of $\varphi_n^m(k, \mathbf{r})$ as (see Eq. (2.2.4)),

$$\mathbf{u}(\mathbf{r}) = \frac{1}{2\pi} \int_0^\infty k dk \sum_{n,m} A_n^m(k) \varphi_n^m(k, \mathbf{r}), \tag{2.2.20}$$

the orthogonality derived as Eq. (2.2.17) can be used to obtain the expansion coefficient $A_n^m(k)$ as

$$A_n^m(k) = \frac{(-1)^m}{E_n(k)} \int_V dv \rho \varphi_n^{-m}(k, \mathbf{r}) \cdot \mathbf{u}(\mathbf{r}). \tag{2.2.21}$$

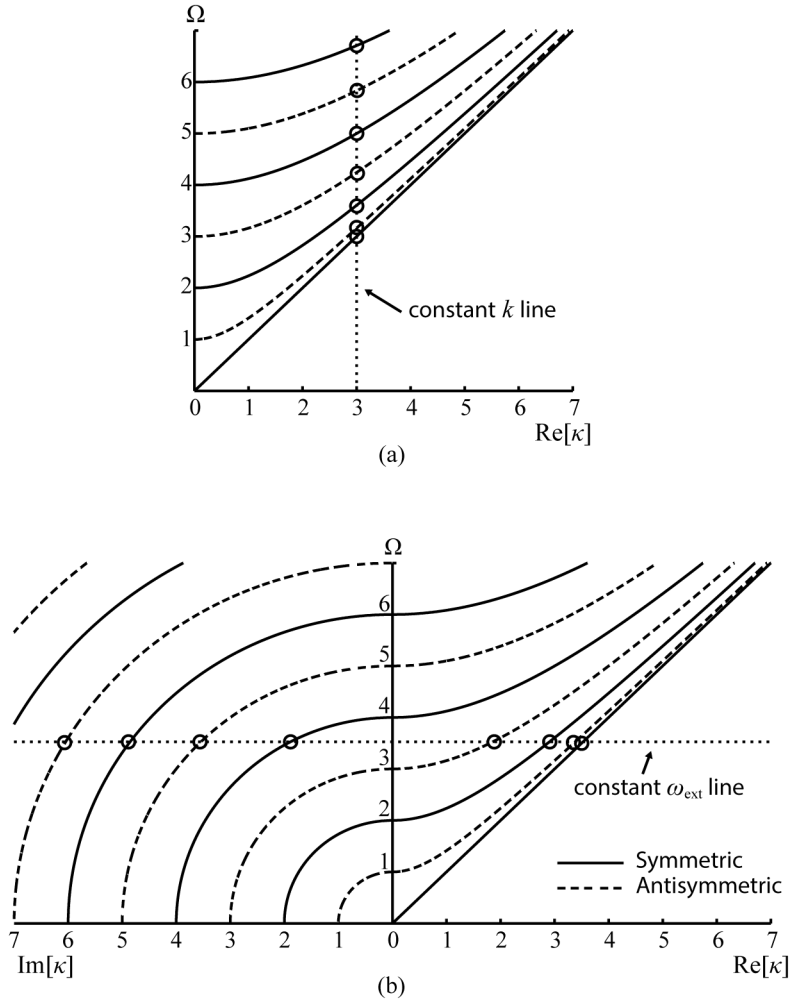


Figure 2.2 The dispersion curve for the shear horizontal wave modes with (bi-)orthogonal modes marked by circles. (a) The orthogonality relation derived in the present theory along the constant real k line, (b) the bi-orthogonality relation from the previous research [59] along the constant ω_{ext} line. Symbols: $\kappa = dk/\pi$ (dimensionless wavenumber), $\Omega = d\omega/\pi c_l$ (dimensionless frequency), $c_l = 6198$ m/s (longitudinal wave speed), $c_t = 3130$ m/s (shear wave speed).

The result given by Eqs. (2.2.20) and (2.2.21) will play a key role in representing the Green's functions in terms of the eigenfunction $\varphi_n^m(k, \mathbf{r})$. Note that Eqs. (2.2.20) and (2.2.21) are also valid when material properties of a plate vary in z .

2.2.1.2 Eigenfunction expansion of the Green's function

To find the Green's function $\mathbf{G}(\mathbf{r}|\mathbf{r}')$ in Eq. (2.2.3), we first need to expand the source term $\mathbf{I}\delta(\mathbf{r} - \mathbf{r}')$ in the right-hand side of Eq. (2.2.3) in terms of the eigenfunctions $\varphi_n^m(k, \mathbf{r})$. To this end, Eq. (2.2.21) is substituted into Eq. (2.2.4):

$$\mathbf{u}(\mathbf{r}) = \frac{1}{2\pi} \int_0^\infty k dk \int_V dv' \rho' \sum_{n,m} \frac{(-1)^m}{E_n(k)} \varphi_n^m(k, \mathbf{r}) \varphi_n^{-m}(k, \mathbf{r}') \cdot \mathbf{u}(\mathbf{r}'), \quad (2.2.22)$$

where $\varphi_n^m \varphi_n^{-m}$ implies the dyadic product of φ_n^m and φ_n^{-m} . By using the following property of the Dirac delta function $\mathbf{I}\delta(\mathbf{r} - \mathbf{r}')$,

$$\mathbf{u}(\mathbf{r}) = \int_V dv' \mathbf{I}\delta(\mathbf{r} - \mathbf{r}') \cdot \mathbf{u}(\mathbf{r}'), \quad (2.2.23)$$

and comparing Eq. (2.2.22) and Eq. (2.2.23), one can identify $\mathbf{I}\delta(\mathbf{r} - \mathbf{r}')$ as

$$\mathbf{I}\delta(\mathbf{r} - \mathbf{r}') = \frac{1}{2\pi} \int_0^\infty k dk \rho \sum_{n,m} \frac{(-1)^m}{E_n(k)} \varphi_n^m(k, \mathbf{r}) \varphi_n^{-m}(k, \mathbf{r}'), \quad (2.2.24)$$

where ρ' in Eq. (2.2.22) is replaced by ρ since $\delta(\mathbf{r} - \mathbf{r}')$ is non-zero only when $\mathbf{r} = \mathbf{r}'$.

Because the source-term $\mathbf{I}\delta(\mathbf{r} - \mathbf{r}')$ is expanded in terms of the eigenfunctions $\varphi_n^m(k, \mathbf{r})$ as Eq. (2.2.24), it will be convenient to write the Green's function $\mathbf{G}(\mathbf{r}|\mathbf{r}')$ as

$$\mathbf{G}(\mathbf{r}|\mathbf{r}') = \frac{1}{2\pi} \int_0^\infty k dk \sum_{n,m} a_n^m(k) \frac{(-1)^m}{E_n(k)} \varphi_n^m(k, \mathbf{r}) \varphi_n^{-m}(k, \mathbf{r}'), \quad (2.2.25)$$

where $a_n^m(k)$ are unknown scalar expansion coefficients to be determined. The substitution of Eqs. (2.2.24) and (2.2.25) into Eq. (2.2.3) and the use of Eq. (2.2.5) yield

$$a_n^m(k) = \frac{1}{\omega_n^2(k) - \omega_{\text{ext}}^2}.$$

Therefore, $\mathbf{G}(\mathbf{r}|\mathbf{r}')$ is now explicitly given as

$$\mathbf{G}(\mathbf{r}|\mathbf{r}') = \frac{1}{2\pi} \int_0^\infty kdk \sum_{n,m} \frac{(-1)^m}{[\omega_n^2(k) - \omega_{\text{ext}}^2]E_n(k)} \phi_n^m(k, \mathbf{r}) \phi_n^{-m}(k, \mathbf{r}'). \quad (2.2.26)$$

The examination of the right-hand side of Eq. (2.2.26) shows (as found in the process of the derivation of the eigenfunction orthogonality) that the following type of definite integrals should be evaluated:

$$f(r, r') = \int_0^\infty kdk g(k) J_m(kr) J_m(kr'), \quad (2.2.27)$$

where $g(k)$ is an even function of k . Among others, it is noted that $g(k)$ involves $[\omega_n^2(k) - \omega_{\text{ext}}^2]^{-1}$, which becomes singular when $\omega_n(k) = \omega_{\text{ext}}$. Therefore, one can use the residue theorem by converting the integral over the real axis in Eq. (2.2.27) to a complex contour integral.

For evaluating integration, we use the method suggested by Sommerfeld [64] (see also Tai [58] and Baddour [65]) and rewrite $f(r, r')$ in Eq. (2.2.27) as, depending on the location of the field point r relative to the source point r' :

$$f(r, r') = \frac{1}{2} \begin{cases} \int_{-\infty}^\infty kdk g(k) H_m^{(1)}(kr) J_m(kr'), & r > r', \\ \int_{-\infty}^\infty kdk g(k) J_m(kr) H_m^{(1)}(kr'), & r < r'. \end{cases} \quad (2.2.28)$$

Then, Eq. (2.2.26) can be rewritten as

$$\mathbf{G}(\mathbf{r}|\mathbf{r}') = \frac{1}{4\pi} \sum_{n,m} \int_{-\infty}^\infty kdk \frac{(-1)^m}{[\omega_n^2(k) - \omega_{\text{ext}}^2]E_n(k)} \bar{\phi}_n^m(k, \mathbf{r}) \phi_n^{-m}(k, \mathbf{r}'), \quad r > r', \quad (2.2.29a)$$

$$\mathbf{G}(\mathbf{r}|\mathbf{r}') = \frac{1}{4\pi} \sum_{n,m} \int_{-\infty}^\infty kdk \frac{(-1)^m}{[\omega_n^2(k) - \omega_{\text{ext}}^2]E_n(k)} \phi_n^m(k, \mathbf{r}) \bar{\phi}_n^{-m}(k, \mathbf{r}'), \quad r < r', \quad (2.2.29b)$$

where the singular eigenfunctions $\bar{\phi}_n^m(k, \mathbf{r}')$ is obtained by replacing the Bessel function $J_m(kr)$ with the Hankel function of the first kind $H_m^{(1)}(kr)$. If the contribution of mode (m, n) to $\mathbf{G}(\mathbf{r}|\mathbf{r}')$ is denoted by $\mathbf{G}_n^m(\mathbf{r}|\mathbf{r}')$, Eqs. (2.2.29) can be simply written as

$$\mathbf{G}(\mathbf{r}|\mathbf{r}') = \sum_{n,m} \mathbf{G}_n^m(\mathbf{r}|\mathbf{r}'). \quad (2.2.30)$$

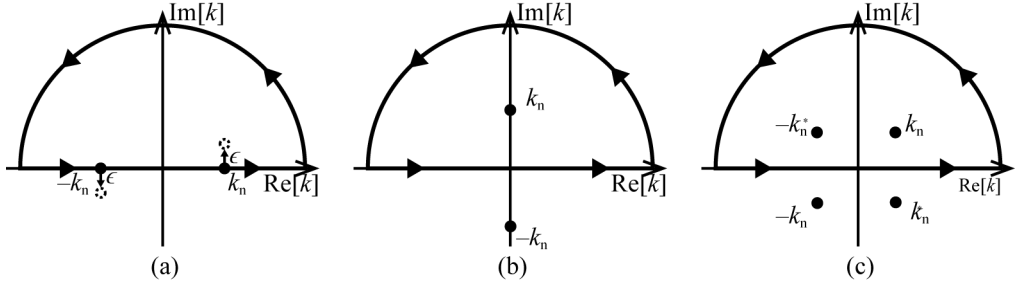


Figure 2.3 A contour enclosing (a) a pole on the real axis, (b) a pole on the imaginary axis and (c) a pair of complex-valued poles.

We will evaluate Eq. (2.2.29) by the residue theorem through the complex contour integral as illustrated in Fig. 2.3. Let us denote by k_n (real, imaginary, or complex) the pole satisfying the condition $\omega_n^2(k) - \omega_{\text{ext}}^2 = 0$ where ω_n is the frequency of the n^{th} branch in the dispersion (as shown in Fig. 2.2, for example). When the contour consisting of a semi-circle in the upper plane ($\text{Im}[k] > 0$) and the real axis shown in Fig. 2.3 is used, we only need to consider poles with $\text{Im}[k_n] > 0$. If a pole belongs to a propagating wave with $\text{Im}[k_n] = 0$, it is convenient to add an artificial infinitesimally-small non-zero value of ε such that $\varepsilon = \text{Im}[k_n] > 0$ during integration and put $\varepsilon = 0$ afterwards. [58] If this technique is used, the principal value integration (which of course yields the same result) may be avoided when a pole exists on the real axis. Note that if k_n is a solution to $\omega_n^2(k) - \omega_{\text{ext}}^2 = 0$, $-k_n$, k_n^* and $-k_n^*$ (*: complex conjugate) are also solutions. Therefore, two poles need to be included if k_n is complex as shown in Fig. 2.3(c).

Let us now perform the integration for \mathbf{G}_n^m for $r > r'$. If a pole is on the real or imaginary axis, the contour encloses a single pole as shown in Fig. 2.3(a) or in Fig.

2.3(b). In this case, $\mathbf{G}_n^m(\mathbf{r}|\mathbf{r}')$ (from Eq. (2.2.29a)) becomes

$$\begin{aligned}\mathbf{G}_n^m(\mathbf{r}|\mathbf{r}') &= \frac{1}{4\pi} \int_{-\infty}^{\infty} k dk \frac{(-1)^m}{[\omega_n^2(k) - \omega_{\text{ext}}^2]E_n(k)} \bar{\varphi}_n^m(k, \mathbf{r}) \varphi_n^{-m}(k, \mathbf{r}') \\ &= \frac{1}{4\pi} \left\{ \frac{2\pi i (-1)^m k}{\partial[\omega_n^2(k) - \omega_{\text{ext}}^2]/\partial k E_n(k)} \bar{\varphi}_n^m(k, \mathbf{r}) \varphi_n^{-m}(k, \mathbf{r}') \right\} \Big|_{k=k_n} \\ &= \frac{i(-1)^m k_n}{4\omega_{\text{ext}} c_{g,n}(k_n) E_n(k_n)} \bar{\varphi}_n^m(k_n, \mathbf{r}) \varphi_n^{-m}(k_n, \mathbf{r}').\end{aligned}\quad (2.2.31)$$

In the last expression of Eq. (2.2.31), the definition of the group velocity $c_{g,n}$ of the n^{th} mode is used:

$$c_{g,n}(k) = \frac{\partial \omega_n(k)}{\partial k}.\quad (2.2.32)$$

When poles are complex-valued, the residue contributions from two poles at k_n and $-k_n^*$ should be included. (Note that the corresponding waves are non-propagating.) In this case, $\mathbf{G}_n^m(\mathbf{r}|\mathbf{r}')$ becomes

$$\begin{aligned}\mathbf{G}_n^m(\mathbf{r}|\mathbf{r}') &= \frac{i(-1)^m k_n}{4\omega_{\text{ext}} c_{g,n}(k_n) E_n(k_n)} \bar{\varphi}_n^m(k_n, \mathbf{r}) \varphi_n^{-m}(k_n, \mathbf{r}') \\ &\quad + \frac{i(-1)^m (-k_n^*)}{4\omega_{\text{ext}} c_{g,n}(-k_n^*) E_n(-k_n^*)} \bar{\varphi}_n^m(-k_n^*, \mathbf{r}) \varphi_n^{-m}(-k_n^*, \mathbf{r}').\end{aligned}\quad (2.2.33)$$

Results similar to Eq. (2.2.31) and Eq. (2.2.33) can be obtained for $r < r'$. If these results and those obtained in Eqs. (2.2.31) and (2.2.33) are substituted into Eq. (2.2.30), the Green's function is finally expressed as

$$\mathbf{G}(\mathbf{r}|\mathbf{r}') = \sum_{n,m} \frac{(-1)^m i k_n}{4P_n} \bar{\varphi}_n^m(\mathbf{r}) \varphi_n^{-m}(\mathbf{r}'), r > r',\quad (2.2.34a)$$

$$\mathbf{G}(\mathbf{r}|\mathbf{r}') = \sum_{n,m} \frac{(-1)^m i k_n}{4P_n} \varphi_n^m(\mathbf{r}) \bar{\varphi}_n^{-m}(\mathbf{r}'), r < r'.\quad (2.2.34b)$$

where

$$P_n = \omega_{\text{ext}} c_{g,n}(k_n) E_n(k_n).\quad (2.2.35)$$

and we have used the notation $\varphi_n^m(\mathbf{r}) = \varphi_n^m(k_n, \mathbf{r})$. Note that in case of complex valued k_n 's, the summation of $\mathbf{G}_n^m(\mathbf{r}|\mathbf{r}')$ must be understood as the expression shown in Eq. (2.2.33) in order for the contributions both from k_n and $-k_n^*$ to be included.

2.2.1.3 Properties of the Green's function

The derived Green's function in Eq. (2.2.34) satisfies some fundamental properties of linear elasticity. Therefore, in this section, we will derive two properties of the Green's function. One of them will be of the well known form that is commonly observed in the Green's function for bulk waves. However, we will also newly derive another property exclusively valid for guided waves.

Let us first consider two point sources located at \mathbf{r}_1 and \mathbf{r}_2 :

$$\mathbf{f}_1(\mathbf{r}) = \mathbf{I}\delta(\mathbf{r} - \mathbf{r}_1) \cdot \mathbf{f}_1, \quad \mathbf{f}_2(\mathbf{r}) = \mathbf{I}\delta(\mathbf{r} - \mathbf{r}_2) \cdot \mathbf{f}_2, \quad (2.2.36)$$

Then, the fields $\mathbf{u} = \mathbf{u}(\mathbf{r})$ and $\mathbf{v}(\mathbf{r})$ generated by these point sources are given by the definition of the Green's function as follows

$$\begin{aligned} \mathbf{u}(\mathbf{r}) &= \mathbf{G}(\mathbf{r}|\mathbf{r}_1) \cdot \mathbf{f}_1, \\ \mathbf{v}(\mathbf{r}) &= \mathbf{G}(\mathbf{r}|\mathbf{r}_2) \cdot \mathbf{f}_2. \end{aligned} \quad (2.2.37)$$

To derive a property of the Green's function, we manipulate \mathbf{u} and \mathbf{v} similarly as in derivation of Eq. (2.2.9):

$$[\mathbf{u}, \mathbf{v}]_S = \int_V dV [\mathbf{u} \cdot \mathbf{f}_1(\mathbf{r}) - \mathbf{v} \cdot \mathbf{f}_2(\mathbf{r})]. \quad (2.2.38)$$

where we have used the compact notation for the surface integral:

$$[\mathbf{u}, \mathbf{v}]_S \triangleq \int_S dS \{ \mathbf{u} \cdot [\mathbf{n} \cdot \boldsymbol{\sigma}(\mathbf{v})] - \mathbf{v} \cdot [\mathbf{n} \cdot \boldsymbol{\sigma}(\mathbf{u})] \}. \quad (2.2.39)$$

Now, we assume that the volume V in the above equation is an annular cylinder which encloses \mathbf{f}_1 and \mathbf{f}_2 with its inner surface located at the radius $r = a$ and the outer surface at $r = b$. Then, by using the Green's function for $r < r'$ in Eq. (2.2.34b), it can be shown that the fields \mathbf{u} and \mathbf{v} on the inner surface at $r = a$ are described in terms of the regular basis functions $\varphi_n^m(\mathbf{r})$. In this case, the surface integral at $r = a$ is vanished as a result

of the orthogonality relations between the basis functions which will be derived in Section 3.3.1.1:

$$[\varphi_n^m, \varphi_v^\mu]_{r=a} = 0. \quad (2.2.40)$$

In the same manner, we can show that the surface integral at $r = b$ is described in terms of the singular basis functions $\bar{\varphi}_n^m(\mathbf{r})$ and that this surface integral also vanishes because of the following orthogonality relation:

$$[\bar{\varphi}_n^m, \bar{\varphi}_v^\mu]_{r=b} = 0. \quad (2.2.41)$$

Therefore, Eq. (2.2.38) becomes

$$\int_V dv [\mathbf{u} \cdot \mathbf{f}_1(\mathbf{r}) - \mathbf{v} \cdot \mathbf{f}_2(\mathbf{r})] = 0. \quad (2.2.42)$$

Substituting Eqs. (2.2.36) and (2.2.37) into Eq. (2.2.42) and some manipulation yield

$$\begin{aligned} 0 &= \mathbf{G}(\mathbf{r}_2|\mathbf{r}_1) \cdot \mathbf{f}_1 \cdot \mathbf{f}_2 - \mathbf{G}(\mathbf{r}_1|\mathbf{r}_2) \cdot \mathbf{f}_2 \cdot \mathbf{f}_1 \\ &= \mathbf{f}_2 \cdot \mathbf{G}(\mathbf{r}_2|\mathbf{r}_1) \cdot \mathbf{f}_1 - \mathbf{f}_2 \cdot [\mathbf{G}(\mathbf{r}_1|\mathbf{r}_2)]^T \cdot \mathbf{f}_1. \end{aligned} \quad (2.2.43)$$

where $[\mathbf{G}(\mathbf{r}_1|\mathbf{r}_2)]^T$ denotes the transpose of $\mathbf{G}(\mathbf{r}_1|\mathbf{r}_2)$.

In the above equation, we have used $\mathbf{f}_1 \cdot \mathbf{G}(\mathbf{r}_1|\mathbf{r}_2) \cdot \mathbf{f}_2 = \mathbf{f}_2 \cdot [\mathbf{G}(\mathbf{r}_1|\mathbf{r}_2)]^T \cdot \mathbf{f}_1$. Since Eq. (2.2.43) is valid for any \mathbf{f}_1 and \mathbf{f}_2 , this equation can be rewritten as

$$\mathbf{G}(\mathbf{r}_2|\mathbf{r}_1) = [\mathbf{G}(\mathbf{r}_1|\mathbf{r}_2)]^T. \quad (2.2.44)$$

This is the first property known as the reciprocity relation of the Green's function. However, it should also be noted that, unlike the Green's function for an unbounded medium, the Green's function $\mathbf{G}(\mathbf{r}|\mathbf{r}')$ in Eq. (2.2.34) is not a symmetric tensor. This means that

$$\mathbf{G}(\mathbf{r}_2|\mathbf{r}_1) \neq [\mathbf{G}(\mathbf{r}_2|\mathbf{r}_1)]^T. \quad (2.2.45)$$

Another property can be derived by taking the complex conjugate of the field \mathbf{v} in Eq. (2.2.38), then we have

$$[\mathbf{u}, \mathbf{v}^*]_S = \int_V dv (\mathbf{u} \cdot \mathbf{f}_2^* - \mathbf{v}^* \cdot \mathbf{f}_1). \quad (2.2.46)$$

In this case, the problem is more complicated because the LHS of the above equation does not vanish. To explain this, we need the following two properties of the basis functions that will be derived in Section 3.3.1.2:

$$[\varphi_n^m, (\varphi_v^\mu)^*]_{r=a} = 0, \quad [\bar{\varphi}_n^m, (\bar{\varphi}_v^\mu)^*]_{r=b} = \tau_n 8i/k_n P_n \delta_{m\mu} \delta_{nv}, \quad (2.2.47)$$

where $\tau_n = 1$ for propagating modes and $\tau_n = 0$ for non-propagating modes.

Now, we can evaluate the LHS of Eq. (2.2.46). The integral over the inner surface at $r = a$ vanishes because of the first relation in Eq. (2.2.47) vanishes. However, the integral over the outer surface at $r = b$ does not vanish and we can show, by using Eq. (2.2.37), the explicit expression of the Green's function in Eq. (2.2.34a), and the second relation in Eq. (2.2.47), that it becomes

$$[\mathbf{u}, \mathbf{v}^*]_{r=b} = 2 \sum_{m,n} \tau_n \frac{ik_n}{4P_n} \mathbf{f}_2^* \cdot \varphi_n^m(\mathbf{r}_2) \varphi_n^{-m}(\mathbf{r}_1) \cdot \mathbf{f}_1, \quad (2.2.48)$$

where we have used $(\varphi_n^{-m}(\mathbf{r}_2))^* = \varphi_n^m(\mathbf{r}_2)$. On the other hand, we can easily show as before in deriving Eq. (2.2.43) that the RHS of Eq. (2.2.46) is

$$\int_V dv (\mathbf{u} \cdot \mathbf{f}_2^* - \mathbf{v}^* \cdot \mathbf{f}_1) = \mathbf{f}_2^* \cdot \mathbf{G}(\mathbf{r}_2|\mathbf{r}_1) \cdot \mathbf{f}_1 - \mathbf{f}_2^* \cdot [\mathbf{G}(\mathbf{r}_1|\mathbf{r}_2)]^H \cdot \mathbf{f}_1. \quad (2.2.49)$$

where $[\mathbf{G}(\mathbf{r}_1|\mathbf{r}_2)]^H$ denotes the conjugate transpose of $\mathbf{G}(\mathbf{r}_1|\mathbf{r}_2)$. Therefore, we finally have the second property of the Green's function as follows

$$\mathbf{G}(\mathbf{r}_2|\mathbf{r}_1) - [\mathbf{G}(\mathbf{r}_1|\mathbf{r}_2)]^H = 2 \sum_{m,n} \tau_n \frac{ik_n}{4P_n} \varphi_n^m(\mathbf{r}_2) \varphi_n^{-m}(\mathbf{r}_1). \quad (2.2.50)$$

Validity of the above property can be checked by using the relations between two nonorthogonal modes that will be discussed in Section 3.3.1.2.

2.2.2 Green's function in Cartesian coordinate system

This section is devoted to the derivation of the same Green's function, but we start from the Cartesian coordinate. Overall procedure is similar to that in the cylindrical coordinate system. The Green's function we first obtain is in the form of superposition of plane waves in all possible directions and later this will be converted to the multipole expansion form.

2.2.2.1 Orthogonality of eigenfunctions for a fixed wave number k

As we have shown in Section 2.2.1, the displacement can be expressed in the cylindrical coordinate system by using an inverse integral transform based on the Hankel transform and the Fourier series. Similarly, in the Cartesian coordinate, the double Fourier transform is employed for motion along the horizontal plane of the plate instead of the Hankel transform and the Fourier series. Then, the displacement field $\mathbf{u}(\mathbf{r})$ can be written as the following inverse Fourier transform :

$$\mathbf{u}(\mathbf{r}) = \frac{1}{(2\pi)^2} \int_{-\infty}^{\infty} dk_x \int_{-\infty}^{\infty} dk_y \sum_n A_n(\mathbf{k}) \varphi_n(\mathbf{k}, \mathbf{r}) \quad (2.2.51)$$

where $A_n(\mathbf{k})$ are unknown expansion coefficients to be determined. The kernel $\varphi_n(\mathbf{k}, \mathbf{r})$ of the above integral transform is the eigenfunctions of the following eigenvalue equation,

$$\nabla \cdot \sigma(\varphi_n(\mathbf{k}, \mathbf{r})) + \rho \omega_n^2 \varphi_n(\mathbf{k}, \mathbf{r}) = \mathbf{0}. \quad (2.2.52)$$

and satisfies the boundary conditions in Eq. (2.2.2b). Because wave propagation in the horizontal plane (x - y plane) will be mainly considered, the wavenumber \mathbf{k} will be set to be $\mathbf{k} = (k_x, k_y, 0)$ and its magnitude is denoted by $k = \sqrt{k_x^2 + k_y^2}$. The explicit forms of the eigenfunctions are given by

· Lamb type wave mode:

$$\boldsymbol{\varphi}_n^m(\mathbf{k}, \mathbf{r}) = \begin{Bmatrix} i(k_x/k)U_n(k, z) \\ i(k_y/k)U_n(k, z) \\ W_n(k, z) \end{Bmatrix} e^{i\mathbf{k}\cdot\mathbf{r}}, \quad (2.2.53)$$

· Shear-horizontal (SH) wave mode:

$$\boldsymbol{\varphi}_n^m(\mathbf{k}, \mathbf{r}) = \begin{Bmatrix} i(k_y/k)V_n(k, z) \\ -i(k_x/k)V_n(k, z) \\ 0 \end{Bmatrix} e^{i\mathbf{k}\cdot\mathbf{r}}. \quad (2.2.54)$$

To expand $\mathbf{G}(\mathbf{r}|\mathbf{r}')$ in terms of the eigenfunction $\boldsymbol{\varphi}_n(\mathbf{k}, \mathbf{r})$, the orthogonality relation of the eigenfunctions should be first defined. To derive the orthogonality relation, consider the following two equations resulting from equation Eq.(2.2.52)

$$\nabla \cdot \boldsymbol{\sigma}_n + \rho \omega_n^2(\mathbf{k}) \boldsymbol{\varphi}_n = 0, \quad (2.2.55a)$$

$$\nabla \cdot \boldsymbol{\sigma}_{n'} + \rho \omega_{n'}^2(-\mathbf{k}') \boldsymbol{\varphi}_{n'} = 0. \quad (2.2.55b)$$

In the above equations, the compact notations as shown in Eq. (2.2.5b) of Section 2.2.1 are similarly employed. In Eq.(2.2.55b), the terms with the subscript n' are associated with $-\mathbf{k}'$, which results from the complex conjugate of terms with \mathbf{k}' . The dot-product of Eq.(2.2.55b) with $\boldsymbol{\varphi}_n$ can be subtracted from the dot-product of Eq.(2.2.55a) with $\boldsymbol{\varphi}_{n'}$ to yield (after some manipulations)

$$\nabla \cdot (\boldsymbol{\sigma}_n \cdot \boldsymbol{\varphi}_{n'} - \boldsymbol{\sigma}_{n'} \cdot \boldsymbol{\varphi}_n) = \rho (\omega_{n'}^2(-\mathbf{k}') - \omega_n^2(\mathbf{k})) \boldsymbol{\varphi}_n \cdot \boldsymbol{\varphi}_{n'}. \quad (2.2.56)$$

Using the definition of the divergence operator, the above equation can be rewritten as

$$\begin{aligned} & \frac{\partial}{\partial x} (\boldsymbol{\sigma}_n \cdot \boldsymbol{\varphi}_{n'} - \boldsymbol{\sigma}_{n'} \cdot \boldsymbol{\varphi}_n) \cdot \hat{\mathbf{e}}_x + \frac{\partial}{\partial y} (\boldsymbol{\sigma}_n \cdot \boldsymbol{\varphi}_{n'} - \boldsymbol{\sigma}_{n'} \cdot \boldsymbol{\varphi}_n) \cdot \hat{\mathbf{e}}_y \\ & + \frac{\partial}{\partial z} (\boldsymbol{\sigma}_n \cdot \boldsymbol{\varphi}_{n'} - \boldsymbol{\sigma}_{n'} \cdot \boldsymbol{\varphi}_n) \cdot \hat{\mathbf{e}}_z = \rho (\omega_{n'}^2(-\mathbf{k}') - \omega_n^2(\mathbf{k})) \boldsymbol{\varphi}_n \cdot \boldsymbol{\varphi}_{n'}. \end{aligned} \quad (2.2.57)$$

Now, by separating $e^{i\mathbf{k}\cdot\mathbf{r}}$ in φ_n , the following notations are defined,

$$\begin{aligned}
\varphi_n &= \tilde{\varphi}_n(\mathbf{k}, z) e^{i\mathbf{k}\cdot\mathbf{r}} \\
\varphi_{n'} &= \tilde{\varphi}_{n'}(-\mathbf{k}', z) e^{-i\mathbf{k}'\cdot\mathbf{r}} \\
\sigma_n &= \sigma(\tilde{\varphi}_n(\mathbf{k}, z)) e^{i\mathbf{k}\cdot\mathbf{r}} \\
\sigma_{n'} &= \sigma(\tilde{\varphi}_{n'}(-\mathbf{k}', z)) e^{-i\mathbf{k}'\cdot\mathbf{r}}.
\end{aligned} \tag{2.2.58}$$

Note that $\mathbf{k}\cdot\mathbf{r} = k_x x + k_y y$. Substituting these into the first term on the RHS of Eq. (2.2.57) results in,

$$\begin{aligned}
&\frac{\partial}{\partial x} (\sigma_n \cdot \varphi_{n'} - \sigma_{n'} \cdot \varphi_n) \cdot \hat{\mathbf{e}}_x \\
&= \left[\frac{\partial}{\partial x} (\sigma_n) \cdot \varphi_{n'} + \sigma_n \cdot \frac{\partial}{\partial x} (\varphi_{n'}) - \frac{\partial}{\partial x} (\sigma_{n'}) \cdot \varphi_n - \sigma_{n'} \cdot \frac{\partial}{\partial x} (\varphi_n) \right] \cdot \hat{\mathbf{e}}_x \\
&= i(k_x - k'_x) [\tilde{\sigma}_n \cdot \tilde{\varphi}_{n'} - \tilde{\sigma}_{n'} \cdot \tilde{\varphi}_n] e^{i(\mathbf{k}-\mathbf{k}')\cdot\mathbf{r}} \cdot \hat{\mathbf{e}}_x.
\end{aligned} \tag{2.2.59}$$

The second term on the RHS of Eq. (2.2.57) can be similarly rewritten. Then, substituting Eq. (2.2.59) into Eq. (2.2.57), integrating this equation over V ($0 \leq x < \infty$, $0 \leq y < \infty$, $0 \leq z \leq d$) and use of the definition of the Dirac delta function,

$$\delta(\mathbf{k} - \mathbf{k}') = \frac{1}{(2\pi)^2} \int_{-\infty}^{\infty} dx \int_{-\infty}^{\infty} dy e^{i(\mathbf{k}-\mathbf{k}')\cdot\mathbf{r}}, \tag{2.2.60}$$

results in the following equation:

$$\begin{aligned}
&(2\pi)^2 \delta(\mathbf{k} - \mathbf{k}') \left\{ \int_0^d dz [\tilde{\sigma}_n \cdot \tilde{\varphi}_{n'} - \tilde{\sigma}_{n'} \cdot \tilde{\varphi}_n] \cdot [i(k_x - k'_x) \hat{\mathbf{e}}_x + i(k_y - k'_y) \hat{\mathbf{e}}_y] \right. \\
&\quad \left. + \int_0^d dz \frac{\partial}{\partial z} [\tilde{\sigma}_n \cdot \tilde{\varphi}_{n'} - \tilde{\sigma}_{n'} \cdot \tilde{\varphi}_n] \cdot \hat{\mathbf{e}}_z \right\} \\
&= (2\pi)^2 \delta(\mathbf{k} - \mathbf{k}') \rho [\omega_{n'}^2(-\mathbf{k}') - \omega_n^2(\mathbf{k})] \int_0^d dz \rho [\tilde{\varphi}_n(\mathbf{k}, z) \cdot \tilde{\varphi}_{n'}(-\mathbf{k}', z)].
\end{aligned} \tag{2.2.61}$$

Then, it is easily found that the first term on the RHS of Eq. (2.2.61) always vanishes for any combination of \mathbf{k} and \mathbf{k}' , and the second term on the RHS of Eq. (2.2.61) also vanishes because of the traction free boundary conditions on the top and the bottom

surfaces of the plate,

$$\int_0^d dz \frac{\partial}{\partial z} [\tilde{\sigma}_n \cdot \tilde{\varphi}_{n'} - \tilde{\sigma}_{n'} \cdot \tilde{\varphi}_n] \cdot \hat{\mathbf{e}}_z = [(\tilde{\sigma}_n \cdot \tilde{\varphi}_{n'} - \tilde{\sigma}_{n'} \cdot \tilde{\varphi}_n) \cdot \hat{\mathbf{e}}_z]_{z=0}^{z=d} = 0. \quad (2.2.62)$$

For further analysis, it is better to simplify Eq. (2.2.61) by integrating over the \mathbf{k}' space ($\int_{-\infty}^{\infty} dk'_x \int_{-\infty}^{\infty} dk'_y (\dots)$). Then, we have the following relation:

$$\rho [\omega_{n'}^2(-\mathbf{k}) - \omega_n^2(\mathbf{k})] \int_0^d dz \rho [\tilde{\varphi}_n(\mathbf{k}, z) \cdot \tilde{\varphi}_{n'}(-\mathbf{k}, z)] = 0. \quad (2.2.63)$$

Equation (2.2.63) states that $\omega_{n'}^2(-\mathbf{k}) \neq \omega_n^2(\mathbf{k})$, i.e., if $n \neq n'$ for a given \mathbf{k} , the integral over z must vanish as we explained for the case in the cylindrical coordinate in Section 2.2.1. Therefore, for two eigenfunctions the following orthogonality relation holds:

$$\int_V dv \rho \varphi_n^m(\mathbf{k}, \mathbf{r}) \cdot \varphi_{n'}^m(-\mathbf{k}', \mathbf{r}) = (2\pi)^2 \delta(\mathbf{k} - \mathbf{k}') \delta_{nn'} E_n. \quad (2.2.64)$$

E_n in the above equation is defined in Eqs. (2.2.18a) and (2.2.18b). Having obtained the orthogonality relation for eigenfunctions, now we can define integral transform pairs for a field $\mathbf{u}(\mathbf{r})$,

$$\mathbf{u}(\mathbf{r}) = \frac{1}{(2\pi)^2} \int_{-\infty}^{\infty} dk_x \int_{-\infty}^{\infty} dk_y \sum_n A_n(\mathbf{k}) \varphi_n(\mathbf{k}, \mathbf{r}), \quad (2.2.65a)$$

$$A_n(\mathbf{k}) = \frac{1}{E_n} \int_V dv \rho \varphi_n(-\mathbf{k}, \mathbf{r}) \cdot \mathbf{u}(\mathbf{r}). \quad (2.2.65b)$$

Eq.(2.2.65b) can be obtained by taking the dot product of Eq. (2.2.65a) with $\varphi_{n'}(-\mathbf{k}', \mathbf{r})$, integrating it over V with the use of Eq. (2.2.64).

2.2.2.2 Eigenfunction expansion of the Green's function

For derivation of the Green's function $\mathbf{G}(\mathbf{r}|\mathbf{r}')$ in Eq.(2.2.3), the source term $\mathbf{I}\delta(\mathbf{r} - \mathbf{r}')$ appearing in the right-hand side of Eq.(2.2.3) should be expanded in terms of the eigenfunctions $\varphi_n(\mathbf{k}, \mathbf{r})$. In this reason, we first substitute Eq. (2.2.65b) into Eq. (2.2.65a):

$$\mathbf{u}(\mathbf{r}) = \frac{1}{(2\pi)^2} \int_{-\infty}^{\infty} dk_x \int_{-\infty}^{\infty} dk_y \int_V dv' \rho' \sum_n \frac{1}{E_n} \varphi_n(\mathbf{k}, \mathbf{r}) \varphi_n(-\mathbf{k}, \mathbf{r}') \cdot \mathbf{u}(\mathbf{r}'). \quad (2.2.66)$$

By using the definition of the Dirac delta function, $\mathbf{I}\delta(\mathbf{r} - \mathbf{r}')$ is expressed as

$$\mathbf{I}\delta(\mathbf{r} - \mathbf{r}') = \frac{1}{(2\pi)^2} \int_{-\infty}^{\infty} dk_x \int_{-\infty}^{\infty} dk_y \rho \sum_n \frac{1}{E_n} \varphi_n(\mathbf{k}, \mathbf{r}) \varphi_n(-\mathbf{k}, \mathbf{r}'). \quad (2.2.67)$$

In the above equation, ρ is used instead of ρ' because $\delta(\mathbf{r} - \mathbf{r}')$ is non-zero only when $\mathbf{r}' = \mathbf{r}$.

Because the source-term $\mathbf{I}\delta(\mathbf{r} - \mathbf{r}')$ is expanded in terms of eigenfunctions φ_n as Eq.(2.2.67), one can also assume that the Green's function $\mathbf{G}(\mathbf{r}|\mathbf{r}')$ can be expanded in terms of φ_n as follows:

$$\mathbf{G}(\mathbf{r}|\mathbf{r}') = \frac{1}{(2\pi)^2} \int_{-\infty}^{\infty} dk_x \int_{-\infty}^{\infty} dk_y \sum_n \frac{a_n(\mathbf{k})}{E_n} \varphi_n(\mathbf{k}, \mathbf{r}) \varphi_n(-\mathbf{k}, \mathbf{r}'), \quad (2.2.68)$$

where $a_n(\mathbf{k})$ are unknown scalar expansion coefficients to be determined. Substituting Eqs.(2.2.67) and (2.2.68) into Eq.(2.2.3) with the use of Eq.(2.2.52) yields

$$a_n(\mathbf{k}) = \frac{1}{(\omega_n^2(\mathbf{k}) - \omega_{\text{ext}}^2)}. \quad (2.2.69)$$

Finally, by substituting Eq. (2.2.69) into Eq. (2.2.68), we have the Green's function $\mathbf{G}(\mathbf{r}|\mathbf{r}')$ as follows:

$$\mathbf{G}(\mathbf{r}|\mathbf{r}') = \frac{1}{(2\pi)^2} \int_{-\infty}^{\infty} dk_x \int_{-\infty}^{\infty} dk_y \sum_n \frac{1}{(\omega_n^2(\mathbf{k}) - \omega_{\text{ext}}^2)E_n} \varphi_n(\mathbf{k}, \mathbf{r}) \varphi_n(-\mathbf{k}, \mathbf{r}'). \quad (2.2.70)$$

Here, we have two choices for calculation of Eq. (2.2.70). One way is to integrate directly over the two-dimensional infinite \mathbf{k} space. The other choice is to take the integral over an infinite interval analytically for one of k_x and k_y and then, the remaining integral is computed numerically.

Because the latter is easier in many cases, here we perform the integration with respect to k_x for example. The analytic integration can be carried out by the residue theorem in which closing contour of a semicircle can be located in the upper or lower-half complex plane. For $x > x'$, the residue theorem is applied by using the contour closing the upper-half complex plane counter-clockwisely. Here, we define the

pole $\mathbf{k}_n = (k_{x,n}, k_y, 0)$ satisfying $\omega_{\text{ext}} = \omega_n(\mathbf{k})$ for given k_y . Then, the integration in Eq.(2.2.70) over k_x becomes

$$\begin{aligned} & \int_{-\infty}^{\infty} dk_x \frac{1}{(\omega_n^2(\mathbf{k}) - \omega_{\text{ext}}^2) E_n} \varphi_n(\mathbf{k}, \mathbf{r}) \varphi_n(-\mathbf{k}, \mathbf{r}') \\ &= \frac{2\pi i}{\partial / \partial k_x [\omega_n^2(\mathbf{k}) - \omega_{\text{ext}}^2] |_{k_x=k_{x,n}} E_n} \varphi_n(\mathbf{k}_n, \mathbf{r}) \varphi_n(-\mathbf{k}_n, \mathbf{r}') \\ &= \frac{\pi i}{\omega_{\text{ext}} c_{g,n} E_n k_{x,n} / k_n} \varphi_n(\mathbf{k}_n, \mathbf{r}) \varphi_n(-\mathbf{k}_n, \mathbf{r}'), \end{aligned} \quad (2.2.71)$$

In the above equation, the following definition was used:

$$\left. \frac{\partial \omega_n}{\partial k_x} \right|_{k_x=k_{x,n}} = \left[\frac{d\omega_n}{dk} \frac{\partial k}{\partial k_x} \right]_{k_x=k_{x,n}} \triangleq c_{g,n} \frac{k_{x,n}}{k_n} \quad (2.2.72)$$

Since details related to the complex contour integral are similar to the case of the cylindrical coordinate, details are omitted here (see, Section 2.2.1).

$$\mathbf{G}(\mathbf{r}|\mathbf{r}') = \int_{-\infty}^{\infty} dk_y \sum_n \frac{ik_n}{4\pi P_n k_{x,n}} \varphi_n(\mathbf{k}_n, \mathbf{r}) \varphi_n(-\mathbf{k}_n, \mathbf{r}'), \quad x > x'. \quad (2.2.73a)$$

where

$$P_n = \omega_{\text{ext}} c_{g,n} E_n.$$

For $x < x'$, we use a clockwise contour in the lower-half complex plane. Therefore, the Green's function valid for $x < x'$ is expressed as

$$\mathbf{G}(\mathbf{r}|\mathbf{r}') = \int_{-\infty}^{\infty} dk_y \sum_n \frac{ik_n}{4\pi P_n k_{x,n}} \varphi_n(\boldsymbol{\kappa}_n, \mathbf{r}) \varphi_n(-\boldsymbol{\kappa}_n, \mathbf{r}'), \quad x < x'. \quad (2.2.73b)$$

where $\boldsymbol{\kappa}_n = (-k_{x,n}, k_y, 0)$. Theoretically, Eqs. (2.2.73a) and (2.2.73b) are valid for generally complex vauled k . However, for a real-valued k , the equation diverges at $k_{x,n}$ and thus we need to apply a change of variables to avoid this problem. Then, for example, Eq. (2.2.73b) can be rewritten as follows,

$$\mathbf{G}(\mathbf{r}|\mathbf{r}') = \int_{\Gamma} d\phi \sum_n \frac{ik_n}{4\pi P_n} \varphi_n(\mathbf{k}_n, \mathbf{r}) \varphi_n(-\mathbf{k}_n, \mathbf{r}'), \quad x > x', \text{ for real } k_n, \quad (2.2.74)$$

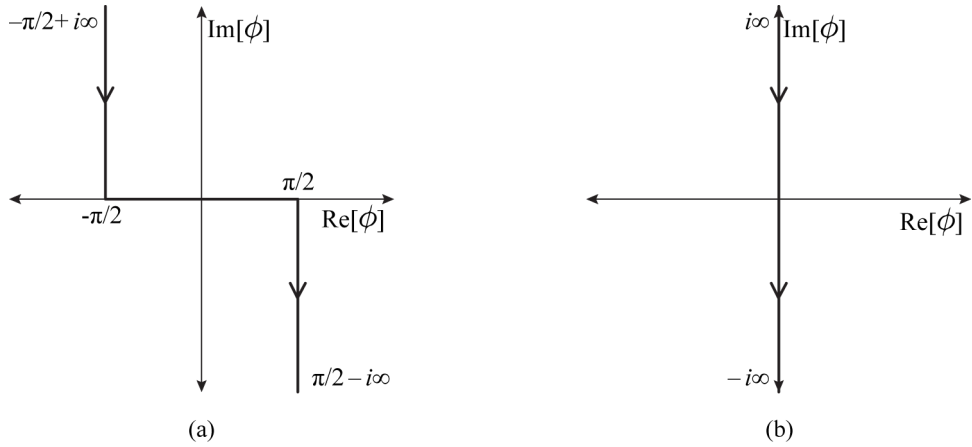


Figure 2.4 A path in the complex plane of ϕ over which the contour integration is performed when k_n is (a) real or complex, (b) imaginary.

where

$$\mathbf{k}_n = (k_{x,n}, k_{y,n}, 0), \quad k_{x,n} = k_n \cos \phi, \quad k_{y,n} = k_n \sin \phi. \quad (2.2.75)$$

There may be many possible choices for a path Γ for the contour integration. For example, for a real and complex k_n , Γ can be a path through $-\pi/2 + i\infty$, $-\pi/2$, $\pi/2$, $\pi/2 - i\infty$ as indicated in Fig. 2.2.74 (a) [66] and for a imaginary k_n , Γ can be a path through $i\infty$, $-i\infty$ as depicted in Fig. 2.2.74 (b).

2.3 Calculation of basis functions

Here, we will deal with more details about the basis functions. For brevity of explanation, the compact notion for the eigenfunctions $\varphi_n^m(\mathbf{r}) = \varphi_n^m(k_n, \mathbf{r})$ will be used in the subsequent sections. And from now on, we will redefine the notation for the angular frequency of an external force as $\omega = \omega_{\text{ext}}$.

For the use in scattering analyses in Chapter 3, we first provide the components of the displacement and stress basis functions in the cylindrical coordinate system.

Lamb type wave mode basis functions are in the form of

$$\varphi_n^m(\mathbf{r}) = \left\{ \begin{array}{c} U_n(z)J'_m(k_nr) \\ U_n(z)imJ_m(k_nr)/k_nr \\ W_n(z)J_m(k_nr) \end{array} \right\} e^{im\theta}. \quad (2.3.1)$$

And the corresponding stress basis functions are in the form of

$$\begin{aligned} \sigma_{n,rr}^m(\mathbf{r}) = & \left\{ 2\mu_L U_n(z) \frac{J_{m+1}(k_nr)}{r} - \left[2m(1-m)\mu_L U_n(z) \right. \right. \\ & \left. \left. + k_n^2(\lambda_L + 2\mu_L)U_n(z)r^2 - k_n\lambda_L r^2 \frac{dW_n(z)}{dz} \right] \frac{J_m(k_nr)}{k_nr^2} \right\} e^{im\theta}, \end{aligned} \quad (2.3.2a)$$

$$\begin{aligned} \sigma_{n,\theta\theta}^m(\mathbf{r}) = & \left\{ \lambda_L \left[\frac{dW_n(z)}{dz} - k_n U_n(z) \right] J_m(k_nr) \right. \\ & \left. - 2\mu_L U_n \left[\frac{J_{m+1}(k_nr)}{r} + m(m-1) \frac{J_m(k_nr)}{k_nr^2} \right] \right\} e^{im\theta}, \end{aligned} \quad (2.3.2b)$$

$$\sigma_{n,zz}^m(\mathbf{r}) = \left[(\lambda_L + 2\mu_L) \frac{dW_n(z)}{dz} - k_n \lambda_L U_n(z) \right] J_m(k_nr) e^{im\theta}, \quad (2.3.2c)$$

$$\sigma_{n,r\theta}^m(\mathbf{r}) = -2im\mu_L U_n(z) \left[(1-m) \frac{J_m(k_nr)}{k_nr^2} + \frac{J_{m+1}(k_nr)}{r} \right] e^{im\theta}, \quad (2.3.2d)$$

$$\sigma_{n,\theta z}^m(\mathbf{r}) = \left\{ im\mu_L \left[\frac{dU_n(z)}{dz} + k_n W_n(z) \right] \frac{J_m(k_nr)}{k_nr} \right\} e^{im\theta}, \quad (2.3.2e)$$

$$\sigma_{n,rz}^m(\mathbf{r}) = \left\{ \mu_L \left[\frac{dU_n(z)}{z} + k_n W_n(z) \right] \left[m \frac{J_m(k_nr)}{k_nr} - J_{m+1}(k_nr) \right] \right\} e^{im\theta}. \quad (2.3.2f)$$

Shear-horizontal (SH) wave mode basis functions are in the form of

$$\varphi_n^m(\mathbf{r}) = \begin{Bmatrix} V_n(z)imJ_m(k_nr)/k_nr \\ -V_n(z)J'_m(k_nr) \\ 0 \end{Bmatrix} e^{im\theta}. \quad (2.3.3)$$

And the corresponding stress basis functions are in the form of

$$\sigma_{n,rr}^m(\mathbf{r}) = 2im\mu_L V_n(z) \left[(m-1) \frac{J_m(k_nr)}{k_nr^2} - \frac{J_{m+1}(k_nr)}{r} \right] e^{im\theta}, \quad (2.3.4a)$$

$$\sigma_{n,\theta\theta}^m(\mathbf{r}) = -\sigma_{n,rr}^m(\mathbf{r}), \quad (2.3.4b)$$

$$\sigma_{n,zz}^m(\mathbf{r}) = 0, \quad (2.3.4c)$$

$$\sigma_{n,r\theta}^m(\mathbf{r}) = \mu_L V_n(z) \left\{ -2 \frac{J_{m+1}(k_nr)}{r} + \left[k_n - \frac{2m(m-1)}{k_nr^2} \right] J_m(k_nr) \right\} e^{im\theta}, \quad (2.3.4d)$$

$$\sigma_{n,\theta z}^m(\mathbf{r}) = \mu_L \frac{dV_n(z)}{dz} \left[J_{m+1}(k_nr) - m \frac{J_m(k_nr)}{k_nr} \right] e^{im\theta}, \quad (2.3.4e)$$

$$\sigma_{n,rz}^m(\mathbf{r}) = im\mu_L \frac{dV_n(z)}{dz} \frac{J_m(k_nr)}{k_nr} e^{im\theta}. \quad (2.3.4f)$$

When an isotropic plate is considered, analytic solutions for $U_n(z)$, $W_n(z)$ and $V_n(z)$ in the eigenfunctions $\varphi_n^m(k, \mathbf{r})$ exist and its explicit expressions can be found in many literatures [62], [67], [68]. In case of a layered isotropic plate, analytic solutions also exist [3] but we recommend using a numerical method that will be discussed in Section 2.3.2. This numerical method called the pseudo-spectral collocation method for general transversely isotropic plates provides some convenient features when dealing with the scattering analysis technique that will be discussed in Chapter 3.

2.3.1 Analytic solutions for an isotropic plate

In this section, we summarize analytic solutions for an isotropic plate. In Section 2.2, we assumed that the top and the bottom surfaces are located at $z = 0, d$. However, when the expressions of analytic solutions for an isotropic plate are concerned, it is convenient to place the top and bottom surfaces at $z = \pm d/2 = \pm h$.

For the symmetric Lamb waves in an isotropic plate, U_n and W_n in Eq. 2.3.1 are in the form of

$$U_n(z) = k_n \cos(p_n z) + \gamma_{S,n} q_n \cos(q_n z), \quad (2.3.5a)$$

$$W_n(z) = -p_n \sin(p_n z) + \gamma_{S,n} k_n \sin(q_n z), \quad (2.3.5b)$$

$$\begin{aligned} \gamma_{S,n} &= \frac{(\lambda_L k_n^2 + \lambda_L p_n^2 + 2\mu_L p_n^2) \cos(p_n h)}{2\mu_L k_n q_n \cos(q_n h)} \\ &= \frac{2k_n p_n \sin(p_n h)}{[(k_n^2 - q_n^2)] \sin(q_n h)}, \end{aligned} \quad (2.3.5c)$$

$$p_n^2 = \frac{\omega^2}{c_l^2} - k_n^2, \quad q_n^2 = \frac{\omega^2}{c_t^2} - k_n^2, \quad (2.3.5d)$$

where c_l and c_t denote the longitudinal and transverse wave velocities, respectively. In the above equations k_n , p_n and q_n satisfy the well-known Rayleigh-Lamb frequency equation[60], [62], [63]:

$$\frac{\tan(q_n h)}{\tan(p_n h)} = -\frac{4p_n q_n k_n^2}{(q_n^2 - k_n^2)^2}. \quad (2.3.5e)$$

The coefficient E_n appearing in the Green's function as in Eq. (2.2.34) is

$$\begin{aligned} E_n &= \rho [h(k_n^2 + p_n^2) + \gamma_{S,n}^2 h(k_n^2 + q_n^2) + (k_n^2/p_n - p_n) \cos(h p_n) \sin(h p_n) \\ &\quad + 4\gamma_{S,n} k_n \cos(h p_n) \sin(h q_n) + \gamma_{S,n}^2 (q_n - k_n^2/q_n) \cos(h q_n) \sin(h q_n)]. \end{aligned} \quad (2.3.5f)$$

The eigenfunctions for the anti-symmetric Lamb waves in Eq. (2.3.1) are described by using the following expressions:

$$U_n(z) = k_n \sin(p_n z) - \gamma_{A,n} q_n \sin(q_n z), \quad (2.3.6a)$$

$$W_n(z) = p_n \cos(p_n z) + \gamma_{A,n} k_n \cos(q_n z), \quad (2.3.6b)$$

where

$$\begin{aligned} \gamma_{A,n} &= -\frac{(\lambda_L k_n^2 + \lambda_L p_n^2 + 2\mu_L p_n^2) \sin(p_n h)}{2\mu_L k_n q_n \sin(q_n h)} \\ &= -\frac{2k_n p_n \cos(p_n h)}{[(k_n^2 - q_n^2)] \cos(q_n h)}, \end{aligned} \quad (2.3.6c)$$

$$p_n^2 = \frac{\omega^2}{c_1^2} - k_n^2, \quad q_n^2 = \frac{\omega^2}{c_t^2} - k_n^2, \quad (2.3.6d)$$

For k_n , p_n and q_n , the following relations hold:

$$\frac{\tan(q_n h)}{\tan(p_n h)} = -\frac{(q_n^2 - k_n^2)^2}{4p_n q_n k_n^2}. \quad (2.3.6e)$$

The coefficient E_n is

$$E_n = \rho [h(k_n^2 + p_n^2) + \gamma_A^2 h(k_n^2 + q_n^2) - (k_n^2/p_n - p_n) \cos(hp_n) \sin(hp_n) + 4\gamma_A k_n \sin(hp_n) \cos(hq_n) - \gamma_A^2 (q_n - k_n^2/q_n) \cos(hq_n) \sin(hq_n)]. \quad (2.3.6f)$$

When the symmetric SH waves are considered, we have the following expressions for the eigenfunctions in Eq. (2.3.3) [60]:

$$V_n(z) = k_n \cos(s_n z), \quad (2.3.7a)$$

$$s_n^2 = \frac{\omega^2}{c_t^2} - k_n^2, \quad (2.3.7b)$$

and

$$E_n = \rho(1 + \delta_0) h k_n^2, \quad (2.3.7c)$$

where $\delta_0 = 1$, for SH₀ (the lowest symmetric SH wave) else 0. For the anti-symmetric SH waves, we have

$$V_n(z) = k_n \sin(s_n z), \quad (2.3.8a)$$

$$s_n^2 = \frac{\omega^2}{c_t^2} - k_n^2, \quad (2.3.8b)$$

$$E_n = \rho h k_n^2. \quad (2.3.8c)$$

The following SH wave dispersion relation is used to calculate k_n for a given ω :

$$\left(\frac{2k_n h}{\pi}\right)^2 = \left(\frac{2\omega h}{\pi c_t}\right)^2 - n^2, \quad (2.3.9)$$

where $n = 0, 2, 4, \dots$ for symmetric modes and $n = 1, 3, 5, \dots$ for anti-symmetric modes.

For the SH wave modes, the wavenumber k_n for a given ω can be very easily found by using Eq. (2.3.9). In case of the Lamb wave modes, the wavenumber k_n for a given ω in Eqs. (2.3.5e) and (2.3.5e) can be found only by numerical methods such as a root-finding algorithm. However, in most cases, it is recommended to use the numerical method described in the next section and use the analytic solutions only as a means of validation for the numerical method.

2.3.2 Numerical solutions by using the pseudo-spectral collocation method for a transverse isotropic plate

2.3.2.1 Matrix eigenvalue equations for the depth-dependent functions

When a transverse isotropic plate such as a layered plate as illustrated in Fig. 2.5 is considered, a problem becomes more complicated and a numerical technique is needed for the computation of $U_n(z)$, $W_n(z)$, $V_n(z)$ and k_n in Eqs. (2.3.1) and (2.3.3) at given frequency. For this computation, we adopt the method proposed by Denolle *et al.* [69] for seismic surface waves. However, frequency range of seismic waves is below 100 Hz and numerical tests of this method in typical NDE application frequency range (10 kHz \sim 20 MHz) show that the matrix representation for Lamb waves used by Denolle *et al.* results in wrong eigenvalues and eigenvectors caused by the badly scaled matrices. Therefore, we will introduce a different matrix representation of the governing equation for Lamb waves.

Substituting expressions for basis functions as in Eqs. (2.3.1) and (2.3.3) into the governing equations of elastic waves in Eq. (2.2.1) results in the governing equations for $U_n(z)$, $W_n(z)$ and $V_n(z)$. Let us consider SH waves first. A field $V = V(z)$ and a wavenumber k of SH waves satisfy the governing equation,

$$0 = \mu_L k^2 V - \frac{d}{dz} \left(\mu_L \frac{dV}{dz} \right) - \rho \omega^2 V. \quad (2.3.10)$$

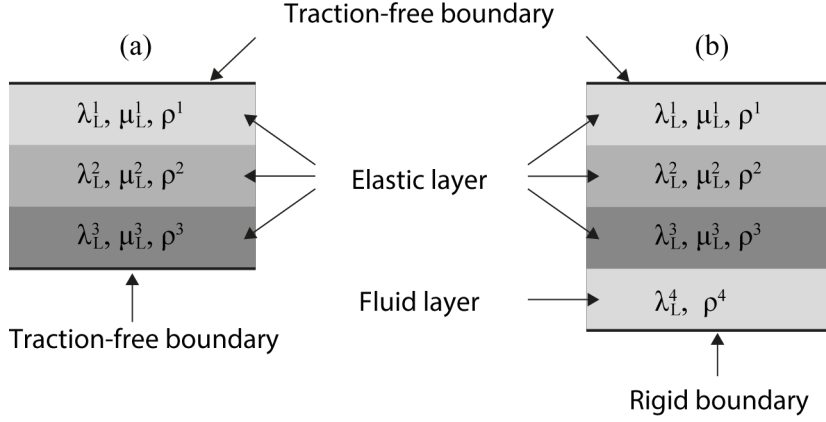


Figure 2.5 (a) Layered plate and (b) layered plate in contact with a fluid.

Eq. (2.3.10) can be written in the following form:

$$\left[\rho \omega^2 + \frac{d}{dz} \left(\mu_L \frac{d}{dz} \right) \right] [V] = k_n^2 [\mu_L] [V]. \quad (2.3.11)$$

The next step is to discretize V on $N + 1$ collocation points and to introduce the differentiation matrix \mathbf{D} of size $(N + 1) \times (N + 1)$ for the discretized field. Then, Eq. (2.3.11) becomes a matrix equation:

$$\left[\rho \omega^2 + \mathbf{D} (\mu_L \mathbf{D}) \right] \begin{bmatrix} V_1 \\ \vdots \\ V_{N+1} \end{bmatrix} = k^2 [\mu_L] \begin{bmatrix} V_1 \\ \vdots \\ V_{N+1} \end{bmatrix}. \quad (2.3.12)$$

In the above equation, ρ and μ_L are diagonal matrices whose elements represent ρ or μ_L on corresponding collocation points of the plate.

Now, the boundary conditions at the top and bottom surfaces must be applied in the above matrix equation. The traction-free boundary conditions are given from the stress-displacement relation as

$$0 = \mu_L \frac{dV}{dz}, \quad \text{at } z = 0, d. \quad (2.3.13)$$

Then, the first and the last row of the coefficient matrices in Eq. (2.3.12) should be replaced by the boundary conditions. Specifically, the first row of the coefficient matrix on the LHS in Eq. (2.3.12) is replaced by the first row of the matrix $\mu_L \mathbf{D}$. Similarly, the second row of the coefficient matrix on the LHS in Eq. (2.3.12) is replaced by the second row of the matrix $\mu_L \mathbf{D}$. Then, the first and the second row of the coefficient matrix on the RHS in Eq. (2.3.12) should be replaced by zeros.

In case of a plate composed of K layers in the thickness direction as illustrated in Fig 2.5(a), Eq. (2.3.11) becomes

$$\begin{aligned}
 & \begin{bmatrix} \rho_1 \omega^2 + \mathbf{D}_1 (\mu_{L,1} \mathbf{D}_1) & \cdots & \mathbf{0} \\ \vdots & \ddots & \vdots \\ \mathbf{0} & \cdots & \rho_K \omega^2 + \mathbf{D}_K (\mu_{L,K} \mathbf{D}_K) \end{bmatrix} \begin{bmatrix} V_1^1 \\ \vdots \\ V_{N_1+1}^1 \\ \vdots \\ V_1^K \\ \vdots \\ V_{N_K+1}^K \end{bmatrix} \\
 & = k^2 \begin{bmatrix} \mu_L^1 & \cdots & \mathbf{0} \\ \vdots & \ddots & \vdots \\ \mathbf{0} & \cdots & \mu_L^K \end{bmatrix} \begin{bmatrix} V_1^1 \\ \vdots \\ V_{N_1+1}^1 \\ \vdots \\ V_1^K \\ \vdots \\ V_{N_K+1}^K \end{bmatrix}. \tag{2.3.14}
 \end{aligned}$$

In this case, the displacement and the stress continuity condition at the interfaces be-

tween two layers should be also applied. Then, one finds:

$$\mu_L^1 \frac{dV^1}{dz} = \mu_L^2 \frac{dV^2}{dz}, \quad (2.3.15)$$

$$V^1 = V^2, \quad (2.3.16)$$

at the interfaces. For example, let us consider an interface between the first and second layers of the plate. Then, the $(N_1 + 1)^{\text{th}}$ rows of the coefficient matrices in Eq. (2.3.14) are replaced by the matrix representation of Eq. (2.3.15) and the next rows ($(N_1 + 2)^{\text{th}}$ rows) are replaced by by the matrix representation of Eq. (2.3.16). Other interfaces between layers can be treated similarly.

Next, we consider Lamb type waves. Fields $U = U(z)$ and $W(z)$, and a wavenumber k of Lamb type waves satisfy the governing equation,

$$\begin{aligned} k\lambda \frac{dW}{dz} + k \frac{d}{dz}(\mu W) + \frac{d}{dz} \left(\mu_L \frac{dU}{dz} \right) + \rho \omega^2 U &= k^2(\lambda_L + 2\mu_L)U, \\ -k\mu_L \frac{dU}{dz} - k \frac{d}{dz}(\lambda_L U) + \frac{d}{dz} \left[(\lambda_L + 2\mu_L) \frac{dW}{dz} \right] + \rho \omega^2 W &= k^2 \mu W, \end{aligned} \quad (2.3.17)$$

the boundary conditions at the top and bottom surfaces

$$\begin{aligned} -k\lambda_L U - (\lambda_L + 2\mu_L) \frac{dW}{dz} &= 0, \quad \text{at } z = 0, d, \\ k\mu_L W + \mu_L \frac{dU}{dz} &= 0, \quad \text{at } z = 0, d. \end{aligned} \quad (2.3.18)$$

Because Eq. (2.3.17) is a quadratic eigenvalue problem, we need to linearize this first. The linearization can be done by employing kU and kV as another variables. Then, Eq.

(2.3.17) can be put into the following form:

$$\begin{aligned}
 & \begin{bmatrix} 0 & 0 & \varepsilon & 0 \\ 0 & 0 & 0 & \varepsilon \\ \frac{d}{dz}\mu_L\frac{d}{dz} + \rho\omega^2 & 0 & 0 & \lambda_L\frac{d}{dz} + \frac{d}{dz}\mu_L \\ 0 & \frac{d}{dz}(\lambda_L + 2\mu_L)\frac{d}{dz} + \rho\omega^2 & -\mu_L\frac{d}{dz} - \frac{d}{dz}\lambda_L & 0 \end{bmatrix} \begin{bmatrix} U \\ W \\ kU \\ kW \end{bmatrix} \\
 & = k \begin{bmatrix} \varepsilon & 0 & 0 & 0 \\ 0 & \varepsilon & 0 & 0 \\ 0 & 0 & \lambda_L + 2\mu_L & 0 \\ 0 & 0 & 0 & \mu_L \end{bmatrix} \begin{bmatrix} U \\ W \\ kU \\ kW \end{bmatrix}, \tag{2.3.19}
 \end{aligned}$$

where ε is the scaling factor. The reason for introducing ε is that, although the above matrix representation is theoretically correct, when the sizes of certain elements of the above matrices differ by many orders of magnitude from those of others, it becomes numerically problematic. Therefore, to scale the problematic elements, we choose $\varepsilon = \omega^2$ for the examples in this dissertation and we also have confirm that this works well in typical NDE application frequency range (10 kHz \sim 20 MHz). The boundary conditions at the interfaces between two layers are

$$\begin{aligned}
 U^1 &= U^2, \\
 W^1 &= W^2, \\
 k\lambda_L^1 U^1 - (\lambda_L^1 + 2\mu_L^1)\frac{dW^1}{dz} &= k\lambda_L^2 U^2 - (\lambda_L^2 + 2\mu_L^2)\frac{dW^2}{dz}, \\
 k\mu_L^1 W^1 + \mu_L^1\frac{dU^1}{dz} &= k\mu_L^2 W^2 + \mu_L^2\frac{dU^2}{dz}. \tag{2.3.20}
 \end{aligned}$$

Then, the similar element scaling should be applied to the rows for the boundary conditions. The rest of the procedure is similar to SH wave cases.

In addition to purely elastic plates, fluid-loaded plates as illustrated in Fig 2.5(b), are commonly observed in many industrial fields. Thus, we extend the above equations to such problems. Here, we consider ideal (nonviscous) fluid which only has

irrotational fields. Theoretically, ideal fluid can be dealt with by using the elasticity equations with $\mu_L \rightarrow 0$. However, numerical tests show that the results obtained from the elasticity equations with $\mu_L \rightarrow 0$ is unstable and convergence of the solution is slow. Therefore, it is preferable to expand the fields in acoustic layers using the acoustic wave equations.

For this reason, let us consider a fluid layer below a plate which has a pressure field p whose depth-dependent function is described by $P(x)$. Then, one finds the governing equation for $P(x)$ as follows [2]:

$$\rho \frac{d}{dz} \left[\frac{1}{\rho} \frac{dP}{dz} \right] + \left[\frac{\omega^2}{c_f^2} - k^2 \right] P = 0. \quad (2.3.21)$$

The governing equation can be rewritten as

$$\begin{bmatrix} 0 & \varepsilon \\ K\rho \frac{d}{dz} \frac{1}{\rho} \frac{d}{dz} + \omega^2 \rho & 0 \end{bmatrix} \begin{bmatrix} P \\ kP \end{bmatrix} = k \begin{bmatrix} \varepsilon & 0 \\ 0 & K \end{bmatrix} \begin{bmatrix} P \\ kP \end{bmatrix}. \quad (2.3.22)$$

where we have used $c_f = \sqrt{K/\rho}$ and K denotes the bulk modulus of the fluid. In the above equation, the linearization used for Lamb type waves have been also adopted for coupling with equations for Lamb type waves. Note that, since the field is irrotational, it does not interact with SH waves. At the interface between solid and fluid layers, the boundary conditions for the continuity of the normal displacement and the normal traction are

$$\begin{aligned} \frac{1}{\rho \omega^2} \frac{dP}{dz} &= W, \\ 0 &= k\mu_L^1 W^1 + \mu_L^1 \frac{dU^1}{dz}, \\ -P &= k\mu_L^2 W^2 + \mu_L^2 \frac{dU^2}{dz}. \end{aligned} \quad (2.3.23)$$

In the above equation, we have used the pressure-displacement relation obtained from the Newton's second law [70]:

$$\nabla p = -\rho \frac{\partial^2 \mathbf{u}}{\partial t^2}. \quad (2.3.24)$$

The bottom of the fluid layer is usually described as a rigid wall with the following boundary condition:

$$\frac{1}{\rho \omega^2} \frac{dP}{dz} = 0. \quad (2.3.25)$$

2.3.2.2 Discretization of the depth-dependent functions

Now, a quadrature rule for the discretization of fields U , W , V and P should be chosen. Once a quadrature rule is chosen, the corresponding quadrature nodes, differentiation matrix and quadrature weights are specified. For example, the Chebyshev-Gauss-Lobatto quadrature rule can be employed. Then, the corresponding quadrature nodes in the interval $-1 \leq x \leq 1$ are defined by

$$x_n = -\cos \frac{n\pi}{N}, n = 0, \dots, N. \quad (2.3.26)$$

And the differentiation matrix related to the above nodes can be computed by using the method in Ref. [71], [72]. Using the nodes and the differentiation matrices with an appropriate scaling of domain, the matrix eigenvalue problem can be constructed. This matrix eigenvalue problem can be categorized as a generalized eigenvalue problem which can be solved by QZ algorithm implemented in most of standard linear algebra packages [73]–[75]. After solving the generalized eigenvalue problem, in most cases, the eigenvalues k are sorted in ascending order of the absolute value and used in order from the least to greatest value.

Once the field values on these nodes are found, the field values not on the nodes can be calculated using the backward discrete Chebyshev transform [76]:

$$U(x) = \sum_{n=0}^N \tilde{U}_n T_n(x), \quad (2.3.27)$$

where $T_n(x)$ is the Chebyshev polynomial defined by the recurrence relation,

$$T_{n+1}(x) = 2xT_n(x) - T_{n-1}(x), n \geq 1, \quad (2.3.28)$$

with $T_0(x) = 1$ and $T_1(x) = x$, or

$$T_n(x) = \cos n\theta, \quad \theta = \arccos x, \quad n \geq 0, \quad (2.3.29)$$

\tilde{U}_n can be evaluated by the forward discrete Chebyshev transform:

$$\tilde{U}_n = \frac{2}{\tilde{c}_n N} \sum_{j=0}^N \frac{1}{\tilde{c}_j} U(x_j) \cos \frac{nj\pi}{N}, \quad 0 \leq n \leq N, \quad (2.3.30)$$

where $\tilde{c}_0 = \tilde{c}_N = 2$ and $\tilde{c}_j = 1$ for $j = 1, 2, \dots, N-1$. Here, $U(x_j)$ corresponds to the calculated field value from the aforementioned eigenvalue problems.

And an integration involving the computed field values such as the ones in Chapter 3 can be done by using the Clenshaw-Curtis quadrature weights w_j in the following way:

$$\int_{-1}^1 f(x) dx \approx \sum_{j=0}^N f(x_j) w_j. \quad (2.3.31)$$

Clenshaw-Curtis quadrature weights w_j can be efficiently calculated using the fast Chebyshev transform [77].

2.3.2.3 Group velocity calculation

Another commonly used physical quantity for guided waves is the group velocity defined as

$$c_{g,n} = \frac{\partial \omega_n(k)}{\partial k}. \quad (2.3.32)$$

For a plate made of lossless materials, the group velocity of a guided wave mode can be obtained by using the computed field values and its derivatives [1], [69]. Here, we will show how the group velocity is related to the computed field values and this approach is different from that in Ref. [1]. In this context, we again consider two fields $\varphi_n(\mathbf{k}, \mathbf{r})$ and $\varphi_{n'}(-\mathbf{k}', \mathbf{r})$ in the Cartesian coordinate system same in guided wave mode n but

different in wavevector \mathbf{k} and $-\mathbf{k}'$, and the following equation similar to Eq. (2.2.56):

$$\begin{aligned} & \nabla \cdot [\boldsymbol{\sigma}_n(\mathbf{k}, \mathbf{r}) \cdot \boldsymbol{\varphi}_n(-\mathbf{k}', \mathbf{r}) - \boldsymbol{\sigma}_n(-\mathbf{k}', \mathbf{r}) \cdot \boldsymbol{\varphi}_n(\mathbf{k}, \mathbf{r})] \\ &= \rho[\omega_n^2(-\mathbf{k}') - \omega_n^2(\mathbf{k})]\boldsymbol{\varphi}_n(\mathbf{k}, \mathbf{r}) \cdot \boldsymbol{\varphi}_n(-\mathbf{k}, \mathbf{r}). \end{aligned} \quad (2.3.33)$$

Integrating the above equation over the thickness direction yields

$$\begin{aligned} & i\Delta\mathbf{k} \cdot \int_0^d dz [\boldsymbol{\sigma}_n(\mathbf{k}, \mathbf{r}) \cdot \boldsymbol{\varphi}_n(-\mathbf{k}, \mathbf{r}) - \boldsymbol{\sigma}_n(-\mathbf{k}, \mathbf{r}) \cdot \boldsymbol{\varphi}_n(\mathbf{k}, \mathbf{r})] \\ &= \Delta\omega_n^2 \int_0^d dz \rho \boldsymbol{\varphi}_n(\mathbf{k}, \mathbf{r}) \cdot \boldsymbol{\varphi}_n(-\mathbf{k}, \mathbf{r}), \end{aligned} \quad (2.3.34)$$

where

$$\Delta\mathbf{k} = \mathbf{k} - \mathbf{k}', \quad \Delta\omega_n^2 = \omega_n^2(\mathbf{k}) - \omega_n^2(\mathbf{k}'). \quad (2.3.35)$$

Now, by using the definition of the normal vector $\mathbf{n} = \Delta\mathbf{k}/\Delta k$, Eq. (2.3.34) becomes

$$\begin{aligned} & i \int_0^d dz \mathbf{n} \cdot [\boldsymbol{\sigma}_n(\mathbf{k}, \mathbf{r}) \cdot \boldsymbol{\varphi}_n(-\mathbf{k}, \mathbf{r}) - \boldsymbol{\sigma}_n(-\mathbf{k}, \mathbf{r}) \cdot \boldsymbol{\varphi}_n(\mathbf{k}, \mathbf{r})] \\ &= \frac{\Delta\omega_n^2}{\Delta k} \int_0^d dz \rho \boldsymbol{\varphi}_n(\mathbf{k}, \mathbf{r}) \cdot \boldsymbol{\varphi}_n(-\mathbf{k}, \mathbf{r}). \end{aligned} \quad (2.3.36)$$

Taking the limit of $\Delta\omega_n^2/\Delta k$, meaning that \mathbf{k}' becomes close enough to \mathbf{k}' , and using the definition of the group velocity in Eq. (2.3.32) result in

$$\begin{aligned} & i \int_0^d dz \mathbf{n} \cdot [\boldsymbol{\sigma}_n(\mathbf{k}, \mathbf{r}) \cdot \boldsymbol{\varphi}_n(-\mathbf{k}, \mathbf{r}) - \boldsymbol{\sigma}_n(-\mathbf{k}, \mathbf{r}) \cdot \boldsymbol{\varphi}_n(\mathbf{k}, \mathbf{r})] \\ &= 2\omega_n(\mathbf{k})c_{g,n} \int_0^d dz \rho \boldsymbol{\varphi}_n(\mathbf{k}, \mathbf{r}) \cdot \boldsymbol{\varphi}_n(-\mathbf{k}, \mathbf{r}). \end{aligned} \quad (2.3.37)$$

$\tilde{\boldsymbol{\sigma}}_n(\mathbf{k}, z)$ and $\tilde{\boldsymbol{\varphi}}_n(\mathbf{k}, z)$ in the above equation are defined in Eq. (2.2.58).

Equation (2.3.37) can be further simplified. In this reason, let us consider the LHS of (2.3.37) first. For the normal vector n in Eq. (2.3.37), any unit vector on the x - y plane can be used. Here, we choose $\mathbf{n} = \hat{\mathbf{e}}_x$ and $\mathbf{k} = (k_n, 0, 0)$. Then LHS in Eq. (2.3.37)

becomes

$$\begin{aligned}
& i \int_0^d dz \hat{\mathbf{e}}_x \cdot [\boldsymbol{\sigma}_n(k_n, \mathbf{r}) \cdot \boldsymbol{\varphi}_n(-k_n, \mathbf{r}) - \boldsymbol{\sigma}_n(-k_n, \mathbf{r}) \cdot \boldsymbol{\varphi}_n(k_n, \mathbf{r})] \\
& = i \int_0^d dz [\boldsymbol{\sigma}_{n,xx}(k_n, \mathbf{r}) \varphi_{n,x}(-k_n, \mathbf{r}) + \boldsymbol{\sigma}_{n,xz}(k_n, \mathbf{r}) \varphi_{n,z}(-k_n, \mathbf{r}) \\
& \quad - \boldsymbol{\sigma}_{n,xx}(-k_n, \mathbf{r}) \varphi_{n,x}(k_n, \mathbf{r}) - \boldsymbol{\sigma}_{n,xz}(-k_n, \mathbf{r}) \varphi_{n,z}(k_n, \mathbf{r})].
\end{aligned} \tag{2.3.38}$$

Because of the explicit expressions $\boldsymbol{\varphi}_n$ and the stress-displacement relation, we have the following relations:

$$\begin{aligned}
\varphi_{n,x}(-k_n, \mathbf{r}) &= -\varphi_{n,x}(k_n, \mathbf{r}), \quad \varphi_{n,z}(-k_n, \mathbf{r}) = \varphi_{n,z}(k_n, \mathbf{r}), \\
\boldsymbol{\sigma}_{n,xx}(-k_n, \mathbf{r}) &= \boldsymbol{\sigma}_{n,xx}(k_n, \mathbf{r}), \quad \boldsymbol{\sigma}_{n,xz}(-k_n, \mathbf{r}) = -\boldsymbol{\sigma}_{n,xz}(k_n, \mathbf{r}).
\end{aligned} \tag{2.3.39}$$

Using the above relation and Eq. (2.3.38), Eq. (2.3.37) becomes

$$\begin{aligned}
& -2i \int_0^d dz [\boldsymbol{\sigma}_{n,xx}(k_n, \mathbf{r}) \varphi_{n,x}(k_n, \mathbf{r}) - \boldsymbol{\sigma}_{n,xz}(k_n, \mathbf{r}) \varphi_{n,z}(k_n, \mathbf{r})] \\
& = 2\omega_n c_{g,n} \int_0^d dz \rho [-\varphi_{n,x}(k, \mathbf{r}) \varphi_{n,x}(k, \mathbf{r}) + \varphi_{n,z}(k, \mathbf{r}) \varphi_{n,z}(k, \mathbf{r})].
\end{aligned} \tag{2.3.40}$$

Note that we used $\omega_n(k_n) = \omega$ in the above equation.

Now, with some manipulation, we have the following relation:

$$c_{g,n} = \frac{P_n}{\omega E_n}, \tag{2.3.41}$$

where for Lamb type modes,

$$E_n = \int_0^d dz \rho [U_n(z)^2 + W_n(z)^2], \tag{2.3.42a}$$

$$P_n = - \int_0^d dz [U_n(z) S_n^1(z) - W_n(z) S_n^3(z)], \tag{2.3.42b}$$

$$S_n^1(z) = -k_n(\lambda_L + 2\mu_L)U_n(z) + \lambda_L \frac{dW_n(z)}{dz}, \tag{2.3.42c}$$

$$S_n^3(z) = \mu_L \frac{dU_n(z)}{dz} + \mu_L k_n W_n(z), \quad (2.3.42d)$$

and for SH wave modes,

$$E_n = \int_0^d dz \rho [V_n(z)^2], \quad (2.3.43a)$$

$$P_n = k_n \int_0^d dz \mu_L [V_n(z) V_n'(z)]. \quad (2.3.43b)$$

2.4 Modeling of guided wave actuators

Many guided wave problems in plates are closely related to design and analysis of guided wave transducers. Therefore, researchers have developed analytic methods to solve fields generated by a surface traction for modeling guided wave transducers. A circular or a finite straight line traction have been rigorously analyzed by applying the Fourier transform or the Hankel transform [78], [79]. Somewhat informal analyses also appear in literatures [80], [81].

Using the derived Green's function in Section 2.2, many guided wave actuators can be easily modeled. These actuators include piezoelectric transducers, magnetostrictive transducers, electromagnetic acoustic transducers [78]–[88]. A force exerted by these transducers is commonly represented as a traction on the bottom or top surface of the plate $z = 0, d$. Then, the field $\mathbf{u}(\mathbf{r})$ actuated by a line traction is expressed by the following equation:

$$\mathbf{u}(\mathbf{r}) = \int_{l_{\text{ext}}} dl' \mathbf{G}(\mathbf{r}|\mathbf{r}') \cdot \mathbf{t}(\mathbf{r}'), \quad \text{at } z' = 0 \text{ or } d, \quad (2.4.1)$$

where l_{ext} denotes a line on the surface of the plate exerted by a traction and $\mathbf{t}(\mathbf{r}')$ is a traction vector defined on this line.

Then, at this point, what we need to do is choose a Green's function that is appropriate for the given problem. In what follows, we will show how the derived Green's function in a multipole expansion form as in Eq. (2.2.34) can be employed to obtain analytic expressions for guided wave actuator models. This will be also used to calculate the coefficient vectors of incident waves in scattering analyses in Chapter 3.

In this context, the Green's function in Eq. (2.2.34a) is substituted into Eq. (2.4.1):

$$\mathbf{u}(\mathbf{r}) = \int_{l_{\text{ext}}} dl' \sum_{n,m} \frac{(-1)^m i k_n}{4P_n} \bar{\varphi}_n^m(k_n, \mathbf{r}) \varphi_n^{-m}(k_n, \mathbf{r}') \cdot \mathbf{t}(\mathbf{r}'). \quad (2.4.2)$$

The above equation can be rewritten as

$$\mathbf{u}(\mathbf{r}) = \sum_{n,m} c_n^m \bar{\varphi}_n^m(k_n, \mathbf{r}). \quad (2.4.3)$$

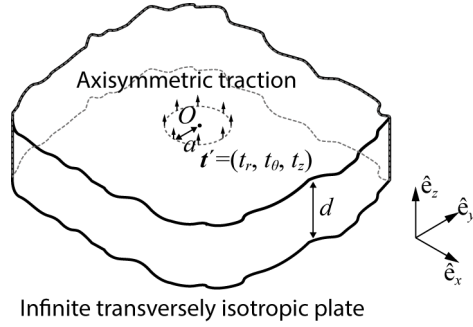


Figure 2.6 Guided wave actuation by an axisymmetric traction on the surface of an infinite plate.

where

$$c_n^m = \frac{(-1)^m i k_n}{4P_n} \int_{l_{\text{ext}}} dl' \varphi_n^{-m}(k_n, \mathbf{r}') \cdot \mathbf{t}(\mathbf{r}'). \quad (2.4.4)$$

Based on Eq. (2.4.3), we derive an analytic field expressions for some basic actuator models in the following section.

2.4.1 Axisymmetric line tractions

An axisymmetric guided wave actuators can be found in many literatures [78], [79], [86], [87]. Although analytic expression of axisymmetric actuators have been also suggested [78], [79], we here provide more simple procedures for deriving such expressions. Furthermore, the following results can be also applicable to transversely isotropic plates.

Let us consider an axisymmetric line traction vector $\mathbf{t}'(\mathbf{r}')$ of radius a on the top surface $z = d$ as illustrated in 2.6 which can be put into the following general form:

$$\mathbf{t}'(\mathbf{r}') = [t_r \hat{\mathbf{e}}_r + t_\theta \hat{\mathbf{e}}_\theta + t_z \hat{\mathbf{e}}_z], \quad \text{at } r' = a \text{ and } z' = d. \quad (2.4.5)$$

For actuation of Lamb type waves, we choose $t_\theta = 0$. Then, substituting Eq. (2.4.5)

into Eq. (2.4.4) yields the coefficient for the singular basis functions $\bar{\varphi}_n^m(k_n, \mathbf{r})$,

$$c_n^m = \frac{(-1)^m i k_n}{4P_n} \int_0^{2\pi} a d\theta' [\varphi_{n,r}^{-m}(k_n, (a, \theta', d))t_r + \varphi_{n,z}^{-m}(k_n, (a, \theta', d))t_z]. \quad (2.4.6)$$

Substituting Eq. (2.3.1) and (2.3.3) in (2.4.6) shows that only the $m = 0$ terms of Lamb type modes are non-zero. Therefore,

$$c_n^0 = \frac{i k_n}{4P_n} 2\pi a [U_n(d)J_0'(k_n a)t_r + W_n(d)J_0(k_n a)t_z]. \quad (2.4.7)$$

For actuation of SH waves, we choose $t_r = 0$ and $t_z = 0$. Then, similar procedure yields,

$$c_n^0 = \frac{i k_n}{4P_n} 2\pi a [-V_n(d)J_0'(k_n a)t_\theta]. \quad (2.4.8)$$

2.4.2 Straight line tractions

Guided wave transducers that can be modeled as finite straight line traction vectors also can be found in many literatures [81], [83], [85]. When a traction under consideration is in the form of a finite straight line with uniform strength, an analytic solution of the resulting field can be obtained by using the plane wave expansion of the regular cylindrical wavefunction appearing in Eq. (2.4.4).

The plane wave expansion of the regular cylindrical function is given by Stratton [89] as follows:

$$J_m(kr)e^{im\theta} = \frac{i^{-m}}{2\pi} \int_0^{2\pi} e^{im\phi + ixk \cos \phi + iyk \sin \phi} d\phi. \quad (2.4.9)$$

Since the above equation is the integral of a periodic function, the integral can be efficiently approximated by using the N points rectangular rule [90]. Then, we have

$$\begin{aligned} J_m(kr)e^{im\phi} &= \frac{i^{-m}}{N} \sum_{\xi=0}^{N-1} e^{im\phi_\xi} e^{i\mathbf{k}_\xi \cdot \mathbf{r}}, \\ &= \sum_{\xi=0}^{N-1} w_\xi^m e^{i\mathbf{k}_\xi \cdot \mathbf{r}}, \end{aligned} \quad (2.4.10)$$

where $\phi_\xi = 2\pi\xi/N$ and

$$\begin{aligned}\mathbf{k}_\xi &= k_{\xi,x}\hat{\mathbf{e}}_x + k_{\xi,y}\hat{\mathbf{e}}_y \\ &= k[\cos\phi_\xi\hat{\mathbf{e}}_x + \sin\phi_\xi\hat{\mathbf{e}}_y],\end{aligned}\tag{2.4.11}$$

$$\begin{aligned}\mathbf{r} &= x\hat{\mathbf{e}}_x + y\hat{\mathbf{e}}_y + z\hat{\mathbf{e}}_z \\ &= r[\cos\theta\hat{\mathbf{e}}_x + \sin\theta\hat{\mathbf{e}}_y] + z\hat{\mathbf{e}}_z.\end{aligned}\tag{2.4.12}$$

In the above equations, we have used the weighting function w_ξ^m ,

$$w_\xi^m = \frac{i^{-m}}{N} e^{im\phi_\xi}.\tag{2.4.13}$$

Although there is no formal rule for determining N , it is empirically chosen to be $N > 2(|kr| + |m|) + 1$. Then, by replacing the cylindrical wavefunctions appearing in Eqs. (2.3.1) and (2.3.1) with the expression in Eq. (2.4.10), the cylindrical wave basis functions in Eq. (2.4.4) can be expressed in terms of the plane wave basis functions in Eqs. (2.2.53) and (2.2.54):

$$\begin{aligned}\varphi_n^m(\mathbf{r}) &= \sum_{\xi=0}^{N-1} w_\xi^m \varphi_n(\mathbf{k}_\xi, \mathbf{r}) \\ &= \sum_{\xi=0}^{N-1} w_\xi^m \tilde{\varphi}_n(\mathbf{k}_\xi, z) e^{i\mathbf{k}_\xi \cdot \mathbf{r}}\end{aligned}\tag{2.4.14}$$

where $\tilde{\varphi}_n(\mathbf{k}_\xi, z)$ denotes z -dependent functions as in Eq. (2.2.58).

Now, let us consider a line traction \mathbf{t} on the top surface as illustrated in Fig. 2.7 with $\psi = 0$:

$$\mathbf{t} = t_x\hat{\mathbf{e}}_x + t_y\hat{\mathbf{e}}_y + t_z\hat{\mathbf{e}}_z, \text{ for } x = 0, -L < y < L, z = d.\tag{2.4.15}$$

By substituting Eqs.(2.4.14) and (2.4.15) into Eq.(2.4.4), we have the coefficients for

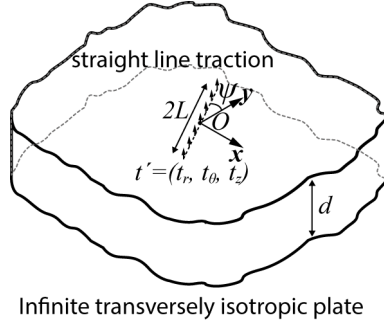


Figure 2.7 Guided wave actuation by a straight line traction having finite length on the surface of an infinite plate.

the outgoing waves represented by $\bar{\varphi}_n^m(k_n, \mathbf{r})$:

$$\begin{aligned}
 c_n^m &= \frac{(-1)^m k_n}{4P_n} \sum_{\xi=0}^{N-1} w_{\xi}^{-m} \tilde{\varphi}_n(\mathbf{k}_{\xi}, d) \cdot \mathbf{t} \int_{-L}^L dy' e^{ik_{\xi y} y'} \\
 &= \frac{(-1)^m k_n}{4P_n} \sum_{\xi=0}^{N-1} w_{\xi}^{-m} \tilde{\varphi}_n(\mathbf{k}_{\xi}, d) \cdot \mathbf{t} \frac{2}{k_{\xi y}} \sin k_{\xi y} L.
 \end{aligned} \tag{2.4.16}$$

Next, we consider a case where a line traction is not aligned with an coordinate axis. In this case, a traction is represented as

$$\mathbf{t}_1 = t_{x_1} \hat{\mathbf{e}}_{x_1} + t_{y_1} \hat{\mathbf{e}}_{y_1} + t_z \hat{\mathbf{e}}_z, \text{ for } x_1 = 0, -L < y_1 < L, z = d, \tag{2.4.17}$$

where (x_1, y_1, z) represents a coordinate system inclined in an angle of ψ in counter-clockwise (CCW) direction with respect to the (x, y, z) coordinate system. Then, substituting Eqs.(2.4.14) and (2.4.17) into Eq.(2.4.4), we have the coefficients for $\bar{\varphi}_n^m(k_n, \mathbf{r})$ as follows:

$$\begin{aligned}
 c_n^m &= \frac{(-1)^m k_n}{4P_n} \sum_{\xi=0}^{N-1} w_{\xi}^{-m} \tilde{\varphi}_n(\mathbf{k}_{\xi_1}, d) \cdot \mathbf{t}_1 \int_{-L}^L dy'_1 e^{ik_{\xi_1 y_1} y'_1} \\
 &= \frac{(-1)^m k_n}{4P_n} \sum_{\xi=0}^{N-1} w_{\xi}^{-m} \tilde{\varphi}_n(\mathbf{k}_{\xi_1}, d) \cdot \mathbf{t}_1 \frac{2}{k_{\xi_1 y_1}} \sin k_{\xi_1 y_1} L.
 \end{aligned} \tag{2.4.18}$$

where

$$\mathbf{k}_{\xi 1} = k_{\xi x 1} \hat{\mathbf{e}}_{x 1} + k_{\xi y 1} \hat{\mathbf{e}}_{y 1}. \quad (2.4.19)$$

$$k_{\xi x 1} = k_{\xi x} \cos \psi + k_{\xi y} \sin \psi, \quad k_{\xi y 1} = -k_{\xi x} \sin \psi + k_{\xi y} \cos \psi. \quad (2.4.20)$$

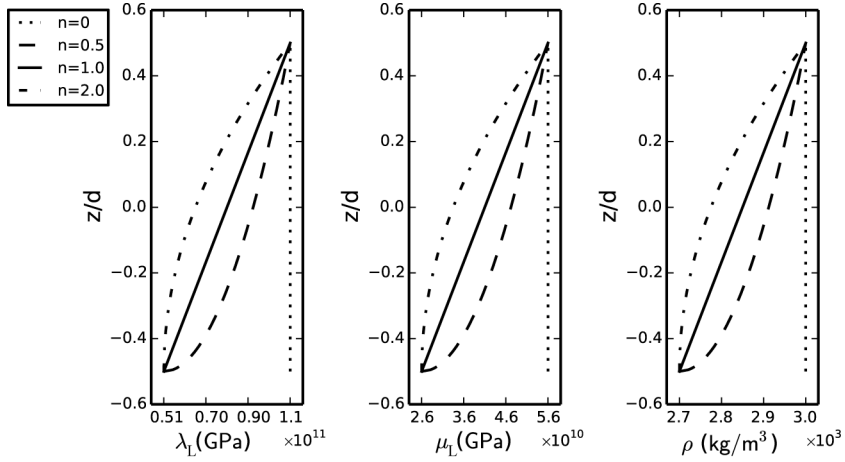


Figure 2.8 The material variation profile (λ_L , μ_L , ρ) of an aluminum-zirconia functionally graded plate governed by Eq. (2.5.1) with different values of n .

2.5 Numerical examples regarding functionally graded plates

In this section, we provide some examples regarding calculation of the basis functions in Section 2.3 and use of the derived green's functions in Section 2.2. Guided wave actuation models in Section 2.4 will be applied for functionally graded plates. Other types of isotropic or layered isotropic plates can be, of course, treated similarly.

2.5.1 Material properties of functionally graded plates

The functionally graded plates are assumed to have material properties — the Lamé constants λ_L , μ_L and mass density ρ — continuously varying through the thickness. The continuous change in material properties of functionally graded plates is known to reduce or avoid problems such as debonding and delamination between layers while these problems are likely to occur when there is a jump in mechanical properties across an interface of two different materials in layered plates.

In the subsequent examples, material properties are assumed to vary according

to a power-law distribution in terms of the volume fractions of the constituents by following the notations in Ref. [91]:

$$P(z) = (P_t - P_b)V + P_b, \quad (2.5.1a)$$

$$V = \left(\frac{z}{d} + \frac{1}{2}\right)^n, \quad (2.5.1b)$$

where P denotes a generic material property such as λ_L , μ_L or ρ , P_t and P_b denote the property at the top and bottom surfaces of the plate, respectively, d is the plate thickness, and n is a parameter for the material variation profile through the thickness.

As in Ref. [91], Aluminum-Zirconia plates are considered in the examples. The Young's modulus, Poisson's ratio and density for Aluminum used in the examples are 70 GPa, 2700 kg/m³, and 0.33, respectively. And for Zirconia, they are 151 GPa, 3000 kg/m³, and 0.33, respectively. We assumed that at the top surface of the plate, the material properties are taken to be those of Zirconia and, at the bottom surface, they are taken to be those of Aluminum. Therefore, for example, $E_t = 151$ GPa and $E_b = 70$ GPa.

2.5.2 Through-thickness mode shapes of guided waves

In this subsection, the through-thickness mode shapes $U(z)$, $W(z)$ and $V(z)$ in Eq. (2.3.1) and (2.3.3) of the aluminum-zirconia plate of frequency·thickness $fd = 500$ kHz·mm and of the material properties described by Eq. 2.5.1 with $n = 1$ were calculated. The pseudo-spectral collocation method in Section 2.3.2 was implemented by using double precision arithmetics in Python programming language and the NumPy package. The Chebyshev-Gauss-Lobatto quadrature rule in Eq. (2.3.26) was employed by using 30 nodes.

In Fig. 2.9, the through-thickness mode shapes for in-plane and out-of-plane motions of S_0 (extensional) — $U(z)$ and $W(z)$, respectively — are plotted. It is shown that the derivative of displacements are understandably continuous along the thickness

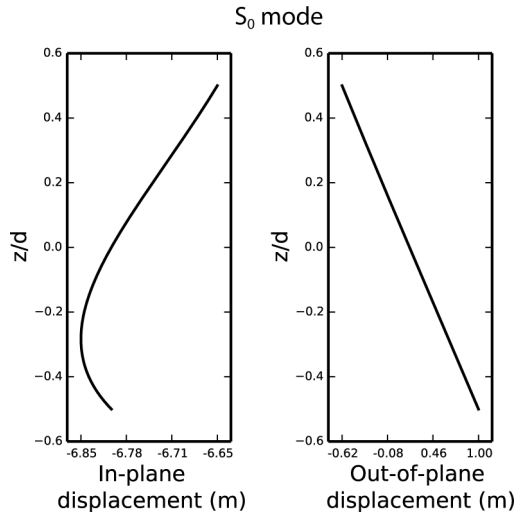


Figure 2.9 The through-thickness mode shape of the S_0 mode wave in an Aluminum-Zirconia functionally graded plate.

due to continuous material property profiles. It is observed that the motion is also not symmetric because the material property profile is not symmetric with respect to the mid-plane of the plate. However still, the motion retains characteristics of extensional waves, in-plane motions of the top and bottom surfaces are in-phase and out-of-plane motions are out-of-phase. A_0 (flexural) and SH_0 (shear-horizontal) waves.

The mode shapes of the A_0 mode are shown in Fig. 2.10, and characteristics of the flexural waves are observed. In Fig. 2.11, the mode shape of the SH_0 mode are shown.

From the results shown, it can be concluded that the motions of the basic 3 modes, S_0 (extensional), A_0 (flexural) and SH_0 (shear-horizontal) modes in functionally graded plates are almost similar to those of an isotropic plate.

For the purpose of comparison, we also provide in Fig. 2.12 the S_0 mode shape of an aluminum-zirconia layered plate of frequency·thickness $fd = 500\text{kHz} \cdot \text{mm}$ whose zirconia layer thickness to aluminum layer thickness ratio is 2:8. It is observed that, unlike the functionally graded plate, the derivative of displacements are not continuous

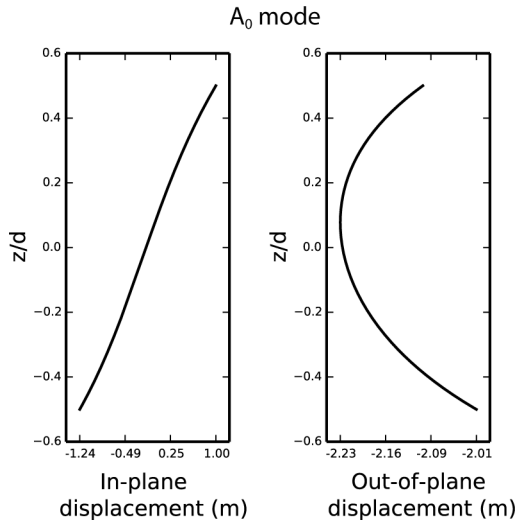


Figure 2.10 The through-thickness mode shape of the A_0 mode wave in an aluminum-zirconia functionally graded plate.

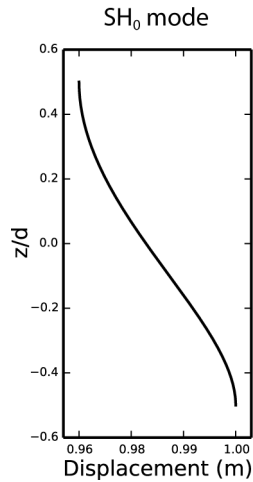


Figure 2.11 The through-thickness mode shape of the SH_0 mode wave in an aluminum-zirconia functionally graded plate.

across the interface between two layers due to the discontinuity of the material profile.

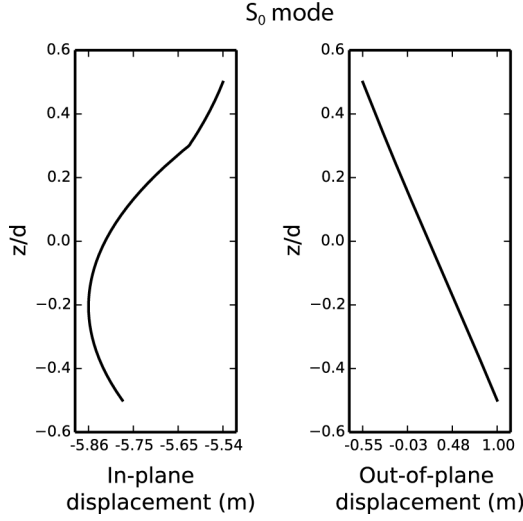


Figure 2.12 The through-thickness mode shape of the S_0 mode wave in an aluminum-zirconia layered plate.

2.5.3 Beam patterns of waves generated by a line traction

Here, we consider waves generated by a line traction on the top surface of the functionally graded plate defined by

$$\mathbf{t} = \hat{\mathbf{e}}_y, \text{ for } x = 0, -L < y < L, z = d. \quad (2.5.2)$$

which had been dealt with in Section 2.4.2. The frequency is $f = 500$ kHz and the thickness of the plate is $d = 1$ mm. The material properties of the functionally graded plate are described in Section 2.5.1. The coefficient for the basis functions can be calculated by using Eq. (2.4.16). Displacement fields were observed at $r = 0.01$ m on the top surface of the plate.

For validation of the theory, the same configuration is implemented in the finite element method discussed in detail in Appendix A.

Fig. 2.13 shows the beam patterns of the line traction evaluated by the theory. The results computed by the theory agrees very well with those computed by the finite

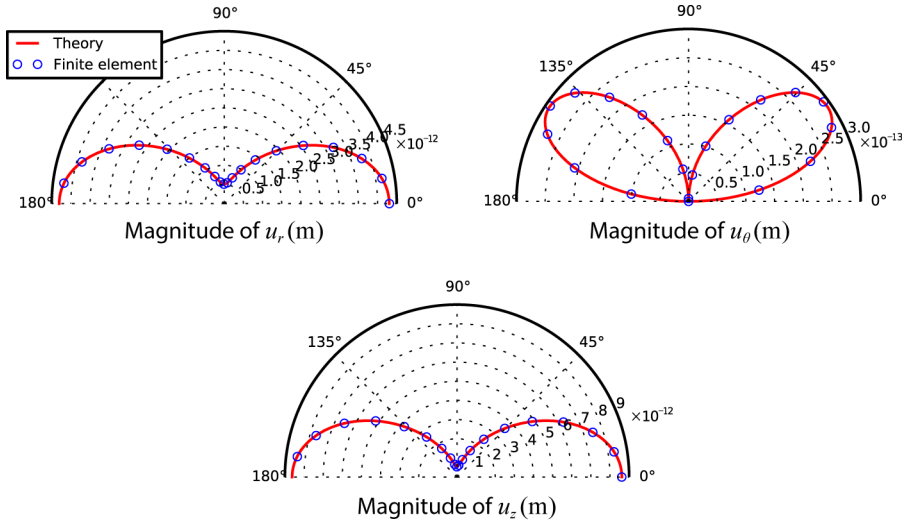


Figure 2.13 Beam patterns of guided waves generated by a line traction in Eq. (2.5.2) with $L = 2$ mm in the aluminum-zirconia functionally graded plate. The power-law material variation of the plate in Eq. (2.5.1) is governed by $n = 1$.

element method. Additionally, in Fig. 2.14, the beam patterns are compared according to the different power-law material variation in Eq. (2.5.1).

2.6 Approximate plate theories

In this section, we compare results obtained from using the derived Green's function based on the three-dimensional elasticity with those obtained from using the Green's function based on approximate plate theories for flexural waves in isotropic plates.

Since, many approximate plate theories for isotropic plates are well known to researchers in engineering fields [33], [35], [39], [92], we here only focus on results.

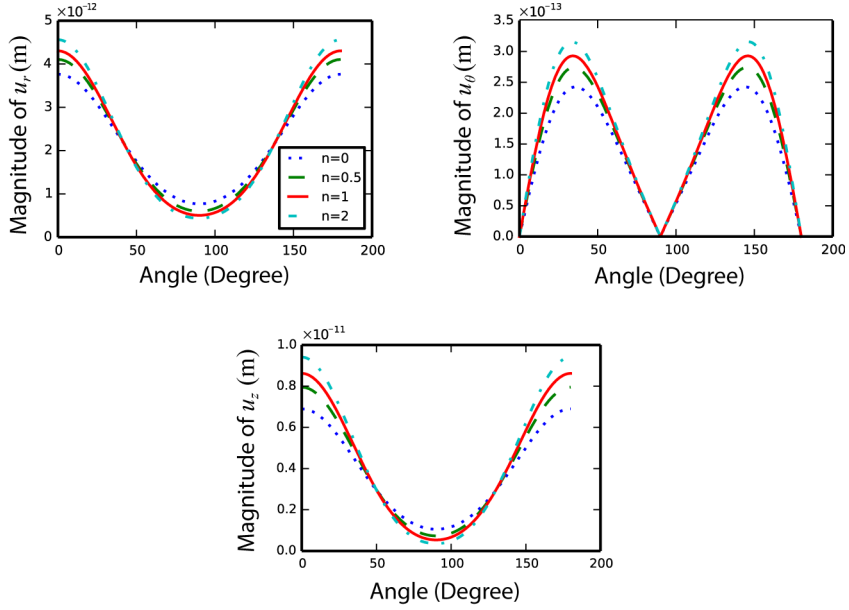


Figure 2.14 Comparison beam patterns of guided waves generated by a line traction in Eq. (2.5.2) with $L = 2$ mm according to the different power-law material variation of the aluminum-zirconia functionally graded plate in Eq. (2.5.1).

2.6.1 Kirchhoff plate theory

The lowest order approximate theory for flexural waves in plates is Kirchhoff theory and valid for very low-frequency range. vertical motion w is described by the following fourth order differential equation [35], [39]:

$$D\nabla^4 w - \rho d \omega^2 w = q, \quad (2.6.1)$$

where $D = Ed^3/12(1 - \nu^2)$ and q is applied load. The three displacement components are obtained from w as follows:

$$u_r = -z \frac{\partial w}{\partial r}, \quad u_\theta = -\frac{z}{r} \frac{\partial w}{\partial \theta}, \quad u_z = w. \quad (2.6.2)$$

For a vertical point load at the origin, $q/D = \delta(\mathbf{r})$, the solution to Eq. (2.6.1) is

given as [35], [93]

$$w_G(R) = \frac{i}{8Dk^2} [H_0^{(1)}(kR) - H_0^{(1)}(ikR)], \quad (2.6.3)$$

where $k = (\omega^2 \rho d / D)^{(1/4)}$ and R is distance from the origin.

2.6.2 Mindlin plate theory

Mindlin plate theory additionally includes shear-deformation and rotary-inertia effect being known to be accurate result for higher frequency range. In this theory, flexural waves are expressed by using the following equations of motion by using the rotation Ω and the deflection w [92]:

$$D \left(\nabla \nabla \cdot \Omega - \frac{1-\nu}{2} \nabla \times \nabla \times \Omega \right) + \bar{\mu} d (\nabla w - \Omega) + \frac{\rho d^3}{12} \omega^2 \Omega = \mathbf{m}, \quad (2.6.4a)$$

$$\bar{\mu} d \nabla \cdot (\nabla w - \Omega) + \rho d \omega^2 w = -q, \quad (2.6.4b)$$

where $D = Ed^3/12(1-\nu^2)$ denotes the flexural rigidity of the plate and $\bar{\mu} = \alpha^2 \mu$; \mathbf{m} is external bending moment; q is external vertical load. For the value of the shear coefficient α in subsequent examples, we use $\alpha^2 = \pi^2/12$ which is known to be correct for low-frequency behavior. Then, the three displacement components are obtained from Ω and w as follows:

$$u_r = -z\Omega_r, \quad u_\theta = -z\Omega_\theta, \quad u_z = w. \quad (2.6.5)$$

For a vertical point load at the origin, $\mathbf{m} = 0$, $q = \delta(\mathbf{r})$, the vertical motion in Eq. (2.6.4) is obtained as follows [92]:

$$w_G(R) = \frac{i}{4D(k_1^2 - k_2^2)} \left(\frac{H_0^{(1)}(k_1 R)}{\gamma_1} - \frac{H_0^{(1)}(k_2 R)}{\gamma_2} \right), \quad (2.6.6)$$

where

$$\gamma_j = 1 - \frac{\rho}{\bar{\mu}} \left(\frac{\omega}{k_j} \right)^2, \quad j = 1, 2,$$

$$k_{1,2}^2 = \frac{1}{2}(k_1^2 + k_1^2) \pm \sqrt{k_f^4 + \frac{1}{4}(k_1^2 - k_1^2)^2},$$

$$k_t = \frac{\omega}{c_t}, c_t = \left(\frac{\bar{\mu}}{\rho} \right)^{1/2}, k_l = \frac{\omega}{c_l}, k_f = \left(\frac{2\rho d \omega^2}{D} \right)^{1/4}.$$

2.6.3 Multipole expansion of flexural waves excited by arbitrary vertical loads

To obtain flexural waves generated by arbitrary vertical loads, we can superpose the point load solution as in Eqs. (2.6.3) and (2.6.6) over the region S of arbitrary vertical loads. However, for use of the solution in scattering problems as in Chapter 3, we should expand Eqs. (2.6.3) and (2.6.6) in terms of multipoles using Graf's addition theorem:

$$H_0^{(1)}(kR) = \sum_{m=-\infty}^{\infty} H_{-m}^{(1)}(kr') e^{-im\theta'} J_m(kr) e^{im\theta}, \quad b > r, \quad (2.6.7a)$$

$$H_0^{(1)}(kR) = \sum_{m=-\infty}^{\infty} J_{-m}(kr') e^{-im\theta'} H_m^{(1)}(kr) e^{im\theta}, \quad b < r. \quad (2.6.7b)$$

where

$$R^2 = (r \cos \theta - r' \cos \theta')^2 + (r \sin \theta - r' \sin \theta')^2. \quad (2.6.8)$$

Then, the resulting field can be calculated using the following relation [92]:

$$w(\mathbf{r}) = \int_S ds' w_G(\mathbf{r}|\mathbf{r}') q(\mathbf{r}'). \quad (2.6.9)$$

2.6.4 Comparison of the elasticity theory with plate theories

Here, we consider axisymmetric actuation of flexural wave as illustrated in Fig. 2.6 and compare results from the elasticity theory with those from plate theories. In examples, an aluminum plate of thickness $d = 1$ mm is excited by a vertical load (1 N/m) along a ring of radius $a = 2d$ on the top surface of the plate. Flexural waves are observed at $r = 100d$ on the top surface of the plate. In case of elasticity theory, other wave components, mainly S_0 wave, are neglected.

In Fig. (2.15), the results from elasticity theory, Kirchhoff and Mindlin plate theory are compared. The result from elasticity theory can be unarguably regarded as the

reference solution. In 0~200 kHz range, the magnitudes from different theories are consistent with each other. However, as to consistency of phase, the result from Kirchhoff theory starts to deviate around 25 kHz. The result from Mindlin plate theory also starts to show some phase deviation around 100 kHz, however in many cases, this level of deviation may be regarded as acceptable. In 200~400 kHz range, the magnitudes resulted from Kirchhoff theory deviates from others. Even Mindlin theory shows inconsistency in magnitude and phase from 300 kHz. In case of Mindlin theory, these inconsistency may be suppressed by changing the value of the shear coefficient α in Section 2.6.2. However, we could not find formal rule for choice of this value.

From this observation, we can conclude that approximate plate theories can provide results with relatively simple equations and implementation procedures for low-frequency range. However, care must be taken when mid or high-frequencies are concerned.

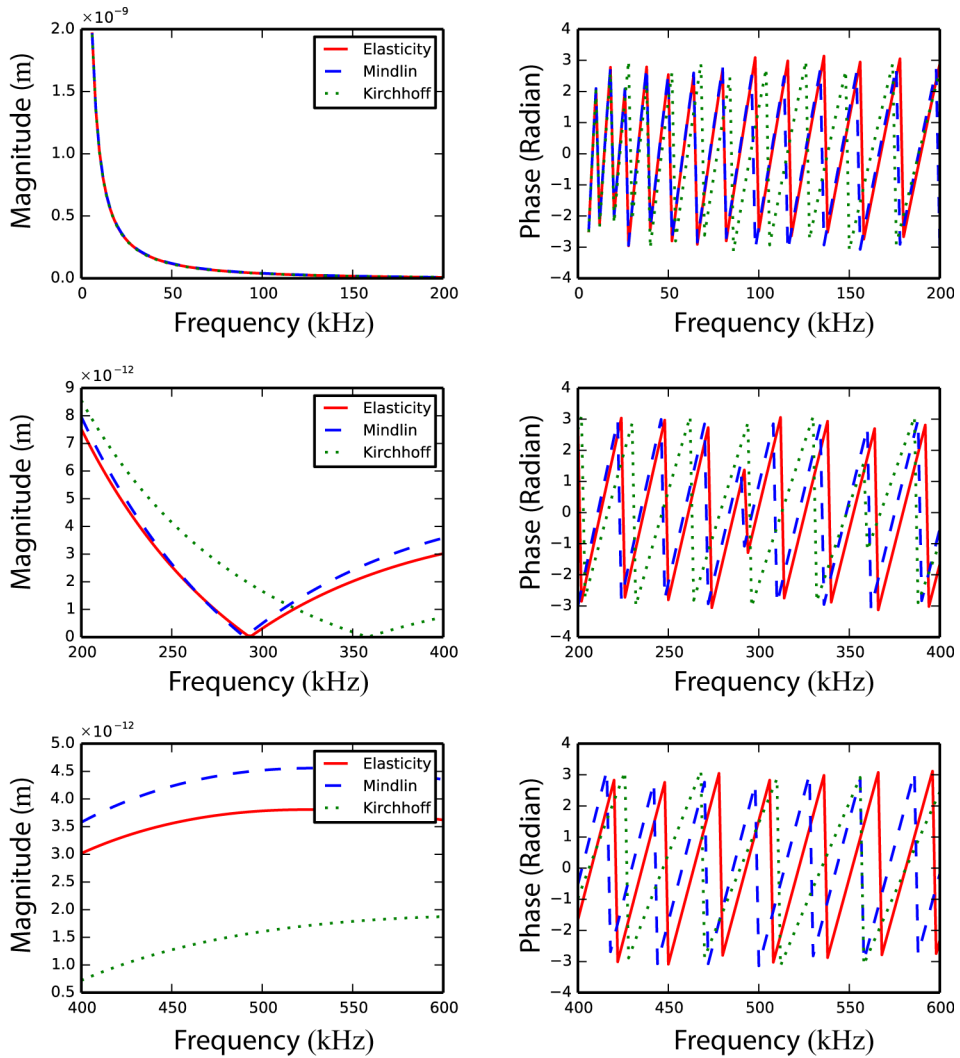


Figure 2.15 Flexural wave excited by an axisymmetric vertical load (1 N/m) on a ring of radius $a = 2d$ in an aluminum plate of thickness $d = 1$ mm. Flexural waves were observed at $r = 100d$.

Chapter 3

Scattering analysis for guided waves in a flat transversely isotropic plate by using the T -matrix method

We have discussed about the basis functions for guided waves in flat plates and derived the Green's function expanded in terms of the basis functions in the previous chapter. Now, we will discuss about the scattering analysis technique based on the transition-matrix (T -matrix) formalism. The T -matrix relates the coefficient vector of a scattered field to that of an incident field as described in Eq. (1.2.1).

First, we will discuss about the extended boundary condition method (EBCM) for calculation of the single scatterer T matrix. In theory, the EBCM is able to calculate the T matrix for any single scatterer of arbitrary shape and size. However, in practice, the EBCM can calculate T matrices for scatterers of certain simple shapes. Anyway, we will develop formulas that can deal with some of them such as a through hole, a step thickness reduction and increase. After discussion of the EBCM, we will discuss about a multiple scattering theory to construct the multiple scatterer T matrix based on the single scatterer T matrices obtained through the EBCM. Then, general properties of the T matrices representing the reciprocity, energy conservation and time-reversal invariance are derived. And finally, we develop a method to solve scattering problems

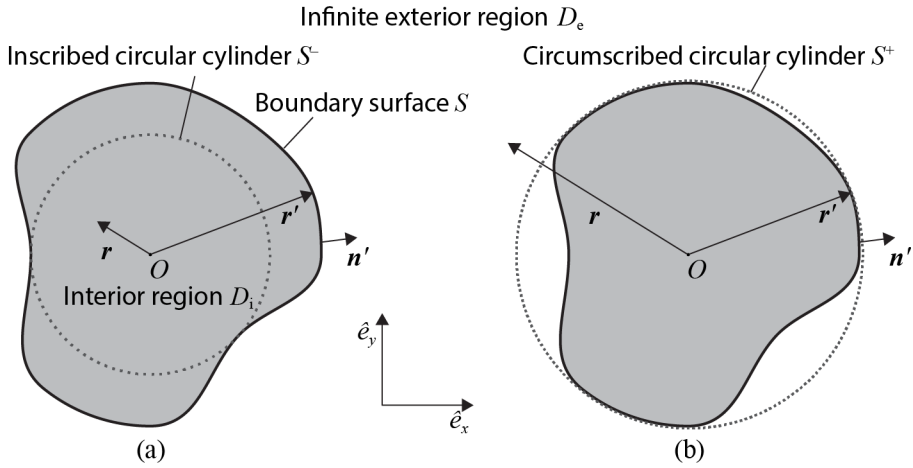


Figure 3.1 Notations used for the extended boundary condition method illustrated in the horizontal plane (the x - y plane) of a plate when the field point \mathbf{r} of Eqs. (3.1.1) and (3.1.2) is located (a) in D_i and (b) in D_e .

regarding arbitrarily shaped elastic inclusion.

3.1 T matrix calculation using the extended boundary condition method for a single scatterer

In this section, we will derive the transition-matrix (T matrix) for a single scatterer through the extended boundary condition method (EBCM) [56], [57] by using the Green's function for transversely isotropic plates derived in the preceding chapter.

3.1.1 The extended boundary condition method

Let us consider time-harmonic waves of excitation angular frequency ω with a scatterer D_i bounded by a surface S within an infinite exterior elastic plate D_e ; Fig. 3.1 shows notations related to the field point \mathbf{r} in D_i and \mathbf{r} in D_e illustrated in the horizontal plane (x - y plane) of the plate. The EBCM starts with the Helmholtz integral formula

also called the null-field integral equations [18], [94] for states a relation between the incident field $\mathbf{u}^{\text{inc}}(\mathbf{r})$ and the total field $\mathbf{u}(\mathbf{r})$:

$$\mathbf{u}^{\text{inc}}(\mathbf{r}) + \int_S ds' \{ \mathbf{u}'_+ \cdot [\mathbf{n}' \cdot \Sigma_0(\mathbf{r}'|\mathbf{r})] - \mathbf{t}'_+ \cdot \mathbf{G}_0(\mathbf{r}'|\mathbf{r}) \} = \begin{cases} \mathbf{u}(\mathbf{r}); & \mathbf{r} \in D_e, \\ 0; & \mathbf{r} \in D_i. \end{cases} \quad (3.1.1a)$$

and, for a scatterer that allows wave transmission through the boundary, another pair of equations can be defined

$$- \int_S ds' \{ \mathbf{u}'_- \cdot [\mathbf{n}' \cdot \Sigma_1(\mathbf{r}'|\mathbf{r})] - \mathbf{t}'_- \cdot \mathbf{G}_1(\mathbf{r}'|\mathbf{r}) \} = \begin{cases} \mathbf{u}(\mathbf{r}); & \mathbf{r} \in D_i, \\ 0; & \mathbf{r} \in D_e. \end{cases} \quad (3.1.2a)$$

In Eq. (3.1.1), \mathbf{u}' , \mathbf{t}' and \mathbf{n}' denote displacement field, traction field and normal vector on the surface S ; the subscripts '+' and '-' denote 'approached from D_e and D_i ', respectively; the strokes indicate that it is a function of \mathbf{r}' ; $\Sigma(\mathbf{r}'|\mathbf{r})$ is the stress counterpart of $\mathbf{G}(\mathbf{r}'|\mathbf{r})$ evaluated through the displacement-stress relation with respect to \mathbf{r} ; the subscripts '0' and '1' indicate 'for the exterior plate' and 'for the scatterer', respectively. Obviously, the total field is written as a sum of the incident field $\mathbf{u}^{\text{inc}}(\mathbf{r})$ and the scattered field $\mathbf{u}^{\text{sc}}(\mathbf{r})$ as

$$\mathbf{u}(\mathbf{r}) = \mathbf{u}^{\text{inc}}(\mathbf{r}) + \mathbf{u}^{\text{sc}}(\mathbf{r}), \quad (3.1.3)$$

where we assume that the incident and scattered displacement fields can be expanded in terms of the regular and singular basis functions in Eqs. (2.3.1) and (2.3.3):

$$\mathbf{u}^{\text{inc}}(\mathbf{r}) = \sum_{n_+, m} A_{n_+}^m \varphi_{n_+, 0}^m(\mathbf{r}), \quad (3.1.4a)$$

$$\mathbf{u}^{\text{sc}}(\mathbf{r}) = \sum_{n_+, m} \alpha_{n_+}^m \bar{\varphi}_{n_+, 0}^m(\mathbf{r}). \quad (3.1.4b)$$

where n_+ is the index for the expansion in terms of the guided wave modes for the exterior plate.

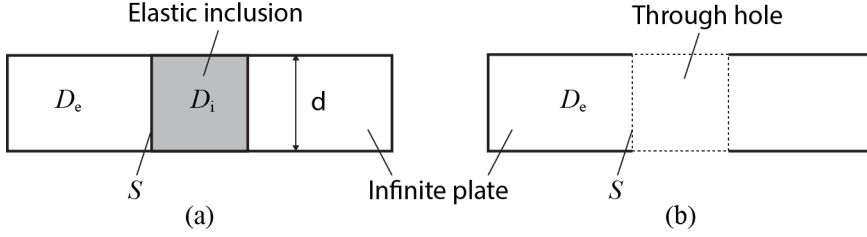


Figure 3.2 Illustrations for cross sections of (a) an elastic inclusion and (b) a through hole embedded in an exterior infinite plate. Thickness of the scatterer is same with that for the plate.

3.1.2 Derivation of the T matrix in case when a plate and a scatterer are of the same thickness

In this subsection, we will derived the T matrix when a scatterer and an exterior plate have the same thickness as illustrated in Fig. 3.2. In this case, only Eqs. (3.1.1)(a) and (3.1.1)(b) is used.

Let us first consider a field point \mathbf{r} lying inside S^- as in Fig. 3.1 (a). In this case, substituting Eqs. (2.2.34b) and (3.1.4a) into Eq. (3.1.1b) yields

$$\sum_{n_+,m} [a_{n_+}^m \varphi_{n_+,0}^m(\mathbf{r})] = - \sum_{n_+,m} \int_S ds' \{ \mathbf{u}'_+ \cdot [\mathbf{n}' \cdot \Sigma_{n_+,0}^m(\mathbf{r}'|\mathbf{r})] - \mathbf{t}'_+ \cdot \mathbf{G}_{n_+,0}^m(\mathbf{r}'|\mathbf{r}) \}, \mathbf{r} \text{ inside } S^-, \quad (3.1.5)$$

where

$$\mathbf{G}_{n_+,0}^m(\mathbf{r}'|\mathbf{r}) = \frac{(-1)^m i k_{n_+}}{4P_{n_+}} \bar{\varphi}_{n_+,0}^{-m}(\mathbf{r}') \varphi_{n_+,0}^m(\mathbf{r}), \quad (3.1.6a)$$

$$\Sigma_{n_+,0}^m(\mathbf{r}'|\mathbf{r}) = \frac{(-1)^m i k_{n_+}}{4P_{n_+}} \sigma(\bar{\varphi}_{n_+,0}^{-m}(\mathbf{r}')) \varphi_{n_+,0}^m(\mathbf{r}). \quad (3.1.6b)$$

In the above equations, $\mathbf{G}_0(\mathbf{r}'|\mathbf{r})$ was obtained from Eq. (2.2.44). Equating the coefficients of $\varphi_{n_+,0}^m(\mathbf{r})$ on the both sides of Eq. (3.1.5) yields

$$a_{n_+}^m = - \frac{(-1)^m i k_{n_+,0}}{4P_{n_+,0}} \int_S ds' \{ \mathbf{u}'_+ \cdot \mathbf{t}(\bar{\varphi}_{n_+,0}^{-m}(\mathbf{r}')) - \mathbf{t}'_+ \cdot \bar{\varphi}_{n_+,0}^{-m}(\mathbf{r}') \}, \quad (3.1.7)$$

where $\mathbf{t}(\bar{\varphi}_{n_+,0}^{-m}(\mathbf{r}'))$ denotes the traction vector obtained from applying the traction-displacement relation on $\bar{\varphi}_{n_+,0}^{-m}(\mathbf{r}')$. Similarly, for \mathbf{r} lying outside S^+ as in Fig. 3.1 (b), we substitute Eqs. (2.2.34a), (3.1.4b) into (3.1.1a) to obtain

$$\sum_{n_+,m} [\alpha_{n_+}^m \bar{\varphi}_{n_+,0}^m(\mathbf{r})] = \sum_{n_+,m} \int_S ds' \{ \mathbf{u}'_+ \cdot [\mathbf{n}' \cdot \Sigma_{n_+,0}^m(\mathbf{r}'|\mathbf{r})] - \mathbf{t}'_+ \cdot \mathbf{G}_{n_+,0}^m(\mathbf{r}'|\mathbf{r}) \}, \mathbf{r} \text{ outside } S^+, \quad (3.1.8)$$

where

$$\mathbf{G}_{n_+,0}^m(\mathbf{r}'|\mathbf{r}) = \frac{(-1)^m i k_{n_+,0}}{4P_{n_+,0}} \varphi_{n_+,0}^{-m}(\mathbf{r}') \bar{\varphi}_{n_+,0}^m(\mathbf{r}), \quad (3.1.9a)$$

$$\Sigma_{n_+,0}^m(\mathbf{r}'|\mathbf{r}) = \frac{(-1)^m i k_{n_+,0}}{4P_{n_+,0}} \boldsymbol{\sigma}(\varphi_{n_+,0}^{-m}(\mathbf{r}')) \bar{\varphi}_{n_+,0}^m(\mathbf{r}). \quad (3.1.9b)$$

Then, by equating the coefficients of $\bar{\varphi}_{n_+,0}^m(\mathbf{r})$ on the both sides of Eq. (3.1.8), the coefficient $\alpha_{n_+}^m$ can be written as

$$\alpha_{n_+}^m = \frac{(-1)^m i k_{n_+,0}}{4P_{n_+,0}} \int_S ds' \{ \mathbf{u}'_+ \cdot \mathbf{t}(\varphi_{n_+,0}^{-m}(\mathbf{r}')) - \mathbf{t}'_+ \cdot \varphi_{n_+,0}^{-m}(\mathbf{r}') \}. \quad (3.1.10)$$

For solving $A_{n_+}^m$ and $\alpha_{n_+}^m$, \mathbf{u}' and \mathbf{t}' on S should be expanded in terms of some basis function sets. For an elastic inclusion as in Fig. 3.2(a), the displacement and traction field continuity boundary conditions should be satisfied and therefore we use the following choice for the expansions [57]:

$$\begin{aligned} \mathbf{u}'_+ &= \sum_{\mu, \nu_+} d_{\nu_+}^{\mu} \varphi_{\nu_+,1}^{\mu}(\mathbf{r}'), \\ \mathbf{t}'_+ &= \sum_{\mu, \nu_+} d_{\nu_+}^{\mu} \mathbf{t}(\varphi_{\nu_+,1}^{\mu}(\mathbf{r}')). \end{aligned} \quad (3.1.11)$$

where ν_- is the index for the expansion in terms of the guided wave modes for the interior plate.

For a through hole as illustrated in Fig. 3.2(b), the traction-free boundary condition should be satisfied and therefore we use

$$\begin{aligned} \mathbf{u}'_+ &= \sum_{\mu, \nu_+} d_{\nu_+}^{\mu} \varphi_{\nu_+,0}^{\mu}(\mathbf{r}'), \\ \mathbf{t}'_+ &= 0. \end{aligned} \quad (3.1.12)$$

instead of Eq.(3.1.11).

If Eq. (3.1.11) is substituted into Eq. (3.1.7) and Eq. (3.1.10), the following relations in matrix form can be obtained:

$$\mathbf{a} = -\bar{\mathbf{Q}}\mathbf{d}, \quad \alpha = \mathbf{Q}\mathbf{d}. \quad (3.1.13)$$

where $\mathbf{a} = \{a_{n_+}^m\}$ and $\alpha = \{\alpha_{n_+}^m\}$ are the coefficient vectors of length $N_+(2M+1)$ if the number of guided wave modes in the expansion in z -direction (n_+ , v_+) for the exterior plate is N_+ and the highest terms in the expansions in θ (m , μ) is M . For instance, the coefficient vector \mathbf{a} is given by

$$\mathbf{a} = \left\{ a_0^{-M}, a_0^{-M+1}, \dots, a_0^M, a_{1,\dots}^{-M}, \dots, a_{1,\dots}^M, \dots, a_{N-1}^M \right\}^T.$$

The coefficient vector $\mathbf{d} = \{d_{v_-}^\mu\}$ for the surface field has the length $N_-(2M+1)$ if the number of guided wave modes in the expansion (v_-) for the interior plate is N_- . However, we here choose $N_- = N_+$ to make \mathbf{Q} and $\bar{\mathbf{Q}}$ square matrices. Therefore, $\bar{\mathbf{Q}}$ and \mathbf{Q} are square matrices of size $N_+(2M+1) \times N_+(2M+1)$ where

$$\bar{\mathbf{Q}} = [\bar{Q}_{n_+,v_+}^{m,\mu}], \quad \mathbf{Q} = [Q_{n_+,v_+}^{m,\mu}], \quad (3.1.14)$$

and, for an elastic inclusion,

$$\bar{Q}_{n_+,v_+}^{m,\mu} = \frac{(-1)^m i k_{n_+,0}}{4P_{n_+,0}} \int_S ds' \left\{ \varphi_{v_-,1}^\mu(\mathbf{r}') \cdot \mathbf{t}(\bar{\varphi}_{n_+,0}^{-m}(\mathbf{r}')) - \mathbf{t}(\varphi_{v_-,1}^\mu(\mathbf{r}')) \cdot \bar{\varphi}_{n_+,0}^{-m}(\mathbf{r}') \right\}, \quad (3.1.15a)$$

$$Q_{n_+,v_+}^{m,\mu} = \frac{(-1)^m i k_{n_+,0}}{4P_{n_+,0}} \int_S ds' \left\{ \varphi_{v_-,1}^\mu(\mathbf{r}') \cdot \mathbf{t}(\varphi_{n_+,0}^{-m}(\mathbf{r}')) - \mathbf{t}(\varphi_{v_-,1}^\mu(\mathbf{r}')) \cdot \varphi_{n_+,0}^{-m}(\mathbf{r}') \right\}, \quad (3.1.15b)$$

For a through hole, the second terms in the integrands of Eqs. (3.1.15a) and (3.1.15b) should be removed. Then, we have

$$\bar{Q}_{n_+,v_+}^{m,\mu} = \frac{(-1)^m i k_{n_+,0}}{4P_{n_+,0}} \int_S ds' \left\{ \varphi_{v_+,0}^\mu(\mathbf{r}') \cdot \mathbf{t}(\bar{\varphi}_{n_+,0}^{-m}(\mathbf{r}')) \right\}, \quad (3.1.16a)$$

$$Q_{n_+,v_+}^{m,\mu} = \frac{(-1)^m i k_{n_+,0}}{4P_{n_+,0}} \int_S ds' \left\{ \varphi_{v_+,0}^\mu(\mathbf{r}') \cdot \mathbf{t}(\varphi_{n_+,0}^{-m}(\mathbf{r}')) \right\}, \quad (3.1.16b)$$

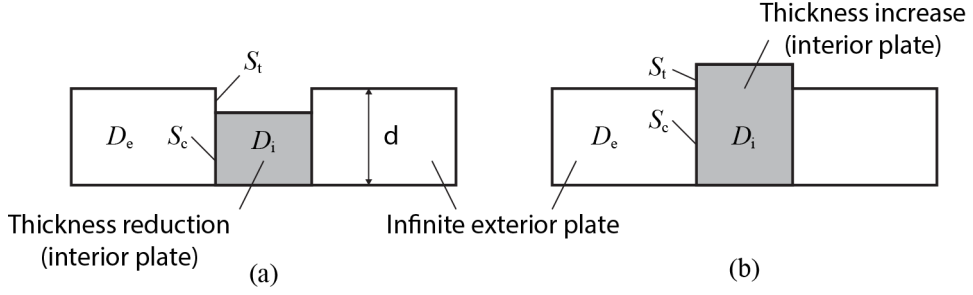


Figure 3.3 Illustrations for cross sections of (a) a thickness reduction and (b) a thickness increase embedded in an exterior infinite plate.

The explicit expressions of the displacement and stress basis functions for the above equations are given in Eqs. (2.3.1), (2.3.2), (2.3.3) and (2.3.4), and $P_{n,0}$ is defined in Eqs. (2.3.42b) and (2.3.43b). The matrix \mathbf{Q} , for instance, is arranged in the following form:

$$\mathbf{Q} = \begin{bmatrix} Q_{0,0}^{-M,-M} & Q_{0,0}^{-M,-M+1} & \cdots & Q_{0,N-1}^{-M,M} \\ Q_{0,0}^{-M+1,-M} & Q_{0,0}^{-M+1,-M+1} & \cdots & Q_{0,N-1}^{-M+1,M} \\ \vdots & \vdots & \ddots & \vdots \\ Q_{N-1,0}^{M,-M} & Q_{N-1,0}^{M,-M+1} & \cdots & Q_{N-1,N-1}^{M,M} \end{bmatrix}.$$

If \mathbf{a} , the coefficient vector for an incident wave, is given, the coefficients of the scattered field α are computed from

$$\alpha = \mathbf{TA}, \quad \mathbf{T} = -\mathbf{Q}\bar{\mathbf{Q}}^{-1}, \quad (3.1.17)$$

The numbers N and M determining the size of \mathbf{T} depend on the shape and size of the scatterer [44], [45].

3.1.3 Derivation of the T matrix in case when there is a thickness difference between a plate and a scatterer

In this subsection, we will derive the T matrix when a scatterer and an exterior plate have different thickness as illustrated in Fig. 3.3. In Fig. 3.3, S_c denote the boundary surfaces where the continuity condition is applied and S_t denote the boundary surfaces where the traction-free condition is applied; therefore, $S_c \cup S_t = S$. In this problem, the second pair of the null-field integral equation in Eq. (3.1.2) is also used in addition to the first pair in Eq. (3.1.1).

3.1.3.1 Interior plate having a step thickness reduction

We first consider the case of a step thickness reduction in Fig 3.3 (a). Following the same procedure as in the preceding subsection and rewriting Eqs. (3.1.7) and (3.1.10) yield

$$a_{n_+}^m = -\frac{(-1)^m i k_{n_+,0}}{4P_{n_+,0}} \left\{ \int_{S_c \cup S_t} ds' \mathbf{u}'_+ \cdot \mathbf{t}(\bar{\varphi}_{n_+,0}^{-m}(\mathbf{r}')) - \int_{S_c} ds' \mathbf{t}'_+ \cdot \bar{\varphi}_{n_+,0}^{-m}(\mathbf{r}') \right\}, \quad (3.1.18a)$$

$$\alpha_{n_+}^m = \frac{(-1)^m i k_{n_+,0}}{4P_{n_+,0}} \left\{ \int_{S_c \cup S_t} ds' \mathbf{u}'_+ \cdot \mathbf{t}(\varphi_{n_+,0}^{-m}(\mathbf{r}')) - \int_{S_c} ds' \mathbf{t}'_+ \cdot \varphi_{n_+,0}^{-m}(\mathbf{r}') \right\}. \quad (3.1.18b)$$

Note that in the second terms in the above two equations, the traction-free boundary condition \mathbf{t}'_+ has been applied to S_t .

Now, we choose \mathbf{u}'_+ and \mathbf{u}'_- to be expanded in terms of the displacement basis functions for the exterior plate and \mathbf{t}'_+ and \mathbf{t}'_- to be expanded in terms of the traction basis functions for the interior plate:

$$\begin{aligned} \mathbf{u}'_+ = \mathbf{u}'_- &= \sum_{\mu, v_+} d_{v_+}^\mu \varphi_{v_+,0}^\mu(\mathbf{r}'), \\ \mathbf{t}'_+ = \mathbf{t}'_- &= \sum_{\mu, v_-} g_{v_-}^\mu \mathbf{t}(\varphi_{v_-,1}^\mu(\mathbf{r}')), \end{aligned} \quad (3.1.19)$$

where v_+ and v_- are indices for the expansion in z -direction for the exterior plate and the interior region. Then, we choose N_+ to be the number of guided wave modes

(n_+, v_+) used for the exterior plate and N_- to be that (n_-, v_-) for the interior plate. Note that, by the above choices, the displacement and traction continuity boundary conditions are satisfied.

Then, by substituting Eq. (3.1.19) into Eqs. (3.1.18a) and (3.1.18b), we obtain the following matrix equations:

$$\mathbf{a} = -(\bar{\mathbf{M}}\mathbf{d} - \bar{\mathbf{N}}\mathbf{g}), \quad \alpha = \mathbf{M}\mathbf{d} - \mathbf{N}\mathbf{g}. \quad (3.1.20)$$

In the above equations, $\bar{\mathbf{M}} = \{\bar{M}_{n_+,v_+}^{m,\mu}\}$ is a square matrix of size $N_+(2M+1) \times N_+(2M+1)$ and $\bar{\mathbf{N}} = \{\bar{N}_{n_+,v_-}^{m,\mu}\}$ is a generally non-square matrix of size $N_+(2M+1) \times N_-(2M+1)$ where

$$\bar{M}_{n_+,v_+}^{m,\mu} = \frac{(-1)^m i k_{n_+,0}}{4P_{n_+,0}} \int_{S_+ \cup S_c} ds' \left[\boldsymbol{\varphi}_{v_+,0}^\mu(\mathbf{r}') \cdot \mathbf{t}(\bar{\boldsymbol{\varphi}}_{n_+,0}^{-m}(\mathbf{r}')) \right], \quad (3.1.21a)$$

$$\bar{N}_{n_+,v_-}^{m,\mu} = \frac{(-1)^m i k_{n_+,0}}{4P_{n_+,0}} \int_{S_c} ds' \left[\mathbf{t}(\boldsymbol{\varphi}_{v_-,1}^\mu(\mathbf{r}')) \cdot \bar{\boldsymbol{\varphi}}_{n_+,0}^{-m}(\mathbf{r}') \right]. \quad (3.1.21b)$$

\mathbf{M} and \mathbf{N} can be similarly obtained by replacing $\bar{\boldsymbol{\varphi}}_{n_+,0}^{-m}(\mathbf{r}')$ with $\boldsymbol{\varphi}_{n_+,0}^{-m}(\mathbf{r}')$.

Now, \mathbf{g} in Eq. (3.1.20) should be eliminated by using the another null-field integral equation in Eq. (3.1.2b). For this reason, we substitute Eq. (3.1.19) into Eq. (3.1.2b), and obtain the following matrix equation:

$$\mathbf{P}\mathbf{a} - \mathbf{R}\mathbf{b} = \mathbf{0}, \quad (3.1.22)$$

In the above equation, $\mathbf{P} = \{P_{n_-,v_+}^{m,\mu}\}$ is a generally non-square matrix of $N_-(2M+1) \times N_+(2M+1)$ size and $\mathbf{R} = \{R_{n_-,v_-}^{m,\mu}\}$ is a square matrix of $N_-(2M+1) \times N_-(2M+1)$ where

$$P_{n_-,v_+}^{m,\mu} = \frac{(-1)^m i k_{n_-,1}}{4P_{n_-,1}} \int_{S_c} ds' \left[\boldsymbol{\varphi}_{v_+,0}^\mu(\mathbf{r}') \cdot \mathbf{t}(\boldsymbol{\varphi}_{n_-,1}^{-m}(\mathbf{r}')) \right], \quad (3.1.23a)$$

$$R_{n_-,v_-}^{m,\mu} = \frac{(-1)^m i k_{n_-,1}}{4P_{n_-,1}} \int_{S_c} ds' \left[\mathbf{t}(\boldsymbol{\varphi}_{v_-,1}^\mu(\mathbf{r}')) \cdot \boldsymbol{\varphi}_{n_-,1}^{-m}(\mathbf{r}') \right]. \quad (3.1.23b)$$

From Eq. (3.1.22), we obtain following relation between \mathbf{d} and \mathbf{g} :

$$\mathbf{g} = \mathbf{R}^{-1}\mathbf{P}\mathbf{d}. \quad (3.1.24)$$

Substituting Eq. (3.1.24) into Eq. (3.1.20) yields

$$\mathbf{a} = -(\bar{\mathbf{M}} - \bar{\mathbf{N}}\mathbf{R}^{-1}\mathbf{P})\mathbf{d}, \quad \alpha = (\mathbf{M} - \mathbf{N}\mathbf{R}^{-1}\mathbf{P})\mathbf{d}. \quad (3.1.25)$$

Therefore, now we have the T matrix \mathbf{T} :

$$\alpha = \mathbf{T}\mathbf{a}, \quad \mathbf{T} = -\mathbf{Q}\bar{\mathbf{Q}}^{-1}, \quad (3.1.26)$$

where

$$\bar{\mathbf{Q}} = \bar{\mathbf{M}} - \bar{\mathbf{N}}\mathbf{R}^{-1}\mathbf{P}, \quad \mathbf{Q} = \mathbf{M} - \mathbf{N}\mathbf{R}^{-1}\mathbf{P}. \quad (3.1.27)$$

3.1.3.2 Interior plate having a step thickness increase

Next, we consider the case of a step thickness increase in inner plate with respect to that of the exterior plate as illustrated in Fig. 3.3 (b). We again follow the same procedure as in the preceding discussion and obtain the following equations:

$$a_{n_+}^m = -\frac{(-1)^m ik_{n_+,0}}{4P_{n_+,0}} \int_{S_c} ds' \left\{ \mathbf{u}'_+ \cdot \mathbf{t}(\bar{\varphi}_{n_+,0}^{-m}(\mathbf{r}')) - \mathbf{t}'_+ \cdot \bar{\varphi}_{n_+,0}^{-m}(\mathbf{r}') \right\}, \quad (3.1.28a)$$

$$\alpha_{n_+}^m = \frac{(-1)^m ik_{n_+,0}}{4P_{n_+,0}} \int_{S_c} ds' \left\{ \mathbf{u}'_+ \cdot \mathbf{t}(\varphi_{n_+,0}^{-m}(\mathbf{r}')) - \mathbf{t}'_+ \cdot \varphi_{n_+,0}^{-m}(\mathbf{r}') \right\}. \quad (3.1.28b)$$

In this case, we choose \mathbf{u}'_+ and \mathbf{u}'_- to be expanded in terms of the displacement basis functions for the interior plate and \mathbf{t}'_+ and \mathbf{t}'_- to be expanded in terms of the traction basis functions for the exterior plate:

$$\begin{aligned} \mathbf{u}'_+ &= \mathbf{u}'_- = \sum_{\mu, \nu_-} d_{\nu_-}^{\mu} \varphi_{\nu_-,1}^{\mu}(\mathbf{r}'), \\ \mathbf{t}'_+ &= \mathbf{t}'_- = \sum_{\mu, \nu_+} g_{\nu_+}^{\mu} \mathbf{t}(\varphi_{\nu_+,0}^{\mu}(\mathbf{r}')), \end{aligned} \quad (3.1.29)$$

where ν_+ and ν_- are indices for the expansion in z -direction for the exterior plate and the interior region. Then, we choose N_+ to be the number of guided wave modes (n_+ , ν_+) used for the exterior plate and N_- to be that (n_- , ν_-) for the interior plate.

Note that, by the above choices, the displacement and traction continuity boundary conditions are satisfied.

Then, by substituting Eq. (3.1.29) into Eqs. (3.1.28a) and (3.1.28b), we obtain the following matrix equations:

$$\mathbf{a} = -(\bar{\mathbf{M}}\mathbf{d} - \bar{\mathbf{N}}\mathbf{g}), \quad \alpha = \mathbf{M}\mathbf{d} - \mathbf{N}\mathbf{g}. \quad (3.1.30)$$

In the above equations, $\bar{\mathbf{M}} = \{\bar{M}_{n_+,v_-}^{m,\mu}\}$ is a generally non-square matrix of size $N_+(2M+1) \times N_-(2M+1)$ and $\bar{\mathbf{N}} = \{\bar{N}_{n_+,v_+}^{m,\mu}\}$ is a square matrix of size $N_+(2M+1) \times N_+(2M+1)$ where

$$\bar{M}_{n_+,v_-}^{m,\mu} = \frac{(-1)^m ik_{n_+,0}}{4P_{n_+,0}} \int_{S_c} ds' \left[\boldsymbol{\varphi}_{v_-,1}^\mu(\mathbf{r}') \cdot \mathbf{t}(\bar{\boldsymbol{\varphi}}_{n_+,0}^{-m}(\mathbf{r}')) \right], \quad (3.1.31a)$$

$$\bar{N}_{n_+,v_+}^{m,\mu} = \frac{(-1)^m ik_{n_+,0}}{4P_{n_+,0}} \int_{S_c} ds' \left[\mathbf{t}(\boldsymbol{\varphi}_{v_+,0}^\mu(\mathbf{r}')) \cdot \bar{\boldsymbol{\varphi}}_{n_+,0}^{-m}(\mathbf{r}') \right]. \quad (3.1.31b)$$

\mathbf{M} and \mathbf{N} can be similarly obtained by replacing $\bar{\boldsymbol{\varphi}}_{n_+,0}^{-m}(\mathbf{r}')$ with $\boldsymbol{\varphi}_{n_+,0}^{-m}(\mathbf{r}')$.

Now, \mathbf{d} in Eq. (3.1.30) should be eliminated by using the another null-field integral equation in Eq. (3.1.2b). For this reason, we substitute Eq. (3.1.29) into Eq. (3.1.2b), and obtain the following matrix equation:

$$\mathbf{P}\mathbf{d} - \mathbf{R}\mathbf{g} = \mathbf{0}, \quad (3.1.32)$$

In the above equation, $\mathbf{P} = \{P_{n_-,v_-}^{m,\mu}\}$ is a square matrix of $N_-(2M+1) \times N_-(2M+1)$ size and $\mathbf{R} = \{R_{n_-,v_+}^{m,\mu}\}$ is a generally non-square matrix of $N_-(2M+1) \times N_+(2M+1)$ where

$$P_{n_-,v_-}^{m,\mu} = \frac{(-1)^m ik_{n_-,1}}{4P_{n_-,1}} \int_{S_c \cup S_t} ds' \left[\boldsymbol{\varphi}_{v_-,1}^\mu(\mathbf{r}') \cdot \mathbf{t}(\boldsymbol{\varphi}_{n_-,1}^{-m}(\mathbf{r}')) \right], \quad (3.1.33a)$$

$$R_{n_-,v_+}^{m,\mu} = \frac{(-1)^m ik_{n_-,1}}{4P_{n_-,1}} \int_{S_c} ds' \left[\mathbf{t}(\boldsymbol{\varphi}_{v_+,0}^\mu(\mathbf{r}')) \cdot \boldsymbol{\varphi}_{n_-,1}^{-m}(\mathbf{r}') \right]. \quad (3.1.33b)$$

From Eq. (3.1.32), we obtain following relation between \mathbf{d} and \mathbf{g} :

$$\mathbf{d} = \mathbf{P}^{-1}\mathbf{R}\mathbf{g}. \quad (3.1.34)$$

Substituting Eq. (3.1.34) into Eq. (3.1.30) yields

$$\mathbf{a} = -(\bar{\mathbf{M}}\mathbf{P}^{-1}\mathbf{R} - \bar{\mathbf{N}})\mathbf{g}, \quad \alpha = (\mathbf{M}\mathbf{P}^{-1}\mathbf{R} - \mathbf{N})\mathbf{g}. \quad (3.1.35)$$

Therefore, now we have the T matrix \mathbf{T} :

$$\alpha = \mathbf{T}\mathbf{a}, \quad \mathbf{T} = -\mathbf{Q}\bar{\mathbf{Q}}^{-1}, \quad (3.1.36)$$

where

$$\bar{\mathbf{Q}} = \bar{\mathbf{M}}\mathbf{P}^{-1}\mathbf{R} - \bar{\mathbf{N}}, \quad \mathbf{Q} = \mathbf{M}\mathbf{P}^{-1}\mathbf{R} - \mathbf{N}. \quad (3.1.37)$$

3.1.4 Translation of fields generated by tractions to the coordinate system for the scatterer

We have discussed about fields excited by a line or surface traction on surfaces of plates (e.g., through a transducer) in Section 2.4. However, one of difficulties arises when dealing with the cylindrical coordinate system is that, unlike the rectangular coordinate system, it is not easy to relate two or more coordinate systems having different coordinate origin. For example, when we need the incident field coefficient vector for scattering problem as shown in Fig. 3.4, the radiated field calculated by Eq. (2.4.1) cannot be directly used because the coordinate system for describing the scatterer is different from that for the tractions.

In other words, in most of the cases, the resulting radiated field $\mathbf{u}(\mathbf{r}_{\text{ext}})$ from tractions is described in terms of the local coordinate system $\mathbf{r}_{\text{ext}} = (r_{\text{ext}}, \theta_{\text{ext}}, z)$ with an origin O_{ext} centered at $\mathbf{b}_{\text{ext}} = (b_{\text{ext}}, \beta_{\text{ext}}, 0)$ for the traction as illustrated in Fig. 3.5 on the horizontal plane (x - y plane) of the plate. Then, the results should be translated into that in the global coordinate system centered at \mathbf{O} for use in scattering problems. For example, in case of a line traction, the resulting field can be expressed in the local coordinate system \mathbf{r}_{ext} by using the form we discussed in Eq. (2.4.3):

$$\mathbf{u}(\mathbf{r}_{\text{ext}}) = \sum_{\nu, \mu} c_{\nu}^{\mu} \bar{\phi}_{\nu, 0}^{\mu}(\mathbf{r}_{\text{ext}}), \quad r_{\text{ext}} > \max(r'_{\text{ext}}), \quad (3.1.38a)$$

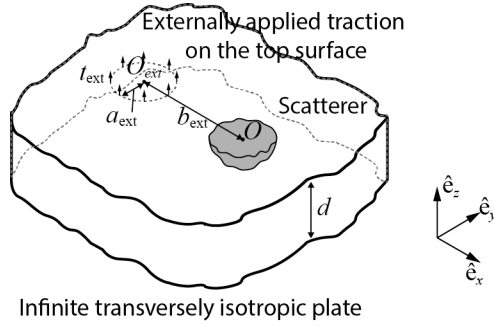


Figure 3.4 Guided wave incident on a scatterer by an externally applied traction.

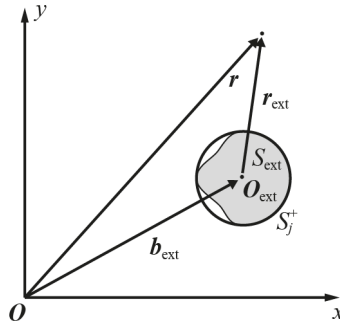


Figure 3.5 Notations used for translation between coordinate systems.

where

$$c_v^\mu = \frac{(-1)^\mu i k_{v,0}}{4P_{v,0}} \int_{l_{\text{ext}}} dl' \varphi_{v,0}^{-\mu}(\mathbf{r}'_{\text{ext}}) \cdot \mathbf{t}(\mathbf{r}'_{\text{ext}}). \quad (3.1.38b)$$

Here, $\max(r'_{\text{ext}})$ denotes the maximum value of r'_{ext} . Having obtained $\mathbf{c} = \{c_v^\mu\}$ in terms of the local coordinate, we can convert \mathbf{c} to \mathbf{a}_{ext} which is the coefficient vector in terms of the global coordinate by using the translational theorem that will be discussed in Eq. (3.2.1) of Section 3.2 as follows:

$$\mathbf{a}_{\text{ext}} = \bar{\mathbf{R}}(-\mathbf{b}_{\text{ext}})^T \mathbf{c}. \quad (3.1.39)$$

This form will be used throughout the rest of this chapter whenever externally applied tractions are concerned in scattering problems.

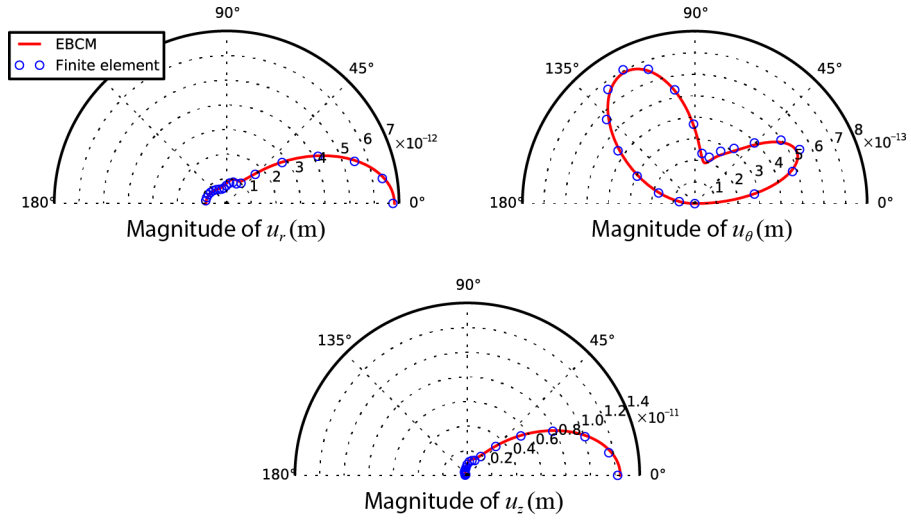


Figure 3.6 Scattered fields from circular cylindrical partly through-hole (step thickness reduction) of radius $\lambda_{A0}/2$ in an aluminum plate of $d = 1$ mm thickness. The thickness reduction of the scatterer compared to an exterior plate is 50 %.

3.1.5 Numerical examples

In this subsection, two numerical examples of the EBCM discussed in the preceding subsections are provided. The developed theories were implemented by using double-precision (16 decimal digits) arithmetics in the NumPy package of the Python programming language [74].

In the first example, we consider a circular part-through hole (step thickness reduction) of radius $\lambda_{A0}/2$ embedded in an aluminum plate of thickness of $d = 1$ mm; see Fig 3.3(a) for illustration. The thickness reduction of the inner plate is 50 % compared to the outer plate. The incident wave is actuated by a circular traction on the top surface of radius $a_{\text{ext}} = \lambda_{A0}/2$ located $b_{\text{ext}} = 3\lambda_{A0}$ from the center of the scatterer \mathbf{O} on the negative x -axis; see Fig. 3.4. The traction is of magnitude 1 N/m directing in z -axis. The considered frequency is 0.5 MHz. The scattered fields are observed on the

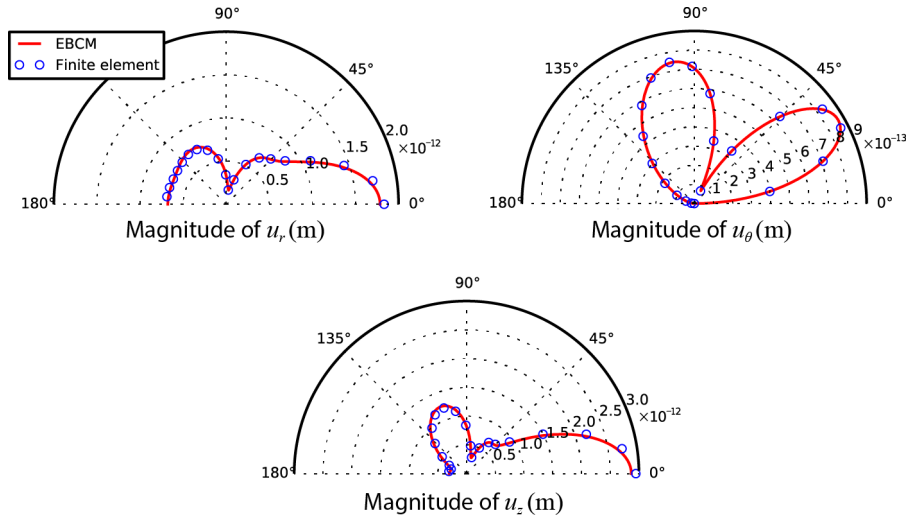


Figure 3.7 Scattered fields from circular cylindrical step thickness increase of radius $\lambda_{A0}/2$ in an aluminum plate of $d = 1$ mm thickness. The thickness increase of the scatterer compared to an exterior plate is 50 %.

top surface at $r = 5\lambda_{A0}$ from \mathbf{O} . For the EBCM, 8 guided wave modes are used for the expansion of fields in the exterior plate, and for the interior plate 5 guided wave modes are used. The configuration for the finite element method used as a reference solution is discussed in detail in Appendix A. Fig. 3.6 shows that the results obtained from the EBCM agrees well with those obtained from the finite element method indicating the validity of the developed theories.

In the second example, we consider a circular step thickness increase of radius $\lambda_{A0}/2$ embedded in an aluminum plate of thickness of $d = 1$ mm; see Fig 3.3(b) for illustration. The thickness increase of the inner plate is 50 % compared to the exterior plate. The incident wave is actuated by the same traction considered in the previous example except that another traction is added to the bottom surface of the plate. The considered frequency is also 0.5 MHz. For the EBCM, 10 guided wave modes are used for the expansion of fields in the exterior plate, and for the interior plate 16 guided

wave modes are used. Fig. 3.7 shows that the results obtained from the EBCM agrees well with those obtained from the finite element method indicating the validity of the developed theories.

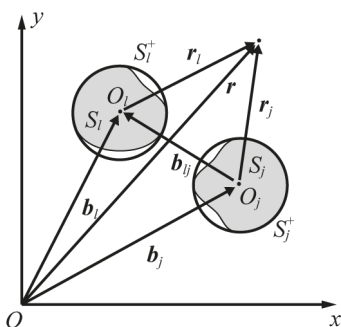


Figure 3.8 Notation for a coordinate translation of fields in the cylindrical coordinate system.

3.2 Multiple scattering analysis using the T -matrix method

3.2.1 Derivation of the T -matrix for multiple scatterers

Having obtained the T matrix in (3.1.17) for a single scatterer in Section 3.1.2, we can now calculate the scattered field from a finite number of multiple scatterers. Therefore, in this section, we explain a multiple scattering theory based on the T matrix formulation. While there are many multiple scattering algorithms available [15], [19]–[21], we here choose an algorithm in [15], [95] which works robustly also for both propagating and nonpropagating modes.

For the analysis, scatterers are assumed to have surfaces on the x - y plane denoted by S_l ($l = 1, 2, \dots, L$) with circumscribed circle S_l^+ as shown in Fig. 3.8. Since the field impinging upon S_l is composed of the externally applied incident field and field scattered from the other subscatterers except S_l itself, the T matrix in Eq. (3.1.17) is used to obtain the scattered field from S_l by the impinging field upon S_l . Because, the T matrix for S_l given by Eq. (3.1.17) is described in terms of its local coordinate system, the consideration of the interaction between S_l and the other subscatterer S_j requires a translational operator connecting the field variables defined in two different

coordinate systems. For the translational operation, it is convenient to introduce the global coordinate system (r, θ, z) centered at O , and the local coordinate systems (r_l, θ_l, z) and (r_j, θ_j, z) centered at O_l and O_j . The position vectors of O_l and O_j in the global coordinate system are denoted by $\mathbf{b}_l = (b_l, \beta_l, 0)$ and $\mathbf{b}_j = (b_j, \beta_j, 0)$ in Fig. 3.8 and \mathbf{b}_{lj} is defined as $\mathbf{b}_{lj} = \mathbf{b}_l - \mathbf{b}_j$.

The Graf's addition theorem used for translational operations in the cylindrical coordinate system is defined as [96],

$$J_m(kr_j)e^{im\theta_j} = \sum_{\mu=-\infty}^{\infty} J_{m-\mu}(kb_{lj})e^{i(m-\mu)\beta_{lj}}J_{\mu}(kr_l)e^{i\mu\theta_l}, \quad (3.2.1a)$$

$$H_m(kr_j)e^{im\theta_j} = \sum_{\mu=-\infty}^{\infty} H_{m-\mu}(kb_{lj})e^{i(m-\mu)\beta_{lj}}J_{\mu}(kr_l)e^{i\mu\theta_l}, \quad r_l < b_{lj}, \quad (3.2.1b)$$

$$H_m(kr_j)e^{im\theta_j} = \sum_{\mu=-\infty}^{\infty} J_{m-\mu}(kb_{lj})e^{i(m-\mu)\beta_{lj}}H_{\mu}(kr_l)e^{i\mu\theta_l}, \quad r_l > b_{lj}. \quad (3.2.1c)$$

Using the above equations, the field defined in the local coordinates of S_j can be rewritten in terms of the local coordinates of S_l . For this translational operation, we first substitute Eqs. (3.2.1) into the explicit expressions of $\varphi_n^m(\mathbf{r}_l)$ and $\bar{\varphi}_n^m(\mathbf{r}_l)$ which are the regular and singular basis functions for the exterior base plate (for explicit expressions, see Eqs. (2.3.1) and (2.3.3)) resulting in the following equations:

$$\varphi_n^m(\mathbf{r}_j) = \sum_{\mu, \nu} R_{n, \nu}^{m, \mu}(\mathbf{b}_{lj})\varphi_{\nu}^{\mu}(\mathbf{r}_l), \quad (3.2.2a)$$

$$\bar{\varphi}_n^m(\mathbf{r}_j) = \sum_{\mu, \nu} \bar{R}_{n, \nu}^{m, \mu}(\mathbf{b}_{lj})\varphi_{\nu}^{\mu}(\mathbf{r}_l), \quad r_l < b_{lj}, \quad (3.2.2b)$$

$$\bar{\varphi}_n^m(\mathbf{r}_j) = \sum_{\mu, \nu} R_{n, \nu}^{m, \mu}(\mathbf{b}_{lj})\bar{\varphi}_{\nu}^{\mu}(\mathbf{r}_l), \quad r_l > b_{lj}. \quad (3.2.2c)$$

where

$$\bar{R}_{n, \nu}^{m, \mu}(\mathbf{b}_{lj}) = \delta_{n\nu}H_{m-\mu}^{(1)}(k_nb_{lj})e^{i(m-\mu)\beta_{lj}}, \quad (3.2.2d)$$

and

$$R_{n, \nu}^{m, \mu}(\mathbf{b}_l) = \delta_{n\nu}J_{m-\mu}(k_nb_l)e^{i(m-\mu)\beta_l}. \quad (3.2.2e)$$

Now, for the multiple scattering analysis, we need the T matrix for a scatterer S_l defined as follows:

$$\alpha_l = \mathbf{T}_l \mathbf{a}_l, \quad (3.2.3)$$

where α_l is the coefficient vector of the field scattered from S_l . And the coefficient vector \mathbf{a}_l of the impinging field upon S_l is

$$\mathbf{a}_l = \mathbf{a}_{l,\text{ext}} + \sum_{j,j \neq l}^L \mathbf{a}_{l,j}, \quad l = 1, \dots, L, \quad (3.2.4)$$

where $\mathbf{a}_{l,\text{ext}}$ denote the contribution from an externally applied incident field expanded in terms the local coordinate system associated with S_l and $\mathbf{a}_{l,j}$, the contribution from the impinging field upon S_l by S_j . Then, by using Eq. (3.2.2b), the following relation can be established between the scattered field coefficient vector α_j of S_j and $\mathbf{a}_{l,j}$:

$$\mathbf{a}_{l,j} = \bar{\mathbf{R}}(\mathbf{b}_{lj})^T \alpha_j. \quad (3.2.5)$$

In the above equation, $\bar{\mathbf{R}}(\mathbf{b}_{lj}) = [\bar{R}_{n,v}^{m,\mu}(\mathbf{b}_{lj})]$ is the singular translational operator whose elements are defined in Eq. (3.2.2d). Similarly, $\mathbf{a}_{l,\text{ext}}$ is obtained from \mathbf{a}_{ext} given in terms of the global coordinate system:

$$\mathbf{a}_{l,\text{ext}} = \mathbf{R}(\mathbf{b}_l)^T \mathbf{a}_{\text{ext}}. \quad (3.2.6a)$$

In the above equation, $\mathbf{R}(\mathbf{b}_l) = [R_{n,v}^{m,\mu}(\mathbf{b}_l)]$ is the regular translational operator whose elements are similar to the one as in Eq. (3.2.2e),

$$R_{n,v}^{m,\mu}(\mathbf{b}_l) = \delta_{nv} J_{m-\mu}(k_n b_l) e^{i(m-\mu)\beta_l}. \quad (3.2.6b)$$

By substituting (3.2.4),(3.2.5), and (3.2.6a) into Eqs. (3.2.3), the following equation can be obtained:

$$\alpha_l = \mathbf{T}_l \left\{ \mathbf{R}(\mathbf{b}_l)^T \mathbf{a}_{\text{ext}} + \sum_{j,j \neq l}^L \bar{\mathbf{R}}(\mathbf{b}_{lj})^T \alpha_j \right\}, \quad l = 1, \dots, L. \quad (3.2.7)$$

The last step is to express α_l in the global coordinate system. If the contribution of α_l is simply denoted by α_l^G , the following relation holds:

$$\alpha_l^G = \mathbf{R}(-\mathbf{b}_l)^T \alpha_l. \quad (3.2.8)$$

Now, by using Eqs. (3.2.7) and (3.2.8), the clustered T matrix denoted by \mathbf{T} for multiple scatterers can be obtained:

$$\alpha = \mathbf{T} \mathbf{a}_{\text{ext}}, \quad (3.2.9)$$

where $\alpha = \{\alpha_1^G, \alpha_2^G, \dots, \alpha_L^G\}^T$. The matrix \mathbf{T} in Eq. (3.2.9) can be found to be

$$\mathbf{T} = \mathbf{E} \mathbf{D}^{-1} \mathbf{C}, \quad (3.2.10a)$$

where

$$\mathbf{D} = \begin{bmatrix} \mathbf{I} & -\mathbf{T}_1 \bar{\mathbf{R}}(\mathbf{b}_{12})^T & \cdots & -\mathbf{T}_1 \bar{\mathbf{R}}(\mathbf{b}_{1L})^T \\ -\mathbf{T}_2 \bar{\mathbf{R}}(\mathbf{b}_{21})^T & \mathbf{I} & \cdots & -\mathbf{T}_2 \bar{\mathbf{R}}(\mathbf{b}_{2L})^T \\ \vdots & \vdots & \ddots & \vdots \\ -\mathbf{T}_L \bar{\mathbf{R}}(\mathbf{b}_{L1})^T & -\mathbf{T}_L \bar{\mathbf{R}}(\mathbf{b}_{L2})^T & \cdots & \mathbf{I} \end{bmatrix},$$

$$\mathbf{E} = \begin{bmatrix} \mathbf{R}(-\mathbf{b}_1) \\ \mathbf{R}(-\mathbf{b}_2) \\ \vdots \\ \mathbf{R}(-\mathbf{b}_L) \end{bmatrix}^T, \quad \mathbf{C} = \begin{bmatrix} \mathbf{T}_1 \mathbf{R}(\mathbf{b}_1)^T \\ \mathbf{T}_2 \mathbf{R}(\mathbf{b}_2)^T \\ \vdots \\ \mathbf{T}_L \mathbf{R}(\mathbf{b}_L)^T \end{bmatrix}. \quad (3.2.10b)$$

Now, we discuss several considerations regarding the details of the multiple scattering analysis for computing scattered fields from multiple scatterers. Let us first consider an externally applied field incident on and a field scattered by multiple scatterers that can be accurately expressed with the number of guided wave modes N and a maximum multipolar order M_G in terms of the global coordinate system. Therefore, the T matrix for multiple scatterers has a size of $N(2M_G + 1) \times N(2M_G + 1)$. Furthermore, for a general distribution of scatterers, the number of guided wave modes used for each scatterer should be also N .

Now, let us take two scatterers S_j and S_l ($l \neq j$) with a maximum multipolar order M_j and M_l among a number of scatterers as an example. The scattered field from S_j expressed by M_j orders in its local coordinate is converted by Eq. (3.2.5) to an impinging field on S_l that may also include terms for $m \geq M_l$ orders. However, the T matrix for the scatterer S_l is unaffected by terms for $m > M_l$ orders. Therefore, $\bar{\mathbf{R}}(\mathbf{b}_{lj})^T$ in Eq.(3.2.5) used for \mathbf{D} in Eq. (3.2.10b) has size $N(2M_l + 1) \times N(2M_j + 1)$. The externally applied incident field with M_G on the original inclusion is also an impinging field upon S_l that also includes terms for $m \geq M_l$ orders. Since the T matrix for the subscatterer is unaffected by terms for $m > M_l$ orders, $\mathbf{R}(\mathbf{b}_l)^T$ in Eq. (3.2.6a) used for \mathbf{D} in Eq. (3.2.10b) has size $N(2M_l + 1) \times N(2M_G + 1)$. Similarly, the scattered field from S_l expressed by M_l orders is converted to the field that also includes terms for $M_G \geq m \geq M_l$ orders in the global coordinate by $\bar{\mathbf{R}}(-\mathbf{b}_l)^T$ of size $N(2M_G + 1) \times N(2M_l + 1)$ in Eq. (3.2.8) used for \mathbf{E} in Eq. (3.2.10b). The reason why the number $N(2M_G + 1)$ of rows in $\bar{\mathbf{R}}(-\mathbf{b}_l)^T$ should be greater than or equal to the number $N(2M_l + 1)$ of its columns is that every multipolar term must be accurately represented in the global coordinate system. In this way, the T matrix for the multiple scatterers so called ‘the clustered T matrix’ [15] can be obtained and its size is $N(2M_G + 1) \times N(2M_G + 1)$ as expected.

3.3 Properties of the T matrix

We have discussed about the transition-matrix (T matrix) for a single and multiple scatterers in the previous sections. In this section, we derive three common properties — the reciprocity, the energy conservation and the time-reversal invariance — of the T matrices for guided wave problems. In theory, the T matrix for a scatterer is unique regardless of derivation methods and should always satisfy properties which will be derived in the rest of this section.

For the derivation of these properties, orthogonality relations between displacement basis functions defined in Eqs. (2.3.1) and (2.3.3) should be first derived. Orthogonality relations of the basis functions can be categorized into two types; the real orthogonality and complex orthogonality relations which will be defined hereafter. The real orthogonality of the guided wave basis functions in the cylindrical coordinate is well known [60]. However, the complex orthogonality in the cylindrical coordinate necessary for derivation of the energy conservation and time-reversal invariance of the T matrix have not been derived. Therefore, we will derive the real and complex orthogonality relations in what follows; the derivation of the real orthogonality is included because of the self-containment of the dissertation.

3.3.1 Orthogonality relations between basis functions in the cylindrical coordinate system

For these two orthogonality relation, let us define a compact notation for an integral representation of a product of two fields $\mathbf{u} = \mathbf{u}(\mathbf{r})$ and $\mathbf{v} = \mathbf{v}(\mathbf{r})$ over a surface S as

$$[\mathbf{u}, \mathbf{v}]_S = \int_S ds \{ \mathbf{u} \cdot [\mathbf{n} \cdot \boldsymbol{\sigma}(\mathbf{v})] - \mathbf{v} \cdot [\mathbf{n} \cdot \boldsymbol{\sigma}(\mathbf{u})] \}. \quad (3.3.1)$$

A difference between two types of orthogonality relations is that the complex orthogonality relation exploits the complex reciprocity theorem that requires the complex conjugate of a field. Thus, derivations of the complex orthogonality relations and

related properties are more complicated than those of the real orthogonality relations, especially for guided waves which also have non-propagating wave modes. We will deal with these two orthogonality types separately in what follows.

3.3.1.1 Real orthogonality relations

Orthogonality relations for guided wave basis functions defined by real reciprocity theorem in the cylindrical coordinate system can be found in literatures (see, e.g., Achenbach [60]) and thus we will follow the same procedure. The reciprocity theorem states that, for any arbitrary two fields \mathbf{u} and \mathbf{v} in a plate on any arbitrarily shaped closed surface S_t which does not enclose any sources, the following relation is satisfied:

$$[\mathbf{u}, \mathbf{v}]_{S_t} = 0. \quad (3.3.2)$$

Now let us assume that S_t is the surface of a circular cylinder composed of two circular cylindrical surfaces at $r = a$ and $r = b$, and the top and bottom surfaces coinciding with the surfaces of the plate. We first consider a case when $\mathbf{u} = \boldsymbol{\varphi}_n^m$ and $\mathbf{v} = \boldsymbol{\varphi}_v^\mu$ and both of these are the regular basis functions for Lamb type wave modes defined in Eq. (2.3.1). Then, substituting these into (3.3.2) yields [60]

$$Q_{nv}^{m\mu}|_{r=b} - Q_{nv}^{m\mu}|_{r=a} = 0, \quad (3.3.3)$$

where

$$Q_{nv}^{m\mu} = 2\pi r (-1)^m \delta_{m(-\mu)} \{ P_{nv}^R J'_m(k_n r) J_m(k_v r) - P_{vn}^R(z) J_m(k_n r) J'_m(k_v r) \}, \quad (3.3.4)$$

and

$$P_{nv}^R = \int_0^d dz \{ U_n(z) [S_v^1(z)] - [W_v(z)] S_n^3(z) \}. \quad (3.3.5)$$

In the above equation, the term $2\pi r \delta_{m(-\mu)}$ is the result of the integration related to the θ -dependent functions, and $S_n^1(z)$ and $S_n^3(z)$ are defined in Eqs. (2.3.42c) and (2.3.42d).

Now, let us consider a case when $n \neq v$ and $m = \mu$. Then,

$$J_m(k_n r) \neq J_\mu(k_v r), \quad (3.3.6)$$

and the reciprocity theorem in Eq. (3.3.3) is satisfied only if $P_{nv}^R = P_{vn}^R = 0$. Let us consider another case, when $n = v$ and $m = \mu$. Then,

$$J_m(k_n r) = J_\mu(k_v r). \quad (3.3.7)$$

and the reciprocity theorem in Eq. (3.3.3) is satisfied even when P_{nv}^R and P_{vn}^R are not zero. Therefore, P_{nv}^R for the above two cases can be expressed as follows

$$P_{nv}^R = P_n \delta_{nv}, \quad (3.3.8)$$

where

$$P_n = \int_0^d dz \{U_n(z)S_n^1(z) - W_n(z)S_n^3(z)\}. \quad (3.3.9)$$

Equation (3.3.8) is the real orthogonality relation between two Lamb type wave modes.

For SH waves, the above procedure can be similarly applied. Then, P_{nv}^R are defined as

$$P_{nv}^R = - \int_0^l dz \mu_L \{V_n(z)k_v V_v(z)\} \quad (3.3.10)$$

And this can be rewritten as

$$P_{nv} = P_n \delta_{nv}, \quad (3.3.11)$$

where

$$P_n = -k_n \int_0^l dz \mu_L \{V_n(z)V_n(z)\} \quad (3.3.12)$$

In addition, it can be shown that the Lamb waves and SH waves are orthogonal to each other [60]. Therefore, we have the real orthogonality relation for any guided wave modes:

$$P_{nv}^R = P_n \delta_{nv}. \quad (3.3.13)$$

Using the above result, we can derive the real orthogonality relations of the basis functions by evaluating the following integrals over the circular cylindrical surface S_c of arbitrary radius, which will be used in derivation of the properties of the T-matrix:

$$[\varphi_n^m, \varphi_v^\mu]_{S_c}, [\bar{\varphi}_n^m, \bar{\varphi}_v^\mu]_{S_c}, [\varphi_n^m, \bar{\varphi}_v^\mu]_{S_c}, [\bar{\varphi}_n^m, \varphi_v^\mu]_{S_c}. \quad (3.3.14)$$

By using the similar procedure as in Section 3.3.1.1, it can be shown that the first and second integral is always zero:

$$[\varphi_n^m, \varphi_v^\mu]_{S_c} = 0, [\bar{\varphi}_n^m, \bar{\varphi}_v^\mu]_{S_c} = 0. \quad (3.3.15)$$

We consider third integral in Eq. (3.3.14) for two Lamb type wave mode basis functions. Substituting the explicit expressions basis functions into the third integral and using the orthogonality relation in Eq. (3.3.19) gives,

$$[\varphi_n^m, \bar{\varphi}_v^\mu]_{S_c} = 2\pi r (-1)^m \delta_{m(-\mu)} \delta_{nv} P_n [J'_m(k_n r) H_m^{(1)}(k_n r) - J_m(k_n r) H_m^{(1)'}(k_n r)]$$

Then using the Wronskian relation,

$$J'_m(kr) H_m^{(1)}(kr) - J_m(kr) H_m^{(1)'}(kr) = -2i/(\pi kr) \quad (3.3.16)$$

we have the following result:

$$[\varphi_n^m, \bar{\varphi}_v^\mu]_{S_c} = -4i/k_n (-1)^m P_n \delta_{m(-\mu)} \delta_{nv}. \quad (3.3.17)$$

The fourth integral can be obtained by using the similar procedure or it can also be calculated using the result from the third integral,

$$[\bar{\varphi}_n^m, \varphi_v^\mu]_{S_c} = -[\varphi_v^\mu, \bar{\varphi}_n^m]_{S_c} = 4i/k_n (-1)^m P_n \delta_{m(-\mu)} \delta_{nv}. \quad (3.3.18)$$

Therefore, the real orthogonality relations for the basis functions in the cylindrical coordinate system can be summarized as follows:

$$\begin{aligned} [\varphi_n^m, \varphi_v^\mu]_{S_c} &= 0, [\bar{\varphi}_n^m, \bar{\varphi}_v^\mu]_{S_c} = 0, \\ [\varphi_n^m, \bar{\varphi}_v^\mu]_{S_c} &= -4i/k_n (-1)^m P_n \delta_{m(-\mu)} \delta_{nv}, \\ [\bar{\varphi}_n^m, \varphi_v^\mu]_{S_c} &= 4i/k_n (-1)^m P_n \delta_{m(-\mu)} \delta_{nv}. \end{aligned} \quad (3.3.19)$$

3.3.1.2 Complex orthogonality relations

In what follows, the complex orthogonality relations for guided wave basis functions in the cylindrical coordinate system will be derived. Here, we first consider a case when $\mathbf{v} = \varphi_n^m$ and $\mathbf{v} = (\varphi_v^\mu)^*$, and these are two Lamb type wave mode basis functions defined in Eq. (2.3.1). Substituting these into Eq. (3.3.2) and some manipulation yield,

$$[\varphi_n^m, (\varphi_v^\mu)^*]_{S_t} = Q_{nv}^{m\mu} |_{r=b} - Q_{nv}^{m\mu} |_{r=a} = 0. \quad (3.3.20)$$

where

$$Q_{nv}^{m\mu} = 2\pi r \delta_{m\mu} \{ P_{nv}^C J'_m(k_n r) [J_m(k_v r)]^* - P_{vn}^{C*}(z) J_m(k_n r) [J'_m(k_v r)]^* \}, \quad (3.3.21)$$

and

$$P_{nv}^C = \int_0^d dz \{ U_n(z) [S_v^1(z)]^* - [W_v(z)]^* S_n^3(z) \}. \quad (3.3.22)$$

In deriving the complex reciprocity relations, we divide into three cases according to the types of a wavenumber; real, imaginary or complex. Then, unlike the procedure used for deriving the real-reciprocity relations, these cases should be dealt with separately.

We first consider a case when wave mode n and v have a pure real wavenumber k_n and k_v respectively, and assume that $v = n$ ($k_v = k_n$). In this case, we have the following relation:

$$\begin{aligned} [U_v(z)]^* &= U_n(z), [W_v(z)]^* = W_n(z), \\ [S_v^1(z)]^* &= S_n^1(z), [S_v^3(z)]^* = S_n^3(z). \end{aligned} \quad (3.3.23)$$

Therefore, (3.3.21) becomes

$$Q_{nn}^{m\mu} = 2\pi r \delta_{m\mu} P_n [J'_m(k_n r) J_m(k_n r) - J_m(k_n r) J'_m(k_n r)] = 0. \quad (3.3.24)$$

As a consequence, Eq. (3.3.20) is satisfied even though P_{nv}^C and P_{vn}^{C*} in Eq. (3.3.21) are not zero. On the other hand, when $v \neq n$ ($k_v \neq k_n$), Eq. (3.3.20) is satisfied only if $P_{nv}^C = P_{vn}^{C*} = 0$.

Next, we consider a case when wave mode n and ν have an pure imaginary or complex wavenumber k_n and k_ν respectively. We suppose that a wavenumber k_ν of the wave mode ν is

$$k_\nu = \begin{cases} k_n, & \text{for imaginary } k_n, \\ -k_n^*, & \text{for complex } k_n. \end{cases} \quad (3.3.25)$$

For these two wave modes n and ν , the following relations hold:

$$\begin{aligned} [U_\nu(z)]^* &= -U_n(z), [W_\nu(z)]^* = W_n(z), \\ [S_\nu^1(z)]^* &= S_n^1(z), [S_\nu^3(z)]^* = -S_n^3(z), \end{aligned} \quad (3.3.26)$$

under condition that $U_n(z)$ and $W_n(z)$ are consistently normalized to attain above relations. (Note that different negative sign relations can be used too.) An we also need the following properties of Bessel functions:

$$J_m(k_n r) = (-1)^m [J_m(k_\nu r)]^*, J'_m(k_n r) = (-1)^{m+1} [J'_m(k_\nu r)]^*. \quad (3.3.27)$$

Then, substituting Eqs. (3.3.26) and (3.3.27) into (3.3.20) yields

$$Q_{nn}^{m\mu} = 2\pi r (-1)^m \delta_{m\mu} P_n [J'_m(k_n r) J_m(k_n r) - J_m(k_n r) J'_m(k_n r)] = 0. \quad (3.3.28)$$

Consequently, in case when Eq. (3.3.25) holds, nonzero $P_{n\nu}^C$ and $P_{\nu n}^{C*}$ can satisfy Eq. (3.3.21). For cases other than those in Eq. (3.3.25), Eq. (3.3.20) is satisfied only if $P_{n\nu}^C = P_{\nu n}^{C*} = 0$. Therefore, by the above relations, we can conclude that, for both propagating and non-propagating modes of Lamb type waves, the following relation holds:

$$P_{n\nu}^C = P_n \delta_{n_\perp \nu}. \quad (3.3.29)$$

In Eq. (3.3.29), we used the symbol n_\perp to indicate the nonorthogonal mode for a wave mode n which satisfies the following relation:

$$\begin{aligned} k_{n_\perp} &= k_n, \text{ for a real } k_n, \\ k_{n_\perp} &= -k_n^*, \text{ for an imaginary or complex } k_n. \end{aligned}$$

By the definition of P_{nv}^C in Eq. (3.3.22) and the properties in Eqs. (3.3.23) and (3.3.26), we have following relations:

$$P_{vn}^{C*} = \begin{cases} P_n \delta_{n \neq v}, & \text{for real } k_n, \\ -P_n \delta_{n \neq v}, & \text{for imaginary or complex } k_n. \end{cases} \quad (3.3.30)$$

For the complex mode orthogonality relation between SH waves, P_{nv}^C is defined as

$$P_{nv}^C = - \int_0^l dz \mu V_n(z) k_v^* V_v(z). \quad (3.3.31)$$

When $v = n$ (for real or imaginary wavenumber $k_v = k_n$), the following relation holds

$$[V_v(z)]^* = [V_n(z)]. \quad (3.3.32)$$

Thus, by proceeding similarly as in Lamb type wave cases, we have

$$P_{nv}^C = \begin{cases} P_n \delta_{nv}, & \text{for real } k_n, \\ -P_n \delta_{nv}, & \text{for imaginary } k_n. \end{cases} \quad (3.3.33a)$$

and

$$P_{vn}^{C*} = P_n \delta_{nv} \text{ for real or imaginary } k_n. \quad (3.3.33b)$$

It is noted that the Lamb and SH wave modes are orthogonal to each other also by complex-reciprocity theorem.

Now, we will calculate following integrals which will be used for derivation of properties of the T-matrix,

$$[\varphi_n^m, (\varphi_v^\mu)^*]_{S_c}, [\varphi_n^m, (\bar{\varphi}_v^\mu)^*]_{S_c}, [\bar{\varphi}_n^m, (\varphi_v^\mu)^*]_{S_c}, [\bar{\varphi}_n^m, (\bar{\varphi}_v^\mu)^*]_{S_c}. \quad (3.3.34)$$

For example, let us consider the second integral in Eq. (3.3.34) and evaluate this integral similarly as in Eq. (3.3.20). Then, we have

$$[\varphi_n^m, (\bar{\varphi}_v^\mu)^*]_{S_c} = 2\pi r \delta_{m\mu} \{ P_{nv}^C J_m'(k_n r) [H_m^{(1)}(k_v r)]^* - P_{vn}^{C*} J_m(k_n r) [H_m^{(1)'}(k_v r)]^* \}. \quad (3.3.35)$$

For a real wavenumber k_n of a Lamb or SH wave mode n , Hankel functions have the following properties:

$$H_m^{(2)}(k_n r) = [H_m^{(1)}(k_n r)]^*, \quad H_m^{(2)'}(kr) = [H_m^{(1)'}(k_n r)]^*. \quad (3.3.36)$$

Substituting the relation in Eqs. (3.3.29), (3.3.30), (3.3.33a), (3.3.33b), (3.3.36) and the Wronskian relation for Bessel and Hankel functions of second kind

$$J_m'(kr)H_m^{(2)}(kr) - J_m(kr)H_m^{(2)'}(kr) = 2i/(\pi kr), \quad (3.3.37)$$

into Eq. (3.3.35) yields

$$[\varphi_n^m, (\bar{\varphi}_v^\mu)^*]_{S_c} = 4i/k_n P_n \delta_{n\perp v} \delta_{m\mu}. \quad (3.3.38)$$

For an imaginary or a complex wavenumber k_n of a Lamb type wave mode n and a wavenumber $-k_n^*$ of its nonorthogonal mode, the following relation holds for Hankel functions:

$$H_m^{(1)}(k_n r) = (-1)^{m+1} [H_m^{(1)}(-k_n^* r)]^*, \quad H_m^{(1)'}(k_n r) = (-1)^m [H_m^{(1)'}(-k_n^* r)]^*. \quad (3.3.39)$$

Substituting the relation in Eqs. (3.3.29), (3.3.30), (3.3.39) and the Wronskian relation in Eq. (3.3.16) into Eq. (3.3.35) results in

$$[\varphi_n^m, (\bar{\varphi}_v^\mu)^*]_{S_c} = (-1)^m 4i/k_n P_n \delta_{n\perp v} \delta_{m\mu}. \quad (3.3.40)$$

We can proceed similarly for an SH wave mode n having an imaginary wavenumber k_n using Eqs. (3.3.33a), then we have

$$[\varphi_n^m, (\bar{\varphi}_v^\mu)^*]_{S_c} = -(-1)^m 4i/k_n P_n \delta_{nv} \delta_{m\mu}. \quad (3.3.41)$$

To simultaneously treat the results for Lamb type wave modes in Eqs. (3.3.38) and (3.3.40) an SH wave modes in Eq. (3.3.41), we introduce the following expression for wave modes having real, imaginary or complex wavenumber k_n ,

$$[\varphi_n^m, (\bar{\varphi}_v^\mu)^*]_{S_c} = \varepsilon_n^m 4i/k_n P_n \delta_{n\perp v} \delta_{m\mu}, \quad (3.3.42)$$

where

$$\varepsilon_n^m = \begin{cases} 1 & ; \text{ for modes with real } k_n, \\ (-1)^m & ; \text{ for Lamb modes with imaginary or complex } k_n, \\ -(-1)^m & ; \text{ for SH modes with imaginary } k_n. \end{cases}$$

Next the fourth integral in Eq. (3.3.34) is evaluated similarly as before, then we have

$$[\bar{\varphi}_n^m, (\bar{\varphi}_v^\mu)^*]_{S_c} = 2\pi r \delta_{m\mu} \{ P_{nv}^C H_m^{(1)'}(k_n r) [H_m^{(1)}(k_v r)]^* - P_{vn}^{C*} H_m^{(1)}(k_n r) [H_m^{(1)'}(k_v r)]^* \}. \quad (3.3.43)$$

When a Lamb type or SH wave mode n having a real wavenumber k_n is considered, the following Wroskian relation are needed:

$$H_m^{(1)'}(kr) H_m^{(2)}(kr) - H_m^{(1)}(kr) H_m^{(2)'}(kr) = 4i/(\pi kr) \quad (3.3.44)$$

Then, by using Eqs. (3.3.29), (3.3.30), (3.3.33a), (3.3.33b), (3.3.36) and the above Wronskian relation, Eq. (3.3.43) becomes

$$[\bar{\varphi}_n^m, (\bar{\varphi}_v^\mu)^*]_{S_c} = 8i/k_n P_n \delta_{m\mu} \delta_{nv}. \quad (3.3.45)$$

For a Lamb type or SH wave mode n having an imaginary or complex wavenumber k_n , we can proceed as before using Eqs. (3.3.29), (3.3.30), (3.3.33a), (3.3.33b) and (3.3.39), then Eq. (3.3.43) becomes

$$[\bar{\varphi}_n^m, (\bar{\varphi}_v^\mu)^*]_{S_c} = 0. \quad (3.3.46)$$

To integrate two cases in Eqs. (3.3.45) and (3.3.46), we introduce the following expression:

$$[\bar{\varphi}_n^m, (\bar{\varphi}_v^\mu)^*]_{S_c} = \tau_n 8i/k_n P_n \delta_{m\mu} \delta_{nv}. \quad (3.3.47)$$

where $\tau_n = 1$ for a real k_n and $\tau_n = 0$ for a imaginary or complex k_n . Evaluations for the first and third integrals in Eq. (3.3.34) can be done in the similar manner. In summary, we have the complex orthogonality relations for the basis functions as follows:

$$\begin{aligned} [\varphi_n^m, (\varphi_v^\mu)^*]_{S_c} &= 0, \quad [\varphi_n^m, (\bar{\varphi}_v^\mu)^*]_{S_c} = \varepsilon_n^m 4i/k_n P_n \delta_{n\perp v} \delta_{m\mu}, \\ [\bar{\varphi}_n^m, (\varphi_v^\mu)^*]_{S_c} &= \varepsilon_n^m 4i/k_n P_n \delta_{n\perp v} \delta_{m\mu}, \\ [\bar{\varphi}_n^m, (\bar{\varphi}_v^\mu)^*]_{S_c} &= \tau_n 8i/k_n P_n \delta_{m\mu} \delta_{nv}. \end{aligned} \quad (3.3.48)$$

3.3.2 Derivation for three properties of the T matrix

In this subsection, three properties of the T matrix is derived by using the orthogonality relations derived in the preceding subsection. The reciprocity theorem in Eq. (3.3.2) yields two special properties of the T matrix [15]. And the concept of time-reversal invariance yields another property of the T matrix.

3.3.2.1 Reciprocity

Derivation of the first property called the reciprocity of the T matrix starts by considering two arbitrary fields, \mathbf{u} and \mathbf{v} consisting of an incident and scattered field:

$$\begin{aligned} \mathbf{u} &= \mathbf{u}^{\text{inc}} + \mathbf{u}^{\text{sc}} = \sum_{n,m} [A_n^m \varphi_n^m + B_n^m \bar{\varphi}_n^m], \\ \mathbf{v} &= \mathbf{v}^{\text{inc}} + \mathbf{v}^{\text{sc}} = \sum_{v,\mu} [C_v^\mu \varphi_v^\mu + D_v^\mu \bar{\varphi}_v^\mu]. \end{aligned} \quad (3.3.49)$$

We assume that a surface S_t is composed of a scatterer surface S_s and an arbitrary circular cylindrical surface S_c . By applying the boundary conditions on the integrals over S_c , Eq. (3.3.2) becomes

$$[\mathbf{u}, \mathbf{v}]_{S_t} = [\mathbf{u}, \mathbf{v}]_{S_c} = 0, \quad (3.3.50)$$

The reason for vanishing S_c related integrals in the above equation can be explained as follows. When the scatterer is a cavity, it is apparent that the traction-free boundary

condition gives vanishing S_c related integrals. However, when the scatterer is an elastic inclusion, a different explanation is needed. For this, we apply the continuity of the displacement and traction field to $[\mathbf{u}, \mathbf{v}]_{S_c}$, and then we have

$$[\mathbf{u}, \mathbf{v}]_{S_c} = [\mathbf{u}^{\text{tr}}, \mathbf{v}^{\text{tr}}]_{S_c}. \quad (3.3.51)$$

For now, let us assumed that the scatterer has a circular cylindrical shape. In this case, the fields \mathbf{u}^{tr} and \mathbf{v}^{tr} transmitted into the scatterer can be described using the regular basis functions $\varphi_n^m(\mathbf{r})$ of the scatterer region. Then, by Eq. (3.3.19), Eq. (3.3.51) always vanishes. This explanation can be extended to a case when the shape of the scatterer is other than circular cylindrical, because we always can set a virtual circular cylindrical scatterer that encloses the surface S_c . Since the transmitted field on S_c can be expanded in $\varphi_n^m(\mathbf{r})$ of the plate, Eq. (3.3.51) always vanishes by Eq. (3.3.19).

Substituting Eq. (3.3.49) into Eq. (3.3.50) yield

$$\begin{aligned} [\mathbf{u}, \mathbf{v}]_{S_c} = \sum_{n,m} \sum_{\nu,\mu} \{ & A_n^m C_\nu^\mu [\varphi_n^m, \varphi_\nu^\mu]_{S_c} + A_n^m D_\nu^\mu [\varphi_n^m, \bar{\varphi}_\nu^\mu]_{S_c} \\ & + B_n^m C_\nu^\mu [\bar{\varphi}_n^m, \varphi_\nu^\mu]_{S_c} + B_n^m D_\nu^\mu [\bar{\varphi}_n^m, \bar{\varphi}_\nu^\mu]_{S_c} \} = 0. \end{aligned} \quad (3.3.52)$$

Using the real orthogonality relations in Eq. (3.3.19), we have

$$\sum_{n,m} A_n^m D_n^{-m} [(-1)^m P_n/k_n] = \sum_{n,m} B_n^m C_n^{-m} [(-1)^m P_n/k_n]. \quad (3.3.53)$$

According to the definition of the T matrix, the following relation holds between the coefficients of the incident and scattered field:

$$B_n^m = \sum_{\nu,\mu} T_{n,\nu}^{m,\mu} A_\nu^\mu, D_n^m = \sum_{\nu,\mu} T_{n,\nu}^{m,\mu} C_\nu^\mu. \quad (3.3.54)$$

Substituting the above relations into Eq. (3.3.53) results in

$$\sum_{n,m} \sum_{\nu,\mu} A_n^m T_{n,\nu}^{-m,\mu} C_\nu^\mu [(-1)^m P_n/k_n] = \sum_{n,m} \sum_{\nu,\mu} T_{n,\nu}^{m,\mu} A_\nu^\mu C_n^{-m} [(-1)^m P_n/k_n]. \quad (3.3.55)$$

Therefore, the property of the T matrix derived from the real reciprocity theorem is

$$T_{n,\nu}^{-m,-\mu} [(-1)^m P_n/k_n] = T_{\nu,n}^{\mu,m} [(-1)^\mu P_\nu/k_\nu]. \quad (3.3.56)$$

3.3.2.2 Energy conservation

It has been known that the property of the T matrix deduced from the energy conservation law corresponds to that deduced from the complex reciprocity theorem [97]. Therefore, we again consider the complex reciprocity theorem based on Eq. (3.3.2), but this time we take the complex conjugate of the field \mathbf{v} in Eq. (3.3.49). Then, by proceeding similarly as in Section, Eq. (3.3.2) becomes

$$\begin{aligned} [\mathbf{u}, \mathbf{v}^*]_{S_c} = & \sum_{n,m} \sum_{\nu,\mu} \{ A_n^m (C_\nu^\mu)^* [\varphi_n^m, (\varphi_\nu^\mu)^*]_{S_c} + A_n^m (D_\nu^\mu)^* [\varphi_n^m, (\bar{\varphi}_\nu^\mu)^*]_{S_c} \\ & + B_n^m (C_\nu^\mu)^* [\bar{\varphi}_n^m, (\varphi_\nu^\mu)^*]_{S_c} + B_n^m (D_\nu^\mu)^* [\bar{\varphi}_n^m, (\bar{\varphi}_\nu^\mu)^*]_{S_c} \} = 0. \end{aligned} \quad (3.3.57)$$

Substituting Eqs. (3.3.48) into the above equation and performing the summation on ν, μ yield

$$\sum_{n,m} \left[A_n^m (D_{n_\perp}^m)^* \varepsilon_n^m P_n / k_n + B_n^m (C_{n_\perp}^m)^* \varepsilon_n^m P_n / k_n + 2B_n^m (D_n^m)^* \tau_n P_n / k_n \right] = 0. \quad (3.3.58)$$

By applying the definition of the T-matrix as in Eq. (3.3.54), we have

$$\begin{aligned} & \sum_{n,m} \sum_{\nu,\mu} \left[A_n^m (C_\nu^\mu)^* (T_{n_\perp, \nu}^{m,\mu})^* \varepsilon_n^m P_n / k_n + A_n^m (C_\nu^\mu)^* T_{\nu_\perp, n}^{\mu,m} \varepsilon_{\nu_\perp}^\mu P_{\nu_\perp} / k_{\nu_\perp} \right] \\ & = - \sum_{n,m} \sum_{\nu,\mu} \sum_{\eta,\xi} \left[A_n^m (C_\nu^\mu)^* 2T_{\eta,n}^{\xi,m} (T_{\eta,\nu}^{\xi,\mu})^* \kappa_\eta P_\eta / k_\eta \right]. \end{aligned} \quad (3.3.59)$$

The above equation should be satisfied for any arbitrary coefficients for the incident wave field. Therefore, the energy conservation property of T matrix is

$$\begin{aligned} & (T_{n_\perp, \nu}^{m,\mu})^* \varepsilon_n^m P_n / k_n + T_{\nu_\perp, n}^{\mu,m} \varepsilon_{\nu_\perp}^\mu P_{\nu_\perp} / k_{\nu_\perp} \\ & = -2 \sum_{\eta,\xi} \left[(T_{\eta,\nu}^{\xi,\mu})^* T_{\eta,n}^{\xi,m} \kappa_\eta P_\eta / k_\eta \right]. \end{aligned} \quad (3.3.60)$$

3.3.2.3 Time-reversal invariance

The time-reversal invariance stands for the fact that time-reversed fields can be represented by the same equations that govern forward fields. This indicates that a property

of the T matrix resulted from the time-reversal invariance can be derived by using the fact that a time-reversed field \mathbf{u}^* can also be expressed in terms of the basis functions $\varphi_n^m(\mathbf{r})$ and $\bar{\varphi}_n^m(\mathbf{r})$. In other words, this derivation is equivalent to a problem that looks for \mathbf{v}^{TR} satisfying the following relation:

$$\mathbf{u}^* = \mathbf{v}^{\text{TR}}, \quad (3.3.61a)$$

where

$$\mathbf{u}^* = (A_n^m)^*(\varphi_n^m)^* + (B_n^m)^*(\bar{\varphi}_n^m)^*, \quad (3.3.61b)$$

$$\mathbf{v}^{\text{TR}} = (C_n^m)^{\text{TR}}\varphi_n^m + (D_n^m)^{\text{TR}}\bar{\varphi}_n^m. \quad (3.3.61c)$$

It seems that directly comparing both side of Eq. (3.3.61a) does not give an answer to this problem. It is because when the time-reversal (the complex conjugate) of the basis functions are taken, its physical interpretation becomes ambiguous. In case of bulk waves which do not involve nonpropagating waves, this ambiguity can be avoided by splitting a standing wave represented by the regular basis functions φ_n^m into an incoming wave and outgoing wave. Then, it is apparent that the time-reversal of an incoming wave becomes an outgoing wave and vice versa. However, when non-propagating modes which has an imaginary or complex wavenumber are involved, it is hard to split a standing wave into an incoming wave and outgoing wave. Therefore, a different approach is needed to tackle this problem.

One way is to use the real and complex orthogonality relations of the basis functions in Eqs. (3.3.19) and (3.3.48). Since we have two unknown coefficients ($(C_n^m)^{\text{TR}}$, $(D_n^m)^{\text{TR}}$), we consider the following two equations:

$$[\varphi_{n'}^{m'}, \mathbf{v}^{\text{TR}}]_{S_T} = [\varphi_{n'}^{m'}, \mathbf{u}^*]_{S_T}, \quad (3.3.62a)$$

$$[\bar{\varphi}_{n'}^{m'}, \mathbf{v}^{\text{TR}}]_{S_T} = [\bar{\varphi}_{n'}^{m'}, \mathbf{u}^*]_{S_T}, \quad (3.3.62b)$$

Substituting Eq. (3.3.19) into the LHS in Eqs. (3.3.62a) and (3.3.62b) yields

$$\begin{aligned} [\varphi_{n'}^{m'}, \mathbf{v}^{\text{TR}}]_{S_T} &= \sum_{n,m} \{ (C_n^m)^{\text{TR}} [\varphi_{n'}^{m'}, \varphi_n^m] + (D_n^m)^{\text{TR}} [\varphi_{n'}^{m'}, \bar{\varphi}_n^m] \} \\ &= -(D_{n'}^{-m'})^{\text{TR}} 4i/k_{n'} (-1)^{m'} P_{n'}, \end{aligned} \quad (3.3.63)$$

$$\begin{aligned} [\bar{\varphi}_{n'}^{m'}, \mathbf{v}^{\text{TR}}]_{S_T} &= \sum_{n,m} \{ (C_n^m)^{\text{TR}} [\bar{\varphi}_{n'}^{m'}, \varphi_n^m] + (D_n^m)^{\text{TR}} [\bar{\varphi}_{n'}^{m'}, \bar{\varphi}_n^m] \} \\ &= (C_{n'}^{-m'})^{\text{TR}} 4i/k_{n'} (-1)^{m'} P_{n'}. \end{aligned} \quad (3.3.64)$$

Substituting Eq. (3.3.48) into the RHS in Eqs. (3.3.62a) and (3.3.62b) yields

$$\begin{aligned} [\varphi_{n'}^{m'}, \mathbf{u}^*]_{S_T} &= \sum_{n,m} \{ (A_n^m)^* [\varphi_{n'}^{m'}, (\varphi_n^m)^*] + (B_n^m)^* [\varphi_{n'}^{m'}, (\bar{\varphi}_n^m)^*] \} \\ &= (B_{n'}^{m'})^* \varepsilon_{n'}^{m'} 4i/k_{n'} P_{n'}, \end{aligned} \quad (3.3.65)$$

$$\begin{aligned} [\bar{\varphi}_{n'}^{m'}, \mathbf{u}^*]_{S_T} &= \sum_{n,m} \{ (A_n^m)^* [\bar{\varphi}_{n'}^{m'}, (\varphi_n^m)^*] + (B_n^m)^* [\bar{\varphi}_{n'}^{m'}, (\bar{\varphi}_n^m)^*] \} \\ &= (A_{n'}^{m'})^* \varepsilon_{n'}^{m'} 4i/k_{n'} P_{n'} + (B_{n'}^{m'})^* \kappa_{n'} 8i/k_{n'} P_{n'}. \end{aligned} \quad (3.3.66)$$

Then, by substituting Eqs. (3.3.63) and (3.3.65) into Eq. (3.3.62a), we get

$$-(D_{n'}^{-m'})^{\text{TR}} (-1)^{m'} = (B_{n'}^{m'})^* \varepsilon_{n'}^{m'}. \quad (3.3.67)$$

In the same way, substituting Eqs. (3.3.64) and (3.3.66) into Eq. (3.3.62b) gives

$$(C_{n'}^{-m'})^{\text{TR}} (-1)^{m'} = (A_{n'}^{m'})^* \varepsilon_{n'}^{m'} + (B_{n'}^{m'})^* \kappa_{n'}. \quad (3.3.68)$$

Now, having obtained $((C_n^m)^{\text{TR}}, (D_n^m)^{\text{TR}})$ in terms of (A_n^m, B_n^m) , we can derive a properties of the T matrix using the definition of the T matrix. Thus, we substitute Eq. (3.3.54) into Eq. (3.3.67):

$$-\sum_{\nu,\mu} T_{n',\nu}^{-m',\mu} (C_\nu^\mu)^{\text{TR}} (-1)^{m'} = \sum_{\nu,\mu} (T_{n',\nu}^{m',\mu})^* (A_\nu^\mu)^* \varepsilon_{n'}^{m'}. \quad (3.3.69)$$

Similarly, Eq. (3.3.68) becomes

$$(C_V^\mu)^{\text{TR}} = (-1)^\mu [(A_{V_\perp}^{-\mu})^* \boldsymbol{\varepsilon}_V^{-\mu} + 2 \sum_{\eta, \xi} (T_{V, \eta}^{-\mu, \xi})^* (A_\eta^\xi)^* \boldsymbol{\kappa}_V]. \quad (3.3.70)$$

Then, eliminating $(C_V^\mu)^{\text{TR}}$ in Eqs. (3.3.69) and (3.3.70) results in

$$\begin{aligned} & - \sum_{v, \mu} T_{n', v}^{-m', \mu} (-1)^\mu [(A_{V_\perp}^{-\mu})^* \boldsymbol{\varepsilon}_V^{-\mu} + 2 \sum_{\eta, \xi} (T_{v, \eta}^{-\mu, \xi})^* (A_\eta^\xi)^* \boldsymbol{\kappa}_V] (-1)^{m'} \\ & = \sum_{v, \mu} (T_{n', v}^{m', \mu})^* (A_V^\mu)^* \boldsymbol{\varepsilon}_{n'}^{m'}. \end{aligned} \quad (3.3.71)$$

This can be rewritten as follows:

$$\begin{aligned} & - 2 \sum_{v, \mu} \sum_{\eta, \xi} T_{n', \eta}^{-m', -\xi} (-1)^{\xi+m'} (T_{\eta, v}^{\xi, \mu})^* (A_V^\mu)^* \boldsymbol{\kappa}_\eta \\ & = \sum_{v, \mu} T_{n', v_\perp}^{-m', -\mu} (-1)^{\mu+m'} (A_V^\mu)^* \boldsymbol{\varepsilon}_{v_\perp}^\mu + \sum_{v, \mu} (T_{n', v}^{m', \mu})^* (A_V^\mu)^* \boldsymbol{\varepsilon}_{n'}^{m'}. \end{aligned} \quad (3.3.72)$$

The above equation should be available for any A_V^μ and therefore we have the time-reversal invariance property of the T matrix in the following form:

$$\begin{aligned} & T_{n', v_\perp}^{-m', -\mu} (-1)^{\mu+m'} \boldsymbol{\varepsilon}_{v_\perp}^\mu + (T_{n', v}^{m', \mu})^* \boldsymbol{\varepsilon}_{n'}^{m'} \\ & = -2 \sum_{\eta, \xi} T_{n', \eta}^{-m', -\xi} (-1)^{\xi+m'} (T_{\eta, v}^{\xi, \mu})^* (A_V^\mu)^* \boldsymbol{\kappa}_\eta. \end{aligned} \quad (3.3.73)$$

It can be check that the above property is equivalent to the simultaneous application of the reciprocity property in Eq. (3.3.56) and the energy conservation property in Eq. (3.3.60) [97].

3.3.3 Summary

The three T-matrix properties are summarized as follows,

· Reciprocity:

$$T_{n, v}^{-m, -\mu} (-1)^m P_n / k_n = T_{v, n}^{\mu, m} (-1)^\mu P_v / k_v, \quad (3.3.74)$$

· Energy conservation:

$$\begin{aligned} (T_{n_\perp, v}^{m, \mu})^* \epsilon_n^m P_n / k_n + T_{v_\perp, n}^{\mu, m} \epsilon_{v_\perp}^\mu P_{v_\perp} / k_{v_\perp} \\ = -2 \sum_{\eta, \xi} \left[(T_{\eta, v}^{\xi, \mu})^* T_{\eta, n}^{\xi, m} \kappa_\eta P_\eta / k_\eta \right], \end{aligned} \quad (3.3.75)$$

where the nonorthogonal mode n_\perp to mode n satisfy the following relation between wavenumbers:

$$k_{n_\perp} = \begin{cases} k_n; & \text{for modes with a real or imaginary } k_n, \\ -k_n^*; & \text{for a complex } k_n, \end{cases}$$

We also have the definitions

$$\epsilon_n^m = \begin{cases} 1; & \text{for modes with real } k_n, \\ (-1)^m; & \text{for Lamb modes with imaginary or complex } k_n, \\ -(-1)^m; & \text{for SH modes with imaginary } k_n, \end{cases}$$

and

$$\tau_n = \begin{cases} 1; & \text{for propagating modes,} \\ 0; & \text{for non-propagating modes.} \end{cases}$$

· Time-reversal invariance:

$$\begin{aligned} T_{n', v_\perp}^{-m', -\mu} (-1)^{\mu+m'} \epsilon_{v_\perp}^\mu + (T_{n', v}^{m', \mu})^* \epsilon_{n'}^{m'} \\ = -2 \sum_{\eta, \xi} T_{n', \eta}^{-m', -\xi} (-1)^{\xi+m'} (T_{\eta, v}^{\xi, \mu})^* (A_v^\mu)^* \kappa_\eta. \end{aligned} \quad (3.3.76)$$

It is noted from the above equations that the reciprocity properties of the T matrix for guided waves is same with that for the bulk waves while the energy conservation and time-reversal invariance properties of the T matrix for guided waves differ from those for bulk waves because of the presence of nonpropagating modes.

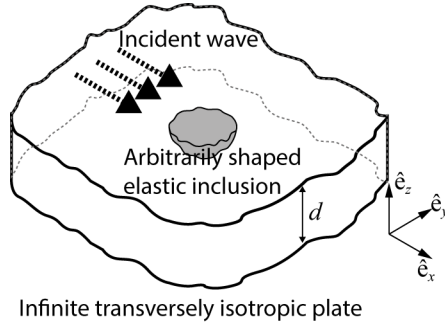


Figure 3.9 Guided wave scattering in an infinite transversely isotropic plate of thickness d with the coordinate system.

3.4 Decomposition method for elastic inclusions using multiple scattering theory

3.4.1 Overall description of the decomposition method

Although, we have obtained the T matrix solutions for a single or multiple scatterers in the previous sections, the previously extended boundary condition method (EBCM) is numerically not versatile when various sizes and shapes of scatterers are concerned. Specifically, when the EBCM is directly applied to scatterers with aspect ratios > 4 in the horizontal plane of a plate, with a varying thickness, or with a radial size $> \lambda_{\min}/2$ (where λ_{\min} is the minimum wavelength), numerical problems such as matrix ill-conditioning occur when solving the linear system of equations. Therefore, to be applicable to a scatterer with a wide range of shapes and sizes, an analysis technique different from that used in the previous works should be developed.

Here, we specifically deal with scattering of guided waves in a flat transversely isotropic plate by an arbitrarily shaped elastic inclusion as in Fig. 3.9. We will use the semi-analytic solution (the T matrix) based on the three-dimensional elasticity described in Section 3.1.2. To develop a method that can be applicable to inclusions with

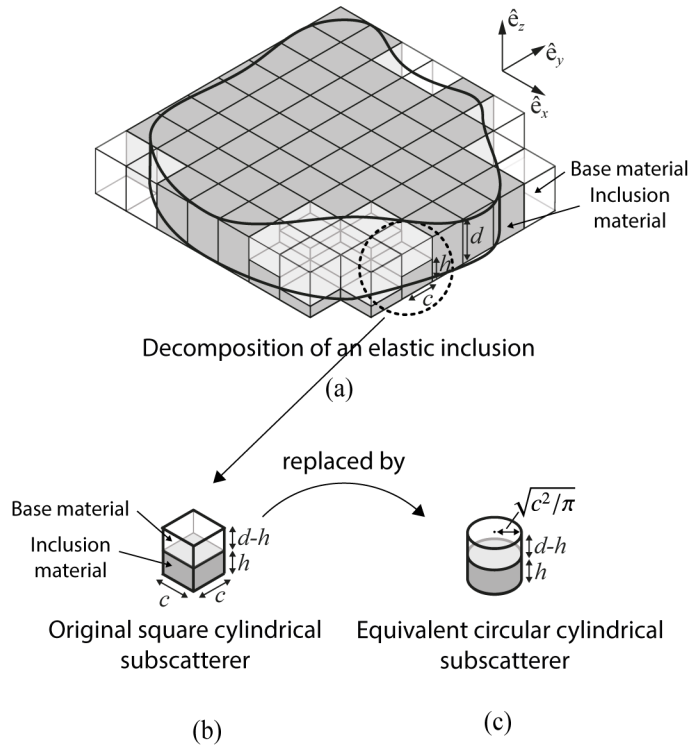


Figure 3.10 (a) Decomposition of a scatterer into a finite number of subscatterers in the horizontal plane using the staircase approximation, (b) stacking a elastic inclusion material with a base (plate) material for the use of the EBCM, and (c) use of an equivalent circular cylindrical subscatterer for efficient T matrix calculation.

a wide range of shapes and sizes that cannot be treated by the aforementioned methods based on the three-dimensional elasticity, we propose a method that decomposes an inclusion into a number of small subscatterers using the staircase approximation, as illustrated in Fig. 3.10(a), and applies a multiple scattering theory (MST) to take the interaction of subscatterers into account and obtain the scattered wave. In this method, the transition matrix (T matrix) that relates the incident and the scattered wave coefficients of each subscatterer is calculated and used in a MST. Although this decom-

position method for scattering analysis has been studied for bulk electromagnetic and acoustic wave problems [19]–[21], [24], there have been no reports related to elastic guided wave scattering problems. Especially because nonpropagating waves that only occur in guided wave problems should be considered in addition to propagating waves in this study, a proper analysis procedure is required.

In the proposed method, the inclusion is decomposed on the horizontal plane (x - y plane in Fig. 3.10(a)) into subscatterers that are relatively small compared to the minimum wavelength of the propagating modes and then the T matrix for each subscatterer is calculated by using the extended boundary condition method [56]. The inclusion is first decomposed into square cylindrical subscatterers, but calculating the T matrix for each square cylindrical subscatterer requires computationally intensive numerical integration. Therefore, equivalent circular cylindrical subscatterers with the same height and volume are substituted for the square cylindrical subscatterers for efficient calculation of the T matrices. Although this kind of approach is expected to be valid when the size of the subscatterer is very small compared to the wavelengths, it has been tested only for acoustic or electromagnetic problems [19]–[21], and thus its validity should be numerically tested for elastic guided wave problems where nonpropagating modes also exist.

When a multiple scattering analysis is conducted after decomposing an inclusion into multiple closely packed subscatterers, the near-field interaction between subscatterers is important. Because the scattered guided wave from a subscatterer includes nonpropagating modes as well as propagating modes, nonpropagating modes must be also considered for the analysis to yield correct results in a near-field interaction problem whereas in a far-field interaction problem only propagating modes are crucial. The effects of nonpropagating modes on the interaction between scatterers have not been tested in bulk wave problems [19], [20] or in seismic wave problems [98], because nonpropagating modes are either non-existent or omitted in these works. Therefore,

nonpropagating modes, which the T matrix should include for a correct description of the near-field interaction, need to be investigated to identify their effects when using the suggested method. Moreover, for decomposition of an elastic inclusion, the relative size of subscatterers compared to the wavelengths should be investigated owing to the existence of nonpropagating modes. Based on these investigation, the T matrix for each subscatterer is calculated and then the scattered field of the decomposed inclusion can be obtained by applying a MST to the T matrices.

Although, so far, the suggested methods are available specifically for an elastic inclusions based on the three-dimensional elasticity, it is expected and also important that this method will be generalized to traction-free scatterers (cavities) or also to methods based on an approximate plate theory in the future studies.

More details related to implementation of the proposed method will be described in the following subsections.

3.4.2 Details related to implementation

3.4.2.1 Calculation of the basis functions and wavenumbers

In the proposed method, an elastic inclusion is first decomposed by using the staircase approximation in the horizontal plane into multiple small square cylindrical subscatterers, as illustrated in Fig. 3.10(a), and the T matrix for each subscatterer is calculated with the EBCM using Eq. (3.1.17). The calculation of the T matrix requires the displacement and stress basis functions defined by Eqs. (2.3.1), (2.3.2), (2.3.3) and (2.3.4) for the plate and the inclusion. If the height h of the inclusion at a specific scatterer location is smaller than the plate thickness d , the square cylindrical subscatterer is assumed to be made of two material, the inclusion material of thickness h and the base (plate) material of thickness $d - h$ as illustrated in Fig. 3.10(b).

The procedure for computation of the basis functions is described in Section 2.3.2.

By using the pseudo-spectral collocation method with the Chebyshev-Gauss-Lobatto quadrature nodes, the calculated values of $U_n(z)$, $W_n(z)$, and $V_n(z)$ and the Clenshaw-Curtis quadrature weights on the Chebyshev-Gauss-Lobatto quadrature nodes can be used directly to integrate the z -dependent functions appearing in the calculation of $\bar{Q}_{n,v}^{m,\mu}$ and $Q_{n,v}^{m,\mu}$ in Eqs. (3.1.15). This is particularly more useful, when multiple scatterers with various thickness h in Fig. 3.10(b) should be dealt with. When the nodes for the plate region and the subscatterer region coincide, this quadrature rule can be directly applied to the nodal values of the plate and subscatterer region obtained from solving eigenvalue problem described in Section 2.3.2.

3.4.2.2 Behavior of a single small subscatterer

Having obtained the basis functions, we can now obtain the T matrix for each subscatterer. However, if the T matrix for the square cylindrical subscatterer as in Fig. 3.10(b) is directly computed, almost every element of the matrices \mathbf{Q}_j and $\bar{\mathbf{Q}}_j$ for $j = 1, 2$ in Eqs. (3.1.15) are nonzero and the calculation of each element requires thousands of Bessel functions to be computed for numerical integration of the θ -dependent functions. Because the required computations are too intensive, we instead substitute the square cylindrical subscatterer with an equivalent circular cylindrical subscatterer with the same height and volume as suggested in Fig. 3.10(c). This approach was used in electromagnetic bulk wave problems [19]. When using the equivalent circular cylindrical scatterer, only $(Q_j)_{n,v}^{m,\mu}$ and $(\bar{Q}_j)_{n,v}^{m,\mu}$ in Eqs. (3.1.15), corresponding to $m = \mu$, are nonzero and, even for these nonzero elements, the numerical integration of θ -dependent functions can be replaced by an analytic integration. Therefore, calculating the T matrix for the equivalent circular cylindrical subscatterer is very efficient when compared to that for the square cylindrical subscatterer.

The approximation for the equivalence between the square cylindrical subscatterer and the equivalent circular cylindrical subscatterer is expected to be valid because,

when a scatterer is relatively small compared to the wavelengths, the subscatterer can be treated as the line source along the thickness direction in guided wave problems, while in bulk wave problems a small scatterer can be treated as a point source [19]. In other words, the scattered field from a small scatterer is not affected by the specific shape of the scatterer but only by the scattering strength related to the volume of the scatterer. Moreover, as the size of the scatterer becomes small, there are dominant multipolar order terms of the T matrix while other terms are almost insignificant in describing the wave behavior by the scatterer. Therefore, the overall computation time for the scattering analysis can be kept to a minimum, by including only these terms in the T matrix. This equivalence assumption is valid only for a small scatterer; however, it is hard to define a small subscatterer in terms of wavelengths in the current problem because nonpropagating modes of guided waves should also be considered. This means that in guided wave problems it is hard to define a small subscatterer in terms of wavelengths because wavenumbers of nonpropagating modes are purely imaginary or complex; defining wavelength of these nonpropagating waves is somewhat ambiguous. Therefore, this approximation should be validated before we describe the next procedure.

As a means to validate the approximation, we choose a simple example, calculate the near-scattered fields from a single square cylindrical subscatterer and a circular cylindrical subscatterer and compare the results with regard to the different values of the the maximum multipolar order M used in the T matrix computation. In this example, the scattered fields from the original and equivalent subscatterer, made of silicon with a shape defined by $c = \lambda_{A0}/12$ and $h = l/2$ in Figs. 3.10(b) and (c), in an aluminum plate are calculated by using Eq. (3.1.17) and observed at the distance $r = \lambda_{A0}/2$ on the top surface of the plate. Twelve guided wave modes $N = 12$ according to the investigation in 3.4.3.2 were used in the T matrix. (The material properties of the scatterer and the plate are defined in the first paragraph of Section 3.4.3; the inci-

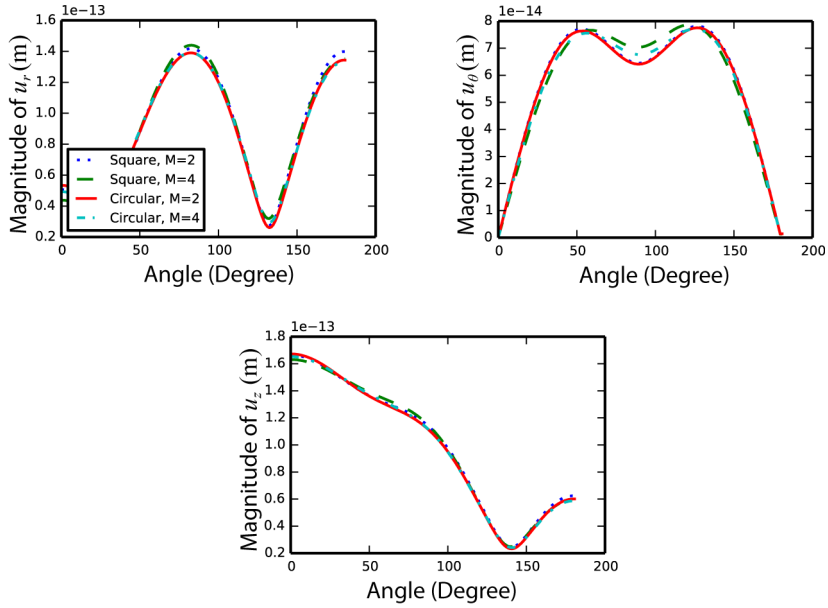


Figure 3.11 Near-scattered fields from the original square cylindrical scatterer and its equivalent circular cylindrical scatterer with its shape defined by $c = \lambda_{A0}/12$ and $h = d/2$ in Fig. 3.10(b) when an aluminum plate and a silicon inclusion are considered. The incident wave is actuated by line tractions as illustrated in Fig. 3.12 with $a_{\text{ext}} = \lambda_{A0}/2$, $r_{\text{ext}} = \lambda_{A0}$ and $t_{\text{ext}} = 1$ N/m at frequency-thickness = 1 MHz-mm. The scattered fields are calculated using the EBCM with $N = 12$ and observed at $r = \lambda_{A0}/6$ from the center of the scatterer.

dent field is actuated from the same configuration described in the second paragraph of Section 3.4.3 except that we used $r_{\text{ext}} = \lambda_{A0}$ in this example to include the contribution of nonpropagating modes in the incident field.) The result in Fig. 3.11 shows that the converged scattered field from the square subscatterer obtained by using $M = 4$ is similar (with minor deviation) to that from the equivalent circular cylindrical subscatterer obtained by using $M = 2$. Although not shown here, the same amount of similarity and deviation is also observed for the far-scattered field. Therefore, we can conclude

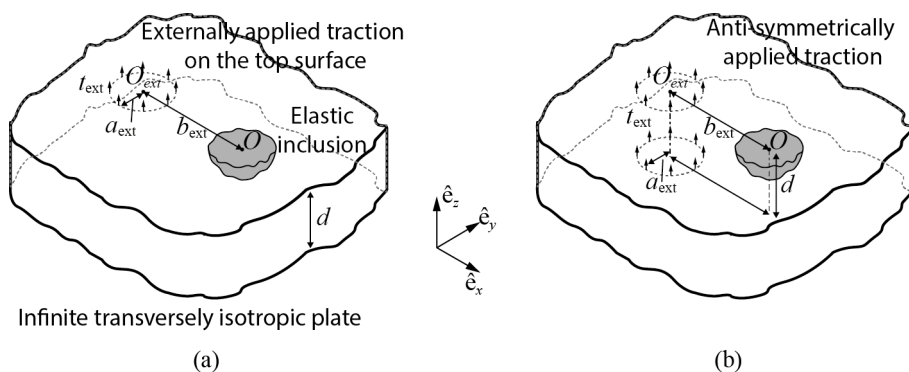


Figure 3.12 Configuration for an incident wave generation. (a) Simultaneous actuation of symmetric and antisymmetric Lamb modes by a line traction on the top surface of the plate. (b) Antisymmetric Lamb mode wave actuation by line tractions on the top and bottom surfaces of the plate used in the numerical examples.

that, even with nonpropagating modes in the T matrix, a circular cylindrical subscatterer with $M = 2$ behaves similarly to a square cylindrical subscatterer with $M = 4$. However, it still cannot be determined whether or not, with multiple subscatterer interaction, significant error caused by accumulation of this minor deviation is observed.

3.4.3 Numerical examples

Numerical examples were solved by using double-precision (16 decimal digits) arithmetics in the NumPy package of the Python programming language [74]. The results obtained by using the suggested method are compared with those obtained by using the finite element method. For the finite element method, the commercially available software COMSOL Multiphysics Structural Mechanics Module was used [99]; see Appendix A for the detailed explanation.

Mechanical properties used in the examples are as follows. For aluminum, Young's modulus = 70 GPa, Poisson's ratio = 0.33, mass density = 2700 kg/m³. For zirconia, Young's modulus = 151 GPa, Poisson's ratio = 0.33, mass density = 3000 kg/m³. For

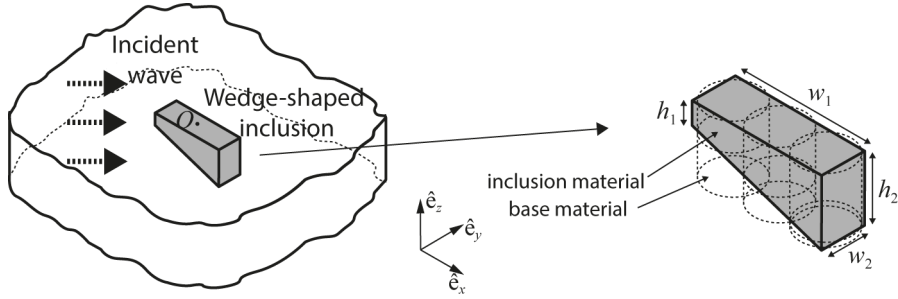


Figure 3.13 A wedge-shaped inclusion in a plate and its decomposition into multiple circular cylindrical subscatterers.

silicon, Young's modulus 131 GPa, Poisson's ratio 0.27, mass density = 2330 kg/m³.

In all problems, the incident fields are actuated by externally applied line tractions as illustrated in Figs. 3.12(a) and 3.12(b). In the first configuration illustrated in Fig. 3.12(a), a circular line traction of radius $a_{\text{ext}} = \lambda_{A0}/2$ are centered at $r_{\text{ext}} = 5\lambda_{A0}$ on the negative x axis and placed on the top surface of the plate; here, the uniform magnitude $t_{\text{ext}} = 1$ N/m of traction is imposed on the circle. In the second configuration illustrated Fig. 3.12(b), two circular line tractions directing in the same direction along the z axis are placed on the top and bottom surfaces of the plate for generation of an anti-symmetric wave mode. For these configuration, the coefficient vector of the incident field needed in the suggested method can be calculated by using Eqs. (2.4.3) and (3.2.5). Note that, because the resulting field and inclusions are chosen to be symmetric with respect to the x axis, the results are also symmetric and therefore plotted up to 180°.

3.4.3.1 Wedge-shaped scatterer

Here, we consider a wedge-shaped inclusion as show in Fig. 3.13 to investigate the appropriate size of a subscatterer for the suggested method. A frequency·thickness of 1 MHz·mm and shape parameters $w_1 = \lambda_{A0}$ ($\lambda_{A0}/d = 2.326$), $w_2 = \lambda_{A0}/4$, $h_1 = 0$,

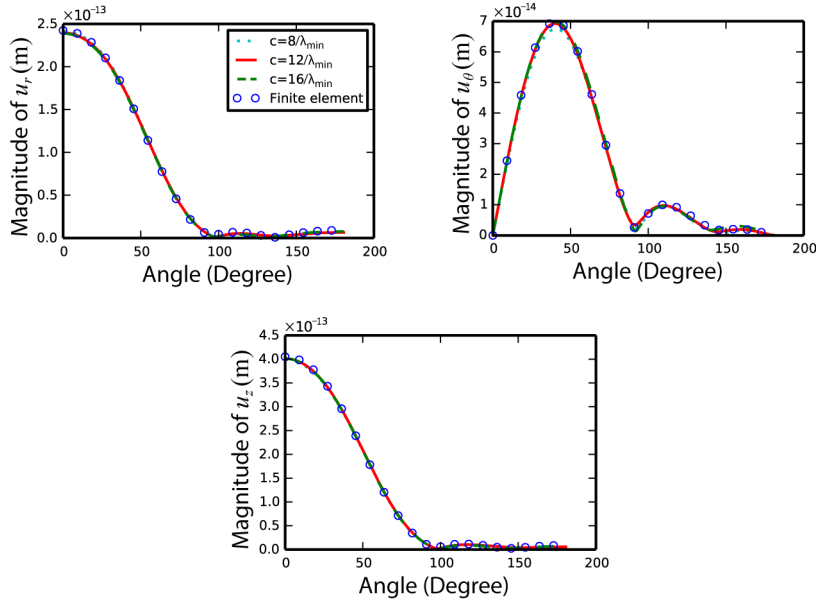


Figure 3.14 Scattered fields from a wedge-shaped silicon inclusion in an aluminum plate as in Fig. 3.13. The results with different values of subscatterer size c defined in Fig. 3.10 are compared. The relative values of c compared to the smallest wavelength λ_{\min} (λ_{A0} in this problem) are used. The shape of the wedge is defined by parameters $w_1 = \lambda_{A0}$, $w_2 = \lambda_{A0}/4$, $h_1 = 0$, and $h_2 = d$. The incident wave is actuated by line tractions as illustrated in Fig. 3.12(b) with $a_{\text{ext}} = \lambda_{A0}/2$, $r_{\text{ext}} = 5\lambda_{A0}$ and $t_{\text{ext}} = 1 \text{ N/m}$ at frequency \cdot thickness = 1 MHz \cdot mm. The scattered fields are observed at $r = 10\lambda_{A0}$ from the center of the scatterer on the top surface of the plate. For the suggested method, $N = 12$ guided wave modes are used.

and $h_2 = d$ were used in the example. The shape of this kind of inclusion cannot be dealt with by modifying the existing method for dealing with scattering by cavities [44], [45]. Since h defined in Fig. 3.10(b) of the inclusion varies in subscatterers, the staircase approximation along the z axis needs to be applied. In this case, discretization over the thickness direction ($0 \leq z \leq d$) is made in calculating the basis functions. In

Table 3.1 Lamination types of plates and scatterers made of Mat 1 and Mat 2, I: isotropic, SL: symmetrically layered, NL: non-symmetrically layered.

Abbreviation	I	SL	NL
Plate	Mat 1	Mat 1	Mat 1
		Mat 2	Mat 2
		Mat 1	Mat 2
Scatterer	Mat 2	Mat 2	Mat 2
		Mat 1	Mat 1
		Mat 2	Mat 1

this works, we used 20 discretizations. In Fig. 3.14, several results are plotted with regard to the relative size c of the subscatterer defined in Fig. 3.10 when compared to λ_{\min} (λ_{A0} in this problem). Thus, we can conclude that $c = \lambda_{A0}/8 \sim \lambda_{A0}/16$ can be used for the size of the subscatterer and also that treating the arbitrary shape along the z axis with the staircase approximation in the suggested method is useful. Since there is very little difference in results as long as the subscatterer size c is in this range, we will use $c = \lambda_{A0}/12$ in the following examples unless otherwise stated.

3.4.3.2 Number of guided wave modes to achieve convergence

As we stated above, near-field interactions can be correctly expressed only when not only the propagating but also the nonpropagating modes are included in forming the T matrix. However, use of many nonpropagating modes is not only efficient but also can cause numerical error in some cases. In this context, we investigate and discuss the number of guided wave modes, N (where N_{Lamb} and N_{SH} are, respectively, the number of Lamb-type wave modes and the number of SH wave modes), for obtaining a converged solution is investigated for different lamination types of plates and scatterers. The lamination types of plates and scatterers used in this investigation are categorized and tabulated in Table 3.1. In Table 3.1, Mat 1 and Mat 2 denote aluminum and silicon, respectively.

In Table 3.2, the results of this investigation are summarized according to the

Table 3.2 The number of guided wave mode expansion terms, N ($N_{\text{Lamb}}, N_{\text{SH}}$), needed to obtain a converged solution. S: symmetric guided wave, A: antisymmetric guided wave, C: nonsymmetric or coupled guided wave; I: isotropic, SL: symmetrically layered, NL: non-symmetrically layered.

Case	Type			Frequency · thickness (MHz · mm)			
	Plate	Scatterer	Wave	0.05	0.5	1	1.5
1-1	I	I	S	2 (1,1)	2 (1,1)	4 (3,1)	6 (3,3)
1-2	I	I	A	4 (2,2)	4 (2,2)	4 (2,2)	7 (4,3)
1-3	I	NL	C	8 (5,3)	8 (5,3)	12 (7,5)	15 (9,6)
2-1	SL	I	S	2 (1,1)	5 (3,2)	6 (3,3)	8 (5,3)
2-2	SL	I	A	6 (4,2)	6 (4,2)	8 (6,2)	8 (6,2)
2-3	SL	NL	C	11 (7,4)	24 (17,7)	26 (19,7)	26 (19,7)
3-1	NL	I	C	6 (3,3)	12 (7,5)	12 (7,5)	14 (9,5)
3-2	NL	NL	C	14 (9,5)	16 (9,7)	24 (17,7)	24 (17,7)

frequency-thickness values. For example, in case 1-3 of Table 3.2, the wedge-shaped silicon inclusion in an aluminum plate is considered as in Fig. 3.13. In this case, the plate is isotropic (expressed as I in Table 3.1) and the subscatterers of the inclusion should be treated as nonsymmetric layers (expressed as NL in Table 3.1) with respect to the horizontal midplane of the plate for the T matrix calculation by using the EBCM. Then, the number of guided wave modes, N , in the suggested method is increased until the scattering solution is converged as in Figure 3.15. Other cases are handled similarly with different values of w_1 , w_2 , h_1 , and h_2 defined in Fig. 3.13.

As shown in Table 3.2, the low number N from cases 1-1, 1-2, 2-1, and 2-2 is due to the decoupling of symmetric and antisymmetric guided wave modes and, as the laminations of the plate and the scatterer become complex as in cases 2-3 and 3-2, more terms are needed for convergence of the solution. The results in Table 3.2 could

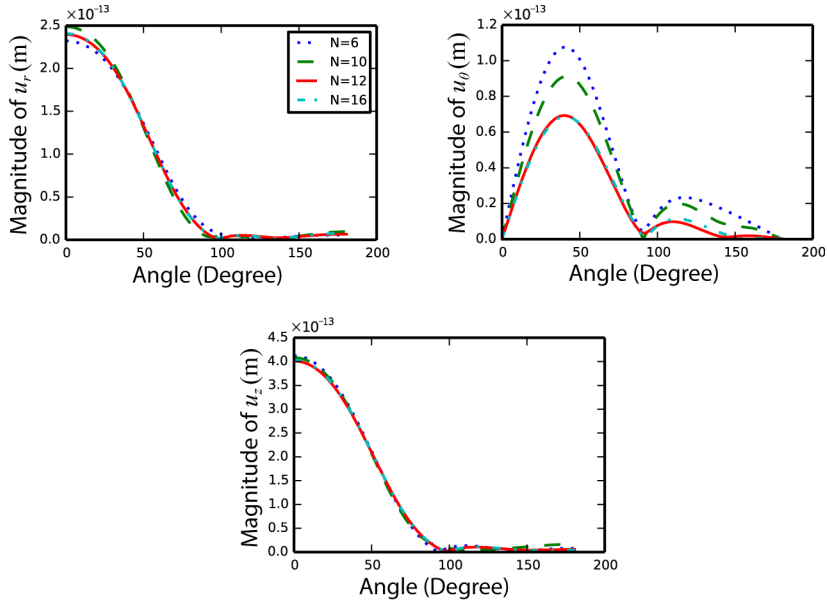


Figure 3.15 The scattered fields from a wedge-shaped silicon inclusion in an aluminum plate as in Fig. 3.13. The results with different numbers of guided wave modes, N , used in the suggested method are compared. The shape of the wedge is defined by parameters $w_1 = \lambda_{A0}$, $w_2 = \lambda_{A0}/4$, $h_1 = 0$, and $h_2 = d$. The incident wave is actuated by line tractions as illustrated in Fig. 3.12(b) with $a_{\text{ext}} = \lambda_{A0}/2$, $r_{\text{ext}} = 5\lambda_{A0}$ and $t_{\text{ext}} = 1$ N/m at frequency-thickness = 1 MHz-mm. The scattered fields are observed at $r = 10\lambda_{A0}$ from the center of the scatterer on the top surface of the plate.

change depending on the properties of the plate and the scatterer but remain similar for materials with properties of the same order of magnitude.

3.4.3.3 Comparison with other solutions for a circular cylindrical inclusion

In this subsection, we compare the result obtained from the proposed method with those from other analytic methods. An aluminum plate of $d = 1$ mm thickness embedded with a circular cylindrical inclusion of $a = 4d$ as shown in Fig. 3.16(a) are con-

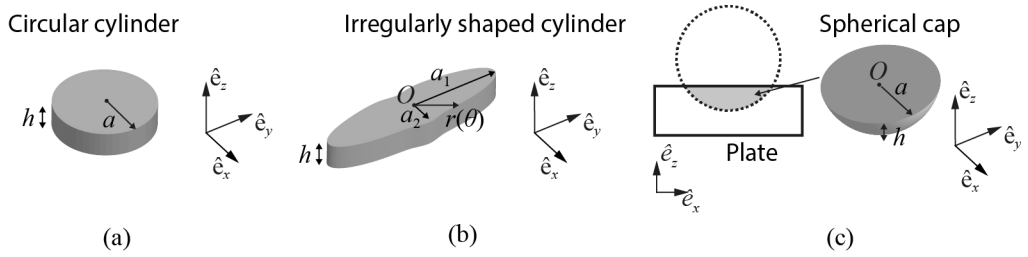


Figure 3.16 (a) The circular cylindrical inclusion, (b) the irregularly shaped cylindrical inclusion and (c) the spherical cap inclusion used to validate the suggested method.

sidered. One of comparable methods is the analytic solution based on Mindlin plate theory for flexural waves (anti-symmetric Lamb waves) scattering [100]. Another solution is obtained from the EBCM based on three-dimensional elasticity as discussed in Section 3.1.

Fig. 3.17(a) shows that at frequency of 30 kHz, the results obtained from three different method are in close agreement with each other. However, at 0.2 MHz and 0.5 MHz, the results obtained from Mindlin plate theory deviate from others. This is because three-dimensional elasticity uses 4 guided wave modes for description of flexural waves in an isotropic plate below 1 MHz·mm (as discussed in 3.4.3.2) while Mindlin plate theory [100] uses 3 modes. Thus it can be deduced from this investigation that the flexural wave scattering analysis based on the three dimensional elasticity have an advantage over approximate plate theories in mid and high frequency range.

3.4.3.4 An arbitrarily shaped scatterer

In this section, complex-shaped inclusions will be tested. In the first example, we consider scattering by an inclusion as shown in Fig. 3.16(b) at a frequency·thickness value of 0.5 MHz·mm. The inclusion is a cylindrical shape with radius r defined by the

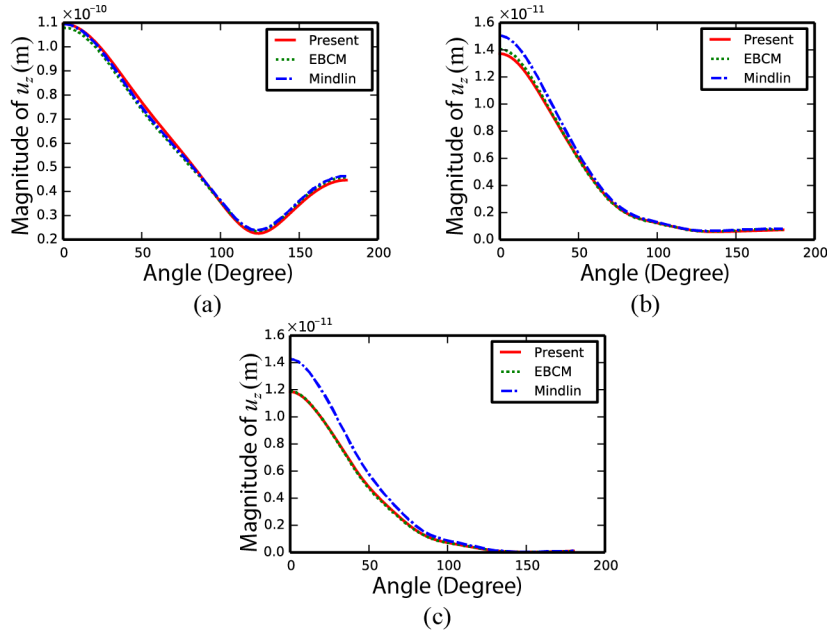


Figure 3.17 Scattered fields from an circular cylinder silicon inclusion in an aluminum plate of $d = 1$ mm thickness at frequency of (a) 30 kHz, (b) 0.2 MHz and (c) 0.5 MHz. The shape of the inclusion is illustrated in Fig. 3.16(a) with $a = 4d$, and $h = d$. The incident waves are A_0 actuated by a circular traction as illustrated in Fig. 3.12(a) with $a_{\text{ext}} = 2d$, $b_{\text{ext}} = 10d$ and $t_{\text{ext}} = 1$ N/m. For the proposed method and the EBCM, the symmetric modes are not included. The scattered fields are observed at $r = 20d$ from the center of the inclusion. $N = 4$ guided wave modes are used for the proposed method and the EBCM. For 30 kHz, we used grid size $c = \lambda_{A0}/20$ instead of $c = \lambda_{A0}/12$ to avoid poor approximation of the curved surface.

following equation in the horizontal plane of the plate:

$$r(\theta) = \frac{a_1 a_2}{\sqrt{a_1^2 \cos^2 \theta + a_2^2 \sin^2 \theta}} + \frac{a_2}{10} \cos 3\theta, \quad (3.4.1)$$

where $a_1 = 2\lambda_{A0}$ ($\lambda_{A0}/d = 3.754$), $a_2 = \lambda_{A0}/2$, and $h = d$. Because this inclusion has the largest radius of $2\lambda_{A0}$, this shape would cause ill-conditioning of the system

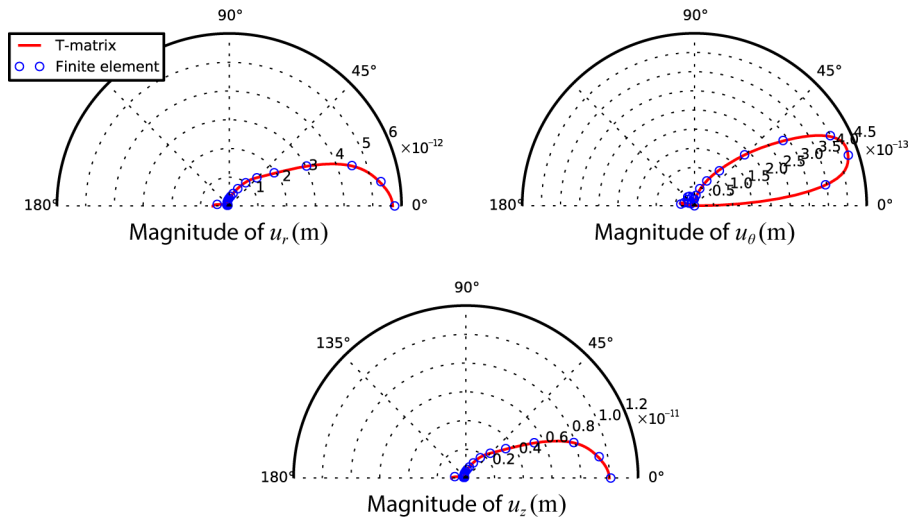


Figure 3.18 Scattered field from an irregularly shaped silicon inclusion in an aluminum plate. The shape of the inclusion is illustrated in Fig. 3.16(b) and defined in the horizontal plane by Eq. (3.4.1) with $a_1 = 2\lambda_{A0}$, $a_2 = \lambda_{A0}/2$, and $h = d$. The incident wave is actuated by line tractions as illustrated in Fig. 3.12(b) with $a_{\text{ext}} = \lambda_{A0}/2$, $r_{\text{ext}} = 5\lambda_{A0}$ and $t_{\text{ext}} = 1 \text{ N/m}$ at frequency \cdot thickness = 0.5 MHz \cdot mm. The scattered fields are observed at $r = 10\lambda_{A0}$ from the center of the inclusion on the top surface of the plate. The inclusion is decomposed into 452 subscatterers and $N = 4$ guided wave modes are used for the suggested method.

matrix when solved by using the existing method [44], [45]. To handle the irregular shape of the inclusion in the horizontal plane of the plate, the staircase approximation was applied. Fig. 3.18 shows good agreement between the results from the suggested method using 452 subscatterers and those from the finite element method. The good agreement also supports the validity of the staircase approximation.

In the next example, the aluminum-zirconia functionally graded plate with the same irregularly shaped inclusion in the previous example defined by Eq. (3.4.1) is

considered. The through-thickness material property profile is defined by Eq. (2.5.1) with $n = 1$. Since the through-thickness material variation of the functionally graded plate is not symmetric with respect to the mid-plane of the plate, actuation of purely symmetric or antisymmetric wave modes are very difficult. Therefore, the incident wave is actuated by a circular traction on the top surface of the plate which simultaneously excites mainly quasi A_0 mode along with quasi S_0 mode in small magnitude.

Fig. (3.19) at the frequency·thickness value of 0.5 MHz·mm shows that the results obtained from the proposed method by using the square subscatterers and equivalent circular subscatterers are overall in good agreement with those from the finite element method. However, for u_θ components small deviations between the results are observed. Specifically, the results obtained from using the original square subscatterers with the maximum circumferential order $M = 2$ are in a better agreement with those from the finite element method.

For the comparison, the same configuration in the previous example was analyzed at the frequency·thickness value of 1 MHz·mm. The results obtained by the proposed method also show small deviation for u_θ component from those from the finite element method. Therefore, from these observations, we can conclude that there is some amount of loss of information regarding the u_θ component of the field during the replacement of square subscatterers with circular subscatterers.

In the next example, we consider scattering by a spherical-cap-shaped inclusion as illustrated in Fig. 3.16(c) at a frequency·thickness value of 1 MHz·mm. The shape of the inclusion is defined by parameters $a = \lambda_{A0}$ ($\lambda_{A0}/d = 2.326$) and $h = d/2$. As in Fig. 3.21, the results from the suggested method using 452 subscatterers are overall in good agreement with those obtained by using the finite element method for all displacement components with minor deviation in the side robe for the u_θ component.

From the results of the above examples, the suggested method is useful for a class of elastic inclusions that cannot be solved by the previously developed techniques for

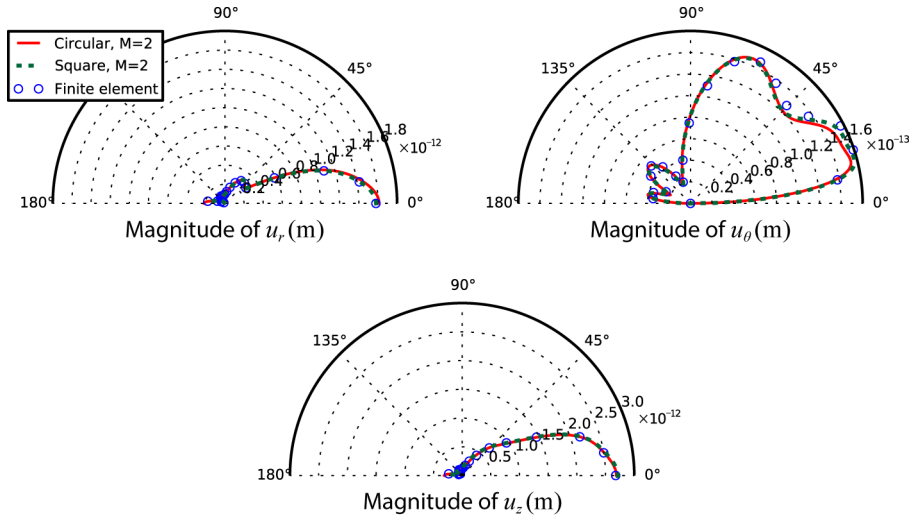


Figure 3.19 Scattered field from an irregularly shaped silicon inclusion in an aluminum-zirconia functionally graded plate with the power-law material variation parameter $n = 1$. The shape of the inclusion is illustrated in Fig. 3.16(b) and defined in the horizontal plane by Eq. (3.4.1) with $a_1 = 2\lambda_{A0}$, $a_2 = \lambda_{A0}/2$, and $h = d$. The incident wave is actuated by line tractions as illustrated in Fig. 3.12(a) with $a_{\text{ext}} = \lambda_{A0}/2$, $r_{\text{ext}} = 5\lambda_{A0}$ and $t_{\text{ext}} = 1$ N/m at frequency·thickness = 0.5 MHz·mm. The scattered fields are observed at $r = 8\lambda_{A0}$ from the center of the inclusion on the top surface of the plate. The inclusion is decomposed into 452 subscatterers and $N = 8$ guided wave modes are used for the suggested method.

scattering analysis by cavities in a plate.

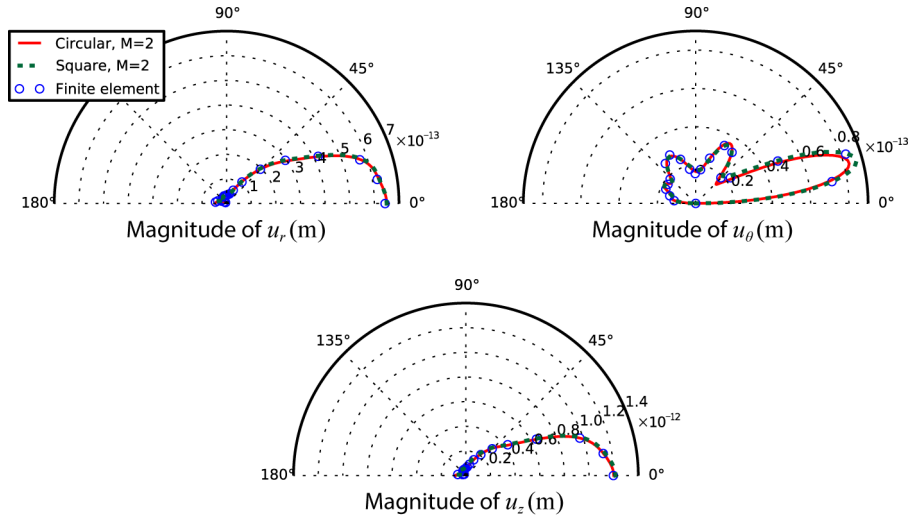


Figure 3.20 Scattered field from an irregularly shaped silicon inclusion in an aluminum-zirconia functionally graded plate with the power-law material variation parameter $n = 1$. The shape of the inclusion is illustrated in Fig. 3.16(b) and defined in the horizontal plane by Eq. (3.4.1) with $a_1 = 2\lambda_{A0}$, $a_2 = \lambda_{A0}/2$, and $h = d$. The incident wave is actuated by line tractions as illustrated in Fig. 3.12(a) with $a_{\text{ext}} = \lambda_{A0}/2$, $r_{\text{ext}} = 5\lambda_{A0}$ and $t_{\text{ext}} = 1 \text{ N/m}$ at frequency-thickness = 1 MHz·mm. The scattered fields are observed at $r = 8\lambda_{A0}$ from the center of the inclusion on the top surface of the plate. The inclusion is decomposed into 452 subscatterers and $N = 12$ guided wave modes are used for the suggested method.

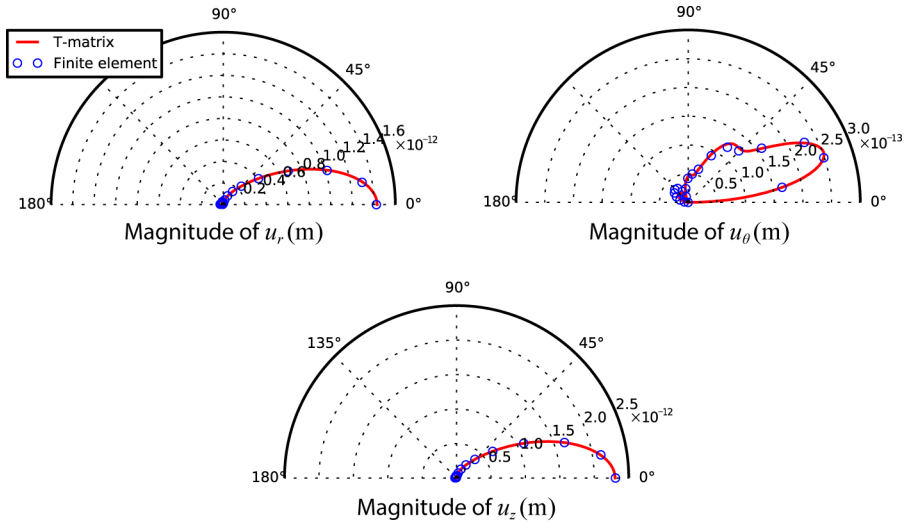


Figure 3.21 Scattered field from a spherical-cap-shaped silicon inclusion in an aluminum plate. The shape of the inclusion is illustrated in Fig. 3.16(c) and defined by parameters $a = \lambda_{A0}$ and $h = d/2$. The incident wave is actuated by line tractions as illustrated in Fig. 3.12 with $a_{\text{ext}} = \lambda_{A0}/2$, $r_{\text{ext}} = 5\lambda_{A0}$ and $t_{\text{ext}} = 1 \text{ N/m}$ at frequency·thickness = 1 MHz·mm. The scattered fields are observed at $r = 10\lambda_{A0}$ from the center of the inclusion on the top surface of the plate. For the suggested method, the inclusion is decomposed into 452 subscatterers and $N = 12$ guided wave modes are used.

Chapter 4

Conclusion and future works

4.1 Conclusion

In this dissertation, a semi-analytic techniques for scattering analysis of guided waves in flat transversely isotropic plates was developed. In terms of the development of analysis method for general scattering problems in flat plates, the existing previous semi-analytic methods based on the Rayleigh hypothesis have only partially fulfilled essential attributes; several researches have suggested analysis methods for problems regarding isotropic plates with a single scatterer of simple shape. Many problems typically faced in real industrial fields are still outside the area covered by these methods. Therefore, we aimed to enlarge the area by employing the transition matrix (T matrix) formalism. The major contribution of this dissertation to the related fields can be summarized as follows:

- Development of the integral transform method for deriving the multipole expansion of the Green's function for transversely isotropic plates
- Development of the extended boundary condition method for single and multiple scattering problems regarding an elastic inclusion, a step thickness increase or reduction

- Development of the decomposition method for scattering problems regarding arbitrarily-shaped elastic inclusions
- Derivation of the properties of the transition matrix for transversely isotropic plates

Specifically, in Chapter 1, we have developed the integral transform method for deriving the multipole expansion of the Green's function for transversely isotropic plates. In this method, we defined an integral transform pair that combines Fourier series expansion, Hankel transform and the eigenfunction expansion of the guided wave modes and, therefore, the Green's function appropriate for the T -matrix method was derived by using this transform. After the derivation, we also gave suggestions on procedures to solve radiation problems typically faced in NDE problems when modeling guided wave transducers by using the derived Green's function. In this context, we reviewed the method for calculating the basis functions for transversely isotropic plates including functionally graded plates.

In Chapter 2, we mainly have discussed about the extended boundary condition method (EBCM) and its application to multiple scattering problems. By adopting the EBCM, we have shown systematic approaches and simplified formula for scattering problems involving an elastic inclusion, a step thickness increase or reduction when compared to the previously existing methods based on Rayleigh hypothesis. The resulting form also naturally extends to multiple scattering problems while the form resulting from the previously existing needs further modifications in this sense. We also developed a decomposition method that can be applicable to elastic inclusions of arbitrary shapes since the previously existing methods have been strongly restricted in shapes and sizes of scatterers by the inherent characteristics of the guided wave basis functions. In this method, a scatterer of arbitrary shape is dealt with by decomposing a scatterer into multiple subscatterers and applying a multiple scattering theory to single

scatterer solutions. In addition to solving methods for scattering problems, we have also derived the three properties of the T matrix, the reciprocity, the energy conservation, the time-reversal invariance that should be satisfied by any T matrix regardless of its calculation method.

For validation of the proposed method, we have compared the results from the suggested method to those from the finite element method and also the analytic solutions based on the approximate plate theory for flexural waves showing good consistency.

4.2 Future works

As we have stated above, we have improved scattering problem solving technique by adopting the T matrix formalism. However, this dissertation is just one of many initiation towards a method that is efficient in computation time and that is also general in terms of applicable scatterer range. Thus much improvement may be expected by more extensive research in the future.

One can expect that the accuracy and the stability of the developed methods based on the EBCM can be improved by employing Galerkin type spectral methods [76] in calculation of the basis functions. This is because Galerkin type methods employ the weak form of governing equations and therefore only the first order derivatives of variables are needed while the pseudo-spectral method employed in this dissertation employ the strong form and thus requires the second order derivatives. Another method to improve accuracy is to employ extended or quad precision arithmetics for implementation on computer [101]. This approach does require some modification of the computer program as the programming language demands. Anyway it has been known that even with ill-conditioning of the matrix to be inverted extended or quad precision arithmetics do more stable matrix inversion than double precision does. Therefore, it is expected to be useful for calculations of the single scatterer T matrix through the

EBCM.

An improvement for the proposed decomposition method in need is adopting efficient multiple scattering algorithm; the most stable but slow method was adopted in this dissertation. The challenge in employing other multiple scattering algorithm is that guided wave scattering problems are inseparable from dealing with nonpropagating modes posing many numerical problems not appearing in bulk wave problems. This is because wavenumbers k_n of nonpropagating modes have a large imaginary part that makes Bessel functions $J_m(k_n r)$ diverge as $r \rightarrow \infty$. Thus, careful selection of appropriate algorithms and tests will be needed even though versatility of many algorithms are already proven in bulk wave problems. The recursive algorithm developed by Chew [19] is one of efficient algorithms and worth testing. However, it is highly possible that the previously stated problem regarding non-propagating modes occurs when this method is adopted for guided wave problems. For other efficient algorithms based on the T matrix formalism developed by Chew, see Ref. [102]. There is another efficient algorithm developed by Mackowski [22] and this may be adopted for guided wave problems without problems involving non-propagating modes. Preconditioned iterative algorithms such as GMRES, CG or BICG supplemented by FFT may be also a good candidate when solutions for a single or not many incident waves are needed [7].

Other research topics that can be initiated by this dissertation are to apply the proposed methods similarly to approximate plate theories such as Kirchhoff theory, Mindlin theory for flexural waves, Kane-Mindlin theory for extensional and shear waves. Efficiency and accuracy of employing such theories should be compared to those of the proposed methods.

Appendix A

Settings for the finite element method

In this appendix, we explain the details related to the settings used in the finite element analysis which can be regarded as reference solutions among other solutions if finite element meshes and the perfectly matches layers (PMLs) are carefully selected. For the finite element analysis, the commercially available software COMSOL Multiphysics [99] is used.

Fig. A.1 shows an example of the finite element meshes used in the dissertation. The domain consists of two cylindrical domain; the inner domain is where the incident and scattered fields propagate and the outer domain is the PML region to absorb the outgoing waves from the inner domain.

As shown in Fig. A.1, the top or the bottom surface of the plate is meshed first and then swept through the thickness direction. In this way, meshes can be evenly distributed through the thickness direction. The surface of the plate is meshed by the triangular elements in the inner domain and by the quadrilateral elements in the outer domain. The mesh size of $\lambda_{\min}/8 \sim \lambda_{\min}/10$ is used in the inner and outer domain except the region around the scatterer which has the mesh size of about $\lambda_{\min}/20$.

The absorbing rate of the PML implemented in COMSOL depends on the mesh size, the specified wave velocity to be absorbed and the geometry of the PML region. In many of two-dimensional scattering problem, the cylindrical PML region is typi-

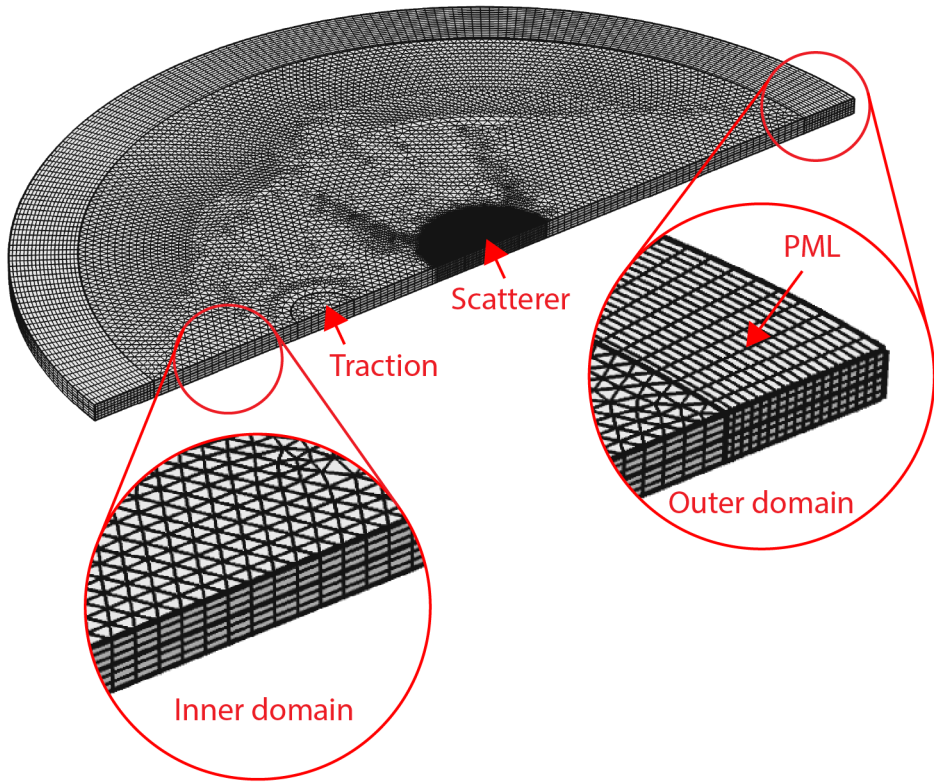


Figure A.1 The finite element meshes for circular domains used for validation of the proposed methods.

cally used. Therefore, we also used the cylindrical PML region even though problems concerned in the dissertation can be regarded as semi-two-dimensional. The thickness of the PML region used in example is λ_{\min} which is mostly λ_{A0} . We choose the wave velocity to be absorbed and specified in the PML setting of COMSOL to be $f\lambda_{\min}$; f denotes frequency and therefore $f\lambda_{\min}$ is the phase velocity of the propagating mode

having the minimum wavelength. The radius of the inner domain is at least $5\lambda_{\min}$ because the PML for the cylindrical domain mainly absorbs waves outgoing along the radial direction and waves propagating along the azimuthal direction are not absorbed well; therefore, it is better to place the wave source near the specified origin for the PML which is the center of the circular domain in the present problems.

Since scattered fields are of interest in the examples, the finite element analysis procedures take two steps. The first step is for calculation of the field actuated by tractions without the scatterers. The second step is for calculation of the field actuated by the tractions with the scatterers. Then, the field calculated from the first step is subtracted from the that from the second step.

Bibliography

- [1] K. Aki and P. Richards, *Quantitative Seismology*. University Science Books, 2002.
- [2] F. B. Jensen, *Computational Ocean Acoustics*. American Institute of Physics, 1994.
- [3] B. Pavlakovic, M. Lowe, D. Alleyne, and P. Cawley, “Disperse: a general purpose program for creating dispersion curves,” 1997.
- [4] Z. Xi, G. Liu, K. Lam, and H. Shang, “Dispersion and characteristic surfaces of waves in laminated composite circular cylindrical shells,” *The Journal of the Acoustical Society of America*, vol. 108, no. 5 Pt 1, p. 2179, 2000.
- [5] H. Huang and X.-f. Chen, “Exact solution of earth-flattening transformation for p-sv waves: taking surface wave as an example,” *Acta Seismologica Sinica*, vol. 21, no. 2, pp. 109–117, 2008.
- [6] W. C. Chew and G. P. Otto, “Microwave imaging of multiple conducting cylinders using local shape functions,” *IEEE microwave and guided wave letters*, vol. 2, no. 7, pp. 284–286, 1992.
- [7] J. H. Lin and W. C. Chew, “Bicg-fft t-matrix method for solving for the scattering solution from inhomogeneous bodies,” *Microwave Theory and Techniques, IEEE Transactions on*, vol. 44, no. 7, pp. 1150–1155, 1996.
- [8] R. L. Kevin, V. M. Eugene, and K. H. Mark, “Ultrasonic lamb wave tomography,” *Inverse Problems*, vol. 18, no. 6, p. 1795, 2002.

- [9] G. Pelekanos, A. Abubakar, and P. M. van den Berg, “Contrast source inversion methods in elastodynamics,” *The Journal of the Acoustical Society of America*, vol. 114, no. 5, pp. 2825–2834, 2003.
- [10] M. Mishchenko, L. Travis, and A. Lacis, *Scattering, Absorption, and Emission of Light by Small Particles*. Cambridge University Press, 2002.
- [11] A. Doicu, Y. Eremin, and T. Wriedt, *Acoustic and Electromagnetic Scattering Analysis using Discrete Sources*. Academic, 2000.
- [12] P. C. Waterman, “Matrix formulation of electromagnetic scattering,” *Proceedings of the IEEE*, vol. 53, no. 8, pp. 805–812, 1965.
- [13] W. Chew, *Waves and Fields in Inhomogeneous Media*. New York: Van Nostrand Reinhold, 1990.
- [14] T. Wriedt, *Generalized Multipole Techniques for Electromagnetic and Light Scattering*. Elsevier Science, 1999.
- [15] P. Martin, *Multiple Scattering: Interaction of Time-harmonic Waves With N Obstacles*. New York: Cambridge University Press, 2006.
- [16] J. L. Rose, “Ultrasonic waves in solid media (new york: cambridge university press),” 1999.
- [17] M. F. Iskander, A. Lakhtakia, and C. H. Durney, “A new procedure for improving the solution stability and extending the frequency range of the ebc,” *Antennas and Propagation, IEEE Transactions on*, vol. 31, no. 2, pp. 317–324, 1983.
- [18] A. Doicu, T. Wriedt, and Y. A. Eremin, *Light Scattering by Systems of Particles - Null-Field Method with Discrete Sources: Theory and Programs*, ser. Springer Series in Optical Sciences. Heidelberg, Germany: Springer, 2006.

- [19] C. Weng Cho, L. Gurel, Y. M. Wang, G. Otto, R. L. Wagner, and L. Qing Huo, "A generalized recursive algorithm for wave-scattering solutions in two dimensions," *Microwave Theory and Techniques, IEEE Transactions on*, vol. 40, no. 4, pp. 716–723, 1992.
- [20] W. C. Chew and L. Cai-Cheng, "The use of Huygens' equivalence principle for solving the volume integral equation of scattering," *Antennas and Propagation, IEEE Transactions on*, vol. 41, no. 7, pp. 897–904, 1993.
- [21] S. Koc and W. C. Chew, "Calculation of acoustical scattering from a cluster of scatterers," *The Journal of the Acoustical Society of America*, vol. 103, no. 2, pp. 721–734, 1998.
- [22] D. W. Mackowski and M. I. Mishchenko, "Calculation of the t matrix and the scattering matrix for ensembles of spheres," *Journal of the Optical Society of America A*, vol. 13, no. 11, pp. 2266–2278, 1996.
- [23] D. W. Mackowski, "Discrete dipole moment method for calculation of the t matrix for nonspherical particles," *Journal of the Optical Society of America A*, vol. 19, no. 5, pp. 881–893, 2002.
- [24] T. Wriedt and R. Schuh, "Decompositioning method to compute scattering by complex shaped particles using a multiple scattering t-matrix approach," *Journal of Quantitative Spectroscopy and Radiative Transfer*, vol. 109, no. 14, pp. 2315–2328, 2008.
- [25] E. M. Purcell and C. R. Pennypacker, "Scattering and absorption of light by nonspherical dielectric grains," *The Astrophysical Journal*, vol. 186, pp. 705–714, 1973.
- [26] J. Richmond, "Te-wave scattering by a dielectric cylinder of arbitrary cross-section shape," *Antennas and Propagation, IEEE Transactions on*, vol. 14, no. 4, pp. 460–464, 1966.

- [27] L. Gürel and W. C. Chew, “A recursive t-matrix algorithm for strips and patches,” *Radio Science*, vol. 27, no. 3, pp. 387–401, 1992.
- [28] M. A. Morgan and K. K. Mei, “Finite-element computation of scattering by inhomogeneous penetrable bodies of revolution,” *Antennas and Propagation, IEEE Transactions on*, vol. 27, no. 2, pp. 202–214, 1979.
- [29] J. H. Su, V. V. Varadan, and V. K. Varadan, “Finite element eigenfunction method (feem) for elastic wave scattering by arbitrary three-dimensional axisymmetric scatterers,” *Journal of Applied Mechanics*, vol. 51, no. 3, pp. 614–621, 1984.
- [30] L. Larsson and A. Rosell, “A hybrid formulation using the transition matrix method and finite elements in a 2d eddy current interaction problem,” 4th International Symposium on NDT in Aerospace - November 13 – 15, 2012, Augsburg, Germany, 2012.
- [31] T. A. Nieminen, H. Rubinsztein-Dunlop, and N. R. Heckenberg, “Calculation of the t-matrix: general considerations and application of the point-matching method,” *Journal of Quantitative Spectroscopy and Radiative Transfer*, vol. 79–80, pp. 1019–1029, 2003.
- [32] J. Wauer and T. Rother, “Considerations to rayleigh’s hypothesis,” *Optics Communications*, vol. 282, no. 3, pp. 339–350, 2009.
- [33] T. Grahn, “Lamb wave scattering from a circular partly through-thickness hole in a plate,” *Wave Motion*, vol. 37, no. 1, pp. 63–80, 2003.
- [34] Y. Leviatan, E. Erez, and M. J. Beran, “A source-model technique for analysis of flexural wave scattering in a heterogeneous thin plate,” *The Quarterly Journal of Mechanics and Applied Mathematics*, vol. 45, no. 3, pp. 499–514, 1992.

- [35] A. N. Norris and C. Vemula, “Scattering of flexural waves on thin plates,” *Journal of Sound and Vibration*, vol. 181, no. 1, pp. 115–125, 1995.
- [36] J. C. P. McKeon and M. K. Hinders, “Lamb wave scattering from a through hole,” *Journal of Sound and Vibration*, vol. 224, no. 5, pp. 843–862, 1999.
- [37] F. B. Cegla, A. Rohde, and M. Veidt, “Analytical prediction and experimental measurement for mode conversion and scattering of plate waves at non-symmetric circular blind holes in isotropic plates,” *Wave Motion*, vol. 45, no. 3, pp. 162–177, 2008.
- [38] C. H. Wang and F.-K. Chang, “Scattering of plate waves by a cylindrical inhomogeneity,” *Journal of Sound and Vibration*, vol. 282, no. 1–2, pp. 429–451, 2005.
- [39] W. M. Lee and J. T. Chen, “Scattering of flexural wave in a thin plate with multiple circular inclusions by using the null-field integral equation approach,” *Journal of Sound and Vibration*, vol. 329, no. 8, pp. 1042–1061, 2010.
- [40] L. R. F. Rose and C. H. Wang, “Mindlin plate theory for damage detection: imaging of flexural inhomogeneities,” *The Journal of the Acoustical Society of America*, vol. 127, no. 2, pp. 754–763, 2010.
- [41] W. J. Parnell and P. A. Martin, “Multiple scattering of flexural waves by random configurations of inclusions in thin plates,” *Wave Motion*, vol. 48, no. 2, pp. 161–175, 2011.
- [42] D. Torrent, Y. Pennec, and B. Djafari-Rouhani, “Effective medium theory for elastic metamaterials in thin elastic plates,” *Physical Review B*, vol. 90, no. 10, p. 104 110, 2014.
- [43] O. Diligent, T. Grahn, A. Boström, P. Cawley, and M. J. S. Lowe, “The low-frequency reflection and scattering of the s_0 lamb mode from a circular through-

- thickness hole in a plate: finite element, analytical and experimental studies,” *The Journal of the Acoustical Society of America*, vol. 112, no. 6, p. 2589, 2002.
- [44] L. Moreau, M. Caleap, A. Velichko, and P. D. Wilcox, “Scattering of guided waves by through-thickness cavities with irregular shapes,” *Wave Motion*, vol. 48, no. 7, pp. 586–602, 2011.
- [45] ———, “Scattering of guided waves by flat-bottomed cavities with irregular shapes,” *Wave Motion*, vol. 49, no. 2, pp. 375–387, 2012.
- [46] R. H. Lyon, “Response of an elastic plate to localized driving forces,” *The Journal of the Acoustical Society of America*, vol. 27, no. 2, pp. 259–265, 1955.
- [47] R. L. Weaver and Y.-H. Pao, “Axisymmetric elastic waves excited by a point source in a plate,” *Journal of Applied Mechanics*, vol. 49, no. 4, pp. 821–836, 1982.
- [48] N. Vasudevan and A. K. Mal, “Response of an elastic plate to localized transient sources,” *Journal of Applied Mechanics*, vol. 52, no. 2, pp. 356–362, 1985.
- [49] F. Santosa and Y.-H. Pao, “Transient axially asymmetric response of an elastic plate,” *Wave Motion*, vol. 11, no. 3, pp. 271–295, 1989.
- [50] G. Liu and Z. C. *Elastic Waves in Anisotropic Laminates*. Taylor & Francis, 2001.
- [51] M. Tan and B. A. Auld, “Normal mode variational method for two- and three-dimensional acoustic scattering in an isotropic plate,” in *1980 Ultrasonics Symposium*, 1980, pp. 857–861.

- [52] J. D. Achenbach and Y. Xu, “Wave motion in an isotropic elastic layer generated by a time-harmonic point load of arbitrary direction,” *The Journal of the Acoustical Society of America*, vol. 106, no. 1, pp. 83–90, 1999.
- [53] H. Bai, J. Zhu, A. H. Shah, and N. Popplewell, “Three-dimensional steady state green function for a layered isotropic plate,” *Journal of Sound and Vibration*, vol. 269, no. 1–2, pp. 251–271, 2004.
- [54] Y. Hisada, “An efficient method for computing green’s functions for a layered half-space with sources and receivers at close depths,” *Bulletin of the Seismological Society of America*, vol. 84, no. 5, pp. 1456–1472, 1994.
- [55] B. B. Guzina and R. Y. S. Pak, “On the analysis of wave motions in a multi-layered solid,” *The Quarterly Journal of Mechanics and Applied Mathematics*, vol. 54, no. 1, pp. 13–37, 2001.
- [56] P. Waterman, “Matrix theory of elastic wave scattering,” *The Journal of the Acoustical Society of America*, vol. 60, pp. 567–580, 1976.
- [57] V. Varatharajulu and Y. Pao, “Scattering matrix for elastic waves. i. theory,” *The Journal of the Acoustical Society of America*, vol. 60, pp. 556–566, 1976.
- [58] C. Tai, *Dyadic Green’s Functions in Electromagnetic Theory*. Intext Educational Publishers, 1971.
- [59] W. B. Fraser, “Orthogonality relation for the rayleigh–lamb modes of vibration of a plate,” *The Journal of the Acoustical Society of America*, vol. 59, no. 1, pp. 215–216, 1976.
- [60] J. Achenbach, *Reciprocity in Elastodynamics*. New York: Cambridge University Press, 2003.
- [61] P. Morse and H. Feshbach, *Methods of Theoretical Physics*. McGraw-Hill, 1953.

- [62] J. Miklowitz, *The Theory of Elastic Waves and Waveguides*. North Holland Publishing Company, 1978.
- [63] R. D. Mindlin, *Waves and Vibrations in Isotropic Elastic plates*, ser. Structural Mechanics. New York: Pergamon, 1960.
- [64] A. Sommerfeld, *Partial Differential Equations in Physics*. Academic Press, 1949.
- [65] N. Baddour, “Multidimensional wave field signal theory: mathematical foundations,” *AIP Advances*, vol. 1, no. 2, 2011.
- [66] A. Bostrom, G. Kristensson, and S. Strom, “Transformation properties of plane, spherical and cylindrical scalar and vector wave functions,” in *Field Representations and Introduction to Scattering*, V. V. Varadan, A. Lakhtakia, and V. K. Varadan, Eds., Amsterdam: North-Holland, 1991.
- [67] J. Achenbach, “Wave propagation in elastic solids (amsterdam: north-holland publishing company),” 1973.
- [68] K. Graff, *Wave Motion in Elastic Solids*. Dover Pubns, 1975.
- [69] M. A. Denolle, E. M. Dunham, and G. C. Beroza, “Solving the surfacewave eigenproblem with chebyshev spectral collocation,” *Bulletin of the Seismological Society of America*, vol. 102, no. 3, pp. 1214–1223, 2012.
- [70] W. Elmore and M. Heald, *Physics of Waves*. Dover Publications, 1969.
- [71] L. N. Trefethen, *Spectral Methods in MatLab*. Society for Industrial and Applied Mathematics, 2000.
- [72] A. T. I. Adamou and R. V. Craster, “Spectral methods for modelling guided waves in elastic media,” *The Journal of the Acoustical Society of America*, vol. 116, no. 3, pp. 1524–1535, 2004.

- [73] E. Anderson, Z. Bai, J. Dongarra, A. Greenbaum, A. McKenney, J. D. Croz, S. Hammerling, J. Demmel, C. Bischof, and D. Sorensen, “Lapack: a portable linear algebra library for high-performance computers,” in *Proceedings of the 1990 ACM/IEEE conference on Supercomputing*, New York, New York, USA: IEEE Computer Society Press, 1990, pp. 2–11.
- [74] S. v. d. Walt, S. C. Colbert, and G. Varoquaux, “The numpy array: a structure for efficient numerical computation,” *Computing in Science and Engineering*, vol. 13, no. 2, pp. 22–30, 2011.
- [75] MATLAB, *version 8.1.0.604 (R2013a)*. Natick, Massachusetts: The MathWorks Inc., 2013.
- [76] J. Shen, T. Tang, and L. Wang, *Spectral Methods: Algorithms, Analysis and Applications*. Springer, 2011.
- [77] J. Waldvogel, “Fast construction of the fejer and clenshaw–curtis quadrature rules,” *BIT Numerical Mathematics*, vol. 46, no. 1, pp. 195–202, 2006.
- [78] R. Ajay and E. S. C. Carlos, “Finite-dimensional piezoelectric transducer modeling for guided wave based structural health monitoring,” *Smart Materials and Structures*, vol. 14, no. 6, p. 1448, 2005.
- [79] H.-S. Yoon, D. Jung, and J.-H. Kim, “Lamb wave generation and detection using piezoceramic stack transducers for structural health monitoring applications,” *Smart Materials and Structures*, vol. 21, no. 5, p. 055 019, 2012.
- [80] P. D. Wilcox, M. J. Lowe, and P. Cawley, “The excitation and detection of lamb waves with planar coil electromagnetic acoustic transducers,” *Ultrasonics, Ferroelectrics, and Frequency Control, IEEE Transactions on*, vol. 52, no. 12, pp. 2370–2383, 2005.

- [81] J. S. Lee, Y. Y. Kim, and S. H. Cho, “Beam-focused shear-horizontal wave generation in a plate by a circular magnetostrictive patch transducer employing a planar solenoid array,” *Smart Materials and Structures*, vol. 18, no. 1, p. 015 009, 2009.
- [82] P. Wilcox, M. Lowe, and P. Cawley, “Omnidirectional guided wave inspection of large metallic plate structures using an emat array,” *Ultrasonics, Ferroelectrics, and Frequency Control, IEEE Transactions on*, vol. 52, no. 4, pp. 653–665, 2005.
- [83] V. Giurgiutiu, “Tuned lamb wave excitation and detection with piezoelectric wafer active sensors for structural health monitoring,” *Journal of Intelligent Material Systems and Structures*, vol. 16, no. 4, pp. 291–305, 2005.
- [84] S. H. Cho, J. S. Lee, and Y. Y. Kim, “Guided wave transduction experiment using a circular magnetostrictive patch and a figure-of-eight coil in nonferromagnetic plates,” *Applied Physics Letters*, vol. 88, no. 22, p. 224 101, 2006.
- [85] A. Raghavan and C. Cesnik, “Review of guided-wave structural health monitoring,” *Shock and Vibration Digest*, vol. 39, no. 2, pp. 91–116, 2007.
- [86] J. K. Lee, H. W. Kim, and Y. Y. Kim, “Omnidirectional lamb waves by axisymmetrically-configured magnetostrictive patch transducer,” *Ultrasonics, Ferroelectrics, and Frequency Control, IEEE Transactions on*, vol. 60, no. 9, pp. 1928–1934, 2013.
- [87] H. M. Seung, H. W. Kim, and Y. Y. Kim, “Development of an omni-directional shear-horizontal wave magnetostrictive patch transducer for plates,” *Ultrasonics*, vol. 53, no. 7, pp. 1304–1308, 2013.
- [88] H. J. Kim, J. S. Lee, H. W. Kim, H. S. Lee, and Y. Y. Kim, “Numerical simulation of guided waves using equivalent source model of magnetostrictive patch transducers,” *Smart Materials and Structures*, vol. 24, no. 1, p. 015 006, 2015.

- [89] J. Stratton, I. Antennas, and P. Society, *Electromagnetic Theory*. Wiley, 2007.
- [90] R. H. MacPhie and W. Ke-Li, "Scattering at the junction of a rectangular waveguide and a larger circular waveguide," *Microwave Theory and Techniques, IEEE Transactions on*, vol. 43, no. 9, pp. 2041–2045, 1995.
- [91] J. Reddy, "Analysis of functionally graded plates," *International Journal for Numerical Methods in Engineering*, vol. 47, no. 1-3, pp. 663–684, 2000.
- [92] L. R. F. Rose and C. H. Wang, "Mindlin plate theory for damage detection: source solutions," *The Journal of the Acoustical Society of America*, vol. 116, no. 1, pp. 154–171, 2004.
- [93] M. Heckl, "Structure-borne-sound," in *Noise Generation and Control in Mechanical Engineering*, Springer, 1982, pp. 209–287.
- [94] Y. Pao and V. Varatharajulu, "Huygens' principle, radiation conditions, and integral formulas for the scattering of elastic waves," *The Journal of the Acoustical Society of America*, vol. 59, p. 1361, 1976.
- [95] D. Felbacq, G. Tayeb, and D. Maystre, "Scattering by a random set of parallel cylinders," *The Journal of the Optical Society of America A*, vol. 11, no. 9, pp. 2526–2538, 1994.
- [96] M. Abramowitz and I. Stegun, *Handbook of Mathematical Functions: With Formulas, Graphs, and Mathematical Tables*. Dover Publications, 1964.
- [97] V. Pagneux and A. Maurel, "Scattering matrix properties with evanescent modes for waveguides in fluids and solids," *The Journal of the Acoustical Society of America*, vol. 116, pp. 1913–1920, 2004.
- [98] M. Bostock and B. Kennett, "Multiple scattering of surface waves from discrete obstacles," *Geophysical journal international*, vol. 108, no. 1, pp. 52–70, 1992.

- [99] COMSOL, *COMSOL Multiphysics Structural Mechanics Module: User's guide*. Stockholm, Sweden: COMSOL AB., 2013.
- [100] C. Vemula and A. N. Norris, "Flexural wave propagation and scattering on thin plates using mindlin theory," *Wave Motion*, vol. 26, no. 1, pp. 1–12, 1997.
- [101] M. I. Mishchenko and L. D. Travis, "T-matrix computations of light scattering by large spheroidal particles," *Optics communications*, vol. 109, no. 1, pp. 16–21, 1994.
- [102] W. C. Chew, C. C. Lu, and Y. M. Wang, "Efficient computation of three-dimensional scattering of vector electromagnetic waves," *Journal of the Optical Society of America A*, vol. 11, no. 4, pp. 1528–1537, 1994.

초록

매우 평판 구조물 내의 탄성 유도초음파 산란현상에 대한 T -matrix 해법

이 흥 선

서울대학교 대학원

기계항공공학부

본 논문은 평판에서 발생하는 유도파의 산란현상을 분석하기 위한 준 이론적 기법을 다룬다. 연구 목표는 횡등방성을 가지는 평판 — 즉 등방성 평판, 적층된 등방성 평판과 함수적 구배를 가지는 평판 — 내에 존재하는 산란 문제를 다루기에 적합한 방법을 개발하는 것이다. 특히, 삼차원 탄성방정식에 기반한 파동함수 전개 기법을 개발하는 것에 중점을 두었다. 파동함수 전개 기법에서는 파동을 지배방정식의 고유함수로 전개한다. 이 논문에서는 기존의 파동함수 전개법에 기반한 해석 기법에서 다루지 않은 문제를 다루고자 전환 행렬 기법(the transition matrix method)을 차용하였다; 전환 행렬 기법은 입사파의 전개 계수와 산란파의 기저 함수에 대한 전개 계수를 T 행렬을 통해서 기술한다.

이러한 이유로 전환 행렬 기법에 필요한 요소들 — 즉 기저 함수와 이를 이용해서 유도할 수 있는 그린 함수 — 에 대해서 먼저 다룬다. 여기서 유도한 그린 함수는 적분 방정식에 이용되며 이를 통해서 파동의 방사 문제 또는 산란 문제를 풀 수 있다. 이 적분 방정식을 이용하면 비교적 단순한 형상을 가진 단일 산란체의 T 행렬을

구할 수 있다. 이러한 방법으로 산란체가 탄성 함유물인 경우 또는 기저 평판과 두께가 다른 산란체를 다루는 경우 등에 대해서 T 행렬의 식을 유도할 것이다. 또한 단일 산란체의 T 행렬을 이용하면 다수의 산란체에 대한 다중 산란 현상이 고려된 T 행렬도 구할 수 있다. 본 논문에서는 T 행렬을 구한 방법 외에도 T 행렬이 가지는 세가지 일반적인 성질을 유도할 것이다.

마지막으로는 산란체가 탄성 함유물(용접부 등)인 경우에 다양한 형상과 크기의 산란체를 다룰 수 있는 기법을 개발 할 것이다. 이 기법에서는 탄성 함유물을 다수의 작은 산란체로 나누고, 여기에 다중 산란 현상을 적용한다. 이로서 적분 방정식에 기반해서 단일 산란체의 T 행렬을 구하기 위한 방식에서 나타나는 한계를 상당부분 해결 할 수 있다.

본 논문에서 개발된 기법은 유한 요소 해석법 또는 근사 판 이론에 의한 해와 비교하여 검증 할 것이다.

주요어: 탄성파, 유도파, 평판파, 산란 현상 해석

학번: 2009-20715